

THESIS

EXPERIMENTAL INVESTIGATION OF WIND EFFECTS ON LONG-SPAN  
SLENDER BRIDGES WITH STOCHASTIC TRAFFIC FLOW

Submitted by

Ryan Scott Nelson

Department of Civil and Environmental Engineering

In partial fulfillment of the requirements

For the Degree of Master of Science

Colorado State University

Fort Collins, Colorado

Spring 2011

Master's Committee:

Advisor: Suren Chen

Bogusz Bienkiewicz

Horishi Sakuria

## ABSTRACT

### EXPERIMENTAL INVESTIGATION OF WIND EFFECTS ON LONG-SPAN SLENDER BRIDGES WITH STOCHASTIC TRAFFIC FLOW

The aeroelastic and aerodynamic effects on long-span slender bridges due to traffic has traditionally been neglected as it is assumed that the bridges will be closed to traffic under strong winds. However, with ever changing weather, natural disasters, and important roles of many long-span bridges throughout the United States, the reality is that these long-span bridges are often not closed and there are still many vehicles on the bridges even when considerably strong winds exist. Therefore, to rationally evaluate the aerodynamic performance of a bridge deck, the impacts from stochastic traffic should be appropriately considered as a key part toward any safety or serviceability study.

The present study discusses the wind tunnel experimental tests of a long-span bridge section with stochastic traffic. The details of the experimental investigations are reported, including the design and construction of a bridge section model, two-degree-of-freedom testing frame and vehicle models representing stochastic traffic. Several tests were performed to determine a baseline for the bridge section without traffic, under different wind speeds and attack angles. The bridge section was then re-tested with many scenarios representing stochastic and extreme traffic conditions. The aeroelastic flutter derivative coefficients were extracted using the iterative mean square method and the values plotted and compared with the baseline results. Under the given reduced velocity range being tested, it is observed that several traffic scenarios increase the aeroelastic and aerodynamic effects as the bridge section becomes more susceptible to flutter and vortex shedding. Finally, the statistical descriptions of the flutter derivatives with the presence of traffic on the bridge section model are also made.

## ACKNOWLEDGEMENTS

I am deeply indebted to my advisor, Professor Suren Chen, for his constant support and guidance. Without his encouragement and understanding of the many obstacles encountered during the experimental work, it would have been nearly impossible to complete. I would also like to give a special thanks to Professor Bogusz Bienkiewicz. His extensive experience with wind tunnel testing provided a wealth of helpful advice and guidance during the development of the experimental setup and throughout the testing phase.

I would like to thank fellow students Feng Chen for the development of the iterative least squares programming in MATLAB and the assistance on wind tunnel testing, Dr. Jun Wu for the traffic flow simulation, Munehito Endo and Swagat Mohopatra for their assistance with the wind tunnel operation and maintenance.

Lastly, I would like to thank my family for their support and love, as my wife Briana and son Kyle had to go it alone at times so I could finish my thesis work.

This study is supported by the National Science Foundation under Grant No. CMMI-0900253. Any opinions, findings, and conclusions or recommendations expressed in this material are those of the investigators and do not necessarily reflect the views of the National Science Foundation.

# TABLE OF CONTENTS

ABSTRACT .....	ii
ACKNOWLEDGEMENTS .....	iii
LISTS OF FIGURES & TABLES .....	vi
CHAPTER 1 .....	1
1.1 Introduction.....	1
1.2 Long-span Bridge Aerodynamics .....	1
1.2.1 Aerodynamics and Aeroelastic Effect.....	2
1.2.2 Fluid (wind) Force Coefficients.....	3
1.2.3 Flutter Derivatives .....	3
1.3 Wind Tunnel Experiments .....	4
1.4 The State-of-the-Art of Bridge Section Model Tests.....	6
1.5 Significance of the Study .....	8
CHAPTER 2 EXPERIMENTAL DESIGNS.....	10
2.1 Bridge Model Design.....	10
2.2 Vehicle Model Design .....	20
2.3 Equipment & Test Setup.....	22
2.4 Test Scenarios .....	26
2.5 Identification of Flutter Derivatives.....	27
2.6 ILS-Method.....	30
CHAPTER 3 WIND TUNNEL TEST RESULTS.....	34

3.1 Calibration Tests without Vehicles .....	34
3.2 Spatial Dependent Traffic Test Results .....	41
3.2.1 Spatial Cases 2.1-2.3 with Traffic Density of 20 vehicles/km/ln.....	41
3.2.2 Spatial Cases 3.1-3.3 with Traffic Density of 32 vehicles/km/ln.....	49
3.3 Time Dependent Traffic Test Results .....	54
3.3.1 Time Cases 1.1-1.3 with 20 vehicles/km/ln .....	54
3.3.2 Time Cases 2.1-2.3 with 32 vehicles/km/ln .....	60
3.4 Extreme Traffic Test Results .....	65
3.4.1 Extreme Traffic Zero Attack Angle .....	65
3.4.2 Extreme Traffic Scenarios with negative 3° Attack Angle .....	71
3.4.3 Extreme Traffic Scenarios with Positive 3° Attack Angle.....	76
3.5 Comparison of Attack Angles.....	81
3.6 Statistical Descriptions of Variation in Spatial Traffic Simulations .....	85
3.6.1 Spatial Cases 2.1-3 Statistical Variation for 20 veh/km/ln Traffic Flow .....	86
3.6.2 Spatial Cases 3.1-3 Statistical Variation for 32 veh/km/ln Traffic Flow .....	90
3.7 Vortex Shedding Phenomenon in Tests .....	94
CHAPTER 4 SUMMARY & DISCUSSION .....	95
4.1 Summary and Discussions .....	95
4.2 Significance of Stochastic and Extreme Traffic Flow .....	96
4.3 Recommendations and Future Experiments .....	98
REFERENCES .....	100

## LISTS OF FIGURES & TABLES

Figure 2.1: Free Body Diagram progression of section model to determine torsional distance ..	12
Figure 2.2: Dimensioned cross-section of the bridge section model (cm).....	13
Figure 2.3: Original copper supports built into bridge section model .....	13
Figure 2.4: 3D view of sectional bridge deck model .....	14
Figure 2.5: 3D view of sectional bridge deck model with removed plywood skin and end plates .....	14
Figure 2.6: Vertical time history, no wind.....	15
Figure 2.7: Torsional time history, no wind.....	15
Figure 2.8: West side picture of model setup in wind tunnel frame .....	17
Figure 2.9: Picture of bridge section in the Industrial Wind Tunnel .....	18
Figure 2.10: Photograph of model vehicles .....	22
Figure 2.11: Industrial Aerodynamics Wind Tunnel at Colorado State University.....	23
Figure 2.12: Mobile support frame for bridge section model .....	24
Figure 2.13: Top view of bridge section mounted in wind tunnel .....	25
Figure 2.14: Photograph bumper to bumper leeward side traffic .....	27
Figure 2.15: 2-DOF bridge deck cross-section view .....	29
Figure 2.16: Iterative Least Squares, from (Chowdhury & Sarkar, 2003).....	33
Figure 3.1: Three calibration tests of pure vertical and coupled flutter analysis of H1 <sup>*</sup> .....	35
Figure 3.2: The average results of pure vertical and coupled flutter analysis of H1 <sup>*</sup> .....	35
Figure 3.3: Three tests of pure vertical and coupled flutter analysis of H4 <sup>*</sup> .....	36
Figure 3.4: The average results of pure vertical and coupled flutter analysis of H4 <sup>*</sup> .....	36

Figure 3.5: Three tests of pure torsional and coupled flutter analysis of A2*	37
Figure 3.6: The average results of pure torsional and coupled flutter analysis of A2*	37
Figure 3.7: Three tests of pure torsional and coupled flutter analysis of A3*	38
Figure 3.8: The average results of pure torsional and coupled flutter analysis of A3*	38
Figure 3.9: Spatial dependent vehicle positioning for cases 2.1-2.3 with 20 vehicles/km/lane...	44
Figure 3.10: Flutter derivative A1* for Spatial Cases 2.1-2.3	45
Figure 3.11: Flutter derivative A2* for Spatial Cases 2.1-2.3	45
Figure 3.12: Flutter derivative A3* for Spatial Cases 2.1-2.3	46
Figure 3.13: Flutter derivative A4* for Spatial Cases 2.1-2.3	46
Figure 3.14: Flutter derivative H1* for Spatial Cases 2.1-2.3	47
Figure 3.15: Flutter derivative H2* for Spatial Cases 2.1-2.3	47
Figure 3.16: Flutter derivative H3* for Spatial Cases 2.1-2.3	48
Figure 3.17: Flutter derivative H4* for Spatial Cases 2.1-2.3	48
Figure 3.18: Spatial dependent vehicle positioning for cases 3.1-3.3 with 32 vehicles/km/lane.	49
Figure 3.19: Flutter derivative A1* for Spatial Cases 3.1-3.3	50
Figure 3.20: Flutter derivative A2* for Spatial Cases 3.1-3.3	50
Figure 3.21: Flutter derivative A3* for Spatial Cases 3.1-3.3	51
Figure 3.22: Flutter derivative A4* for Spatial Cases 3.1-3.3	51
Figure 3.23: Flutter derivative H1* for Spatial Cases 3.1-3.3	52
Figure 3.24: Flutter derivative H2* for Spatial Cases 3.1-3.3	52
Figure 3.25: Flutter derivative H3* for Spatial Cases 3.1-3.3	53
Figure 3.26: Flutter derivative H4* for Spatial Cases 3.1-3.3	53
Figure 3.27: Time dependent vehicle positioning for cases 1.1-1.3 with 20 vehicles/km/lane ...	55
Figure 3.28: Flutter derivative A1* for Time Cases 1.1-1.3	56
Figure 3.29: Flutter derivative A2* for Time Cases 1.1-1.3	56
Figure 3.30: Flutter derivative A3* for Time Cases 1.1-1.3	57

Figure 3.31: Flutter derivative $A4^*$ for Time Cases 1.1-1.3.....	57
Figure 3.32: Flutter derivative $H1^*$ for Time Cases 1.1-1.3.....	58
Figure 3.33: Flutter derivative $H2^*$ for Time Cases 1.1-1.3.....	58
Figure 3.34: Flutter derivative $H3^*$ for Time Cases 1.1-1.3.....	59
Figure 3.35: Flutter derivative $H4^*$ for Time Cases 1.1-1.3.....	59
Figure 3.36: Time dependent vehicle positioning for cases 2.1-2.3 with 32 vehicles/km/lane ...	60
Figure 3.37: Flutter derivative $A1^*$ for Time Cases 2.1-2.3.....	61
Figure 3.38: Flutter derivative $A2^*$ for Time Cases 2.1-2.3.....	61
Figure 3.39: Flutter derivative $A3^*$ for Time Cases 2.1-2.3.....	62
Figure 3.40: Flutter derivative $A4^*$ for Time Cases 2.1-2.3.....	62
Figure 3.41: Flutter derivative $H1^*$ for Time Cases 2.1-2.3.....	63
Figure 3.42: Flutter derivative $H2^*$ for Time Cases 2.1-2.3.....	63
Figure 3.43: Flutter derivative $H3^*$ for Time Cases 2.1-2.3.....	64
Figure 3.44: Flutter derivative $H4^*$ for Time Cases 2.1-2.3.....	64
Figure 3.45: Extreme traffic scenarios vehicle layouts.....	66
Figure 3.46: Flutter derivative $A1^*$ for Extreme traffic scenarios.....	67
Figure 3.47: Flutter derivative $A2^*$ for Extreme traffic scenarios.....	67
Figure 3.48: Flutter derivative $A3^*$ for Extreme traffic scenarios.....	68
Figure 3.49: Flutter derivative $A4^*$ for Extreme traffic scenarios.....	68
Figure 3.50: Flutter derivative $H1^*$ for Extreme traffic scenarios.....	69
Figure 3.51: Flutter derivative $H2^*$ for Extreme traffic scenarios.....	69
Figure 3.52: Flutter derivative $H3^*$ for Extreme traffic scenarios.....	70
Figure 3.53: Flutter derivative $H4^*$ for Extreme traffic scenarios.....	70
Figure 3.54: Bridge cross-section with $3^\circ$ negative attack angle .....	71
Figure 3.55: Flutter derivative $A1^*$ for Extreme traffic scenarios with $-3^\circ$ attack angle .....	72
Figure 3.56: Flutter derivative $A2^*$ for Extreme traffic scenarios with $-3^\circ$ attack angle .....	72

Figure 3.57: Flutter derivative $A3^*$ for Extreme traffic scenarios with $-3^\circ$ attack angle .....	73
Figure 3.58: Flutter derivative $A4^*$ for Extreme traffic scenarios with $-3^\circ$ attack angle .....	73
Figure 3.59: Flutter derivative $H1^*$ for Extreme traffic scenarios with $-3^\circ$ attack angle .....	74
Figure 3.60: Flutter derivative $H2^*$ for Extreme traffic scenarios with $-3^\circ$ attack angle .....	74
Figure 3.61: Flutter derivative $H3^*$ for Extreme traffic scenarios with $-3^\circ$ attack angle .....	75
Figure 3.62: Flutter derivative $H4^*$ for Extreme traffic scenarios with $-3^\circ$ attack angle .....	75
Figure 3.63: Bridge cross-section with positive $3^\circ$ attack angle .....	76
Figure 3.64: Flutter derivative $A1^*$ for Extreme traffic scenarios with $+3^\circ$ attack angle .....	77
Figure 3.65: Flutter derivative $A2^*$ for Extreme traffic scenarios with $+3^\circ$ attack angle .....	77
Figure 3.66: Flutter derivative $A3^*$ for Extreme traffic scenarios with $+3^\circ$ attack angle .....	78
Figure 3.67: Flutter derivative $A4^*$ for Extreme traffic scenarios with $+3^\circ$ attack angle .....	78
Figure 3.68: Flutter derivative $H1^*$ for Extreme traffic scenarios with $+3^\circ$ attack angle .....	79
Figure 3.69: Flutter derivative $H2^*$ for Extreme traffic scenarios with $+3^\circ$ attack angle .....	79
Figure 3.70: Flutter derivative $H3^*$ for Extreme traffic scenarios with $+3^\circ$ attack angle .....	80
Figure 3.71: Flutter derivative $H4^*$ for Extreme traffic scenarios with $+3^\circ$ attack angle .....	80
Figure 3.72: Changes in $A1^*$ due to attack angle, no vehicles .....	81
Figure 3.73: Changes in $A2^*$ due to attack angle, no vehicles .....	82
Figure 3.74: Changes in $A3^*$ due to attack angle, no vehicles .....	82
Figure 3.75: Changes in $A4^*$ due to attack angle, no vehicles .....	83
Figure 3.76: Changes in $H1^*$ due to attack angle, no vehicles .....	83
Figure 3.77: Changes in $H2^*$ due to attack angle, no vehicles .....	84
Figure 3.78: Changes in $H3^*$ due to attack angle, no vehicles .....	84
Figure 3.79: Changes in $H4^*$ due to attack angle, no vehicles .....	85
Figure 3.80: Variation of $A1^*$ showing the mean, upper and lower 2 standard deviations.....	86
Figure 3.81: Variation of $A2^*$ showing the mean, upper and lower 2 standard deviations.....	86
Figure 3.82: Variation of $A3^*$ showing the mean, upper and lower 2 standard deviations.....	87

Figure 3.83: Variation of A4* showing the mean, upper and lower 2 standard deviations.....	87
Figure 3.84: Variation of H1* showing the mean, upper and lower 2 standard deviations.....	88
Figure 3.85: Variation of H2* showing the mean, upper and lower 2 standard deviations.....	88
Figure 3.86: Variation of H3* showing the mean, upper and lower 2 standard deviations.....	89
Figure 3.87: Variation of H4* showing the mean, upper and lower 2 standard deviation .....	89
Figure 3.88: Variation of A1* showing the mean, upper and lower 2 standard deviations.....	90
Figure 3.89: Variation of A2* showing the mean, upper and lower 2 standard deviations.....	90
Figure 3.90: Variation of A3* showing the mean, upper and lower 2 standard deviations.....	91
Figure 3.91: Variation of A4* showing the mean, upper and lower 2 standard deviations.....	91
Figure 3.92: Variation of H1* showing the mean, upper and lower 2 standard deviations.....	92
Figure 3.93: Variation of H2* showing the mean, upper and lower 2 standard deviations.....	92
Figure 3.94: Variation of H3* showing the mean, upper and lower 2 standard deviation .....	93
Figure 3.95: Variation of H4* showing the mean, upper and lower 2 standard deviations.....	93
Table 2.1: Model and prototype bridge specifications and properties .....	12
Table 2.2: Model experimentally determined properties .....	20
Table 2.3: Vehicle model specifications and dimensions (cm).....	21
Table 2.4: Test scenarios and wind speeds .....	26
Table 3.1: SDOF statistical results for A2* and A3*.....	39
Table 3.2: SDOF statistical results for H1* and H4*.....	39
Table 3.3: MDOF statistical results for A1* and A2* .....	40
Table 3.4: MDOF statistical results for A3* and A4* .....	40
Table 3.5: MDOF statistical results for H1* and H2* .....	40
Table 3.6: MDOF statistical results for H3* and H4* .....	41

# CHAPTER 1

## 1.1 Introduction

It is well known that the study of aeroelastic effects on bridge structures came into the spot light with the failure of the Tacoma Narrows Bridge. The following in-depth studies of the Tacoma Narrows failure laid the foundation for the current understanding of aeroelastic effects on structures. The failure also led to the common practice of wind tunnel testing of long span bridges to further understand the aerodynamic and aeroelastic behavior of bridge decks. This thesis will focus on experimentally investigating the aerodynamic performance of a slender long-span bridge with stochastic traffic. The thesis is made of four chapters. Chapter 1 will briefly introduce the background information about wind aerodynamics on bridges. In Chapter 2, the experimental design and setup will be introduced. Detailed experimental testing results and extensive analysis will be reported in Chapter 3. Finally, discussions and a summary will be made in Chapter 4.

## 1.2 Long-span Bridge Aerodynamics

Throughout the world lighter, slender and longer long-span bridges have been proposed and built such as the current long span record holder, Akashi Kaikyō Bridge in Japan with a 1,991 meter main-span. The design control is more critical as the current long-span bridge designs exhibit large slenderness ratios, flexibility and low structural dampening. Currently feasibility studies have been implemented to explore spans of up to 5,000 meters (Ge & Xiang, 2008).

### 1.2.1 Aerodynamics and Aeroelastic Effect

Wind includes laminar (or smooth) and turbulent flow components. For slender long-span bridges, both laminar and turbulent-induced wind loads will cause the bridge to experience dynamic vibration. For instance buffeting is caused by the unsteady loading on a structure due to velocity fluctuations in the approaching wind. Flow-induced vibration of the bridge deck as a result of aerodynamic effects will modify the flow around the bridge deck, which in turn will change the wind load on the bridge deck. Such a flow-structure interaction is called aeroelastic effect. Aeroelasticity refers to the interaction of the inertial, elastic, and aerodynamic forces acting on structural elements exposed to wind flow. The aerodynamic pressure force and skin friction lead to the aerodynamic effect caused by the irregular nature of the wind and its interaction with the bridge structure. Some of the aerodynamic effects include, vortex shedding, cross-wind galloping, and buffeting which can be detrimental to the performance of a bridge structure. Depending on the profile of the cross-section of the bridge deck, the increase of wind speeds typically lead to aeroelastic instability. When the aeroelastic effect continues to get stronger, at some point, the bridge may experience amplified self-excited oscillatory motion due to the aerodynamic forces, which is called flutter (Simiu & Scanlan, 1996). Flutter is essentially a stability problem, which will cause the bridge to experience excessive and amplified vibration until failure. The well-known failure of the Tacoma Narrows Bridge is a good example of aeroelastic effect.

Due to the complexness of aeroelastic instability, to date, there is no absolute theoretical approach which can fully characterize the nature. The state-of-the-art will still depend on some critical variables, such as flutter derivatives which are usually obtained from wind tunnel tests or computational fluid dynamics (CFD). In addition to flutter derivatives which characterize the dynamic effect of wind, there are also static fluid (wind) force coefficients. Some basic

information of the static fluid (wind) force coefficients and the flutter derivatives will be briefly introduced in the following. For more details, people can refer to Ref. (Simiu & Scanlan, 1996).

### 1.2.2 Fluid (wind) Force Coefficients

The net wind-pressure forces  $F_L$  and  $F_D$  in the lift and drag directions respectively can be obtained from wind tunnel testing and then expressed in dimensionless terms of lift and drag coefficients  $C_L$  and  $C_D$  as (Simiu & Scanlan, 1996):

$$C_L = \frac{F_L}{\frac{1}{2}\rho U^2 B}$$

Equation 1.1

$$C_D = \frac{F_D}{\frac{1}{2}\rho U^2 B}$$

Equation 1.2

where  $B$  is a typical reference dimension of the structure such as the bridge deck width. The net flow induced moment  $M$  the corresponding coefficient is

$$C_M = \frac{M}{\frac{1}{2}\rho U^2 B^2}$$

Equation 1.3

### 1.2.3 Flutter Derivatives

The complete linearized flutter derivative formulation of the self excited forces on the three-degrees-of-freedom can be written as: (Sarkar, et al, 1994)

$$L_{se} = \frac{1}{2} \rho U^2 B \left[ KH_1^* \left( \frac{\dot{h}}{U} \right) + KH_2^* B \left( \frac{\dot{\alpha}}{U} \right) + K^2 H_3^* \alpha + K^2 H_4^* \frac{h}{B} + KH_5^* \left( \frac{\dot{p}}{U} \right) + K^2 H_6^* \left( \frac{p}{B} \right) \right]$$

Equation 1.4

$$M_{se} = \frac{1}{2} \rho U^2 B^2 \left[ KA_1^* \left( \frac{\dot{h}}{U} \right) + KA_2^* B \left( \frac{\dot{\alpha}}{U} \right) + K^2 A_3^* \alpha + K^2 A_4^* \frac{h}{B} + KA_5^* \left( \frac{\dot{p}}{U} \right) + K^2 A_6^* \left( \frac{p}{B} \right) \right]$$

Equation 1.5

$$D_{se} = \frac{1}{2} \rho U^2 B \left[ KP_1^* \left( \frac{\dot{p}}{U} \right) + KP_2^* B \left( \frac{\dot{\alpha}}{U} \right) + K^2 P_3^* \alpha + K^2 P_4^* \frac{p}{B} + KP_5^* \left( \frac{\dot{h}}{U} \right) + K^2 P_6^* \left( \frac{h}{B} \right) \right]$$

Equation 1.6

where  $\rho$  = air density;  $B$  = width of the bridge deck;  $K = B\omega/U$  reduced frequency;  $\dot{h}$ ,  $\dot{\alpha}$  and  $\dot{p}$  = velocities; and  $A_i^*$ ,  $H_i^*$  and  $P_i^*$ , where  $i = 1-6$  are non-dimensional functions of the reduced velocity ( $= 1/K$ ) known as flutter derivatives. Typically for bridge deck analysis the  $A_{5,6}^*$ ,  $H_{5,6}^*$  and  $P_i^*$  terms are neglected as their effects are assumed to be small (Sarkar, et al, 1994).

### 1.3 Wind Tunnel Experiments

The wind tunnel experimental approach is about testing the scaled model of the structure in a simulated environment to reproduce the real world behavior. The challenge lies in replicating the environmental conditions the prototype bridge experiences at its geographic location. It is recognized that laboratory flow will never perfectly match real world atmospheric flow. In addition to the atmospheric environment being reproduced in a similar manner, the structure under study should be modeled with the similarity criteria (Simiu & Scanlan, 1996). The characteristics of wind fields should consider: (1) the variation of the mean wind speed with

height; (2) the variation of turbulence intensities and integral scales with height; and (3) the spectra and cross-spectra of turbulence in the along-wind, across-wind, and vertical directions.

It is crucial to simulate rational boundary layer in wind tunnels. There are three types of wind tunnels typically used: long tunnels (boundary layer tunnel), short wind tunnels and those tunnels with active devices. Generally, the long wind tunnel achieves better atmospheric turbulence simulation due to the long test section to develop desired boundary layer conditions. The best results are achieved by using a long wind tunnel with passive devices placed at the test section entrance, such as grids, barriers, fences and spires to simulate turbulent atmospheric conditions (Simiu and Scanlan 1986).

To date, the use of wind tunnels is a necessary tool to perform physical experiments to gain further understanding into the numerous complex effects coupled with fluid flow (Simiu & Scanlan, 1996). In the design of long span bridges it is typical to use section models and/or full structure model in the wind tunnel tests. However, with the ever increasing span length of long span bridges, a smaller scale has to be used for the full bridge models. As a result, the Reynolds number becomes questionable for smaller scale models (Scanlan R. , 1978). The use of section models has proven to be cost effective to appropriately detail the bridge deck geometry and obtain the aerodynamic and aeroelastic characteristics for a particular bridge cross-section.

One of the key aspects is to be able to correlate the wind tunnel testing results of the model with the prototype of the structure. This is accomplished by using the basic scaling considerations:

$$\left(\frac{\rho_s}{\rho_f}\right)_m = \left(\frac{\rho_s}{\rho_f}\right)_p$$

Equation 1.7

where  $\rho_s$  and  $\rho_f$  are the densities of the structure and the fluid, respectively, and the subscripts  $m$  and  $p$  refer to the model and prototype respectively. This holds true for the geometric ratios and shapes between the model and prototype. There are also three chosen ratios such as length scale:

$$\lambda_L = \frac{D_m}{D_p}$$

Equation 1.8

The second choice, which may also be controlled by the wind tunnel capacity, is the velocity scale.

$$\lambda_V = \frac{U_m}{U_p}$$

Equation 1.9

The third choice depending on testing circumstances is the density scale,

$$\lambda_\rho = \frac{\rho_m}{\rho_p}$$

Equation 1.10

typically  $\lambda_\rho = 1$  as the air density of the testing facility is similar to that of the air surrounding the prototype.

#### 1.4 The State-of-the-Art of Bridge Section Model Tests

During the past couple decades, most studies were focused on deciding 6 or 8 flutter derivatives by looking at vertical and torsion motions (two degrees of freedom)(2-DOF) due to the inherent strong coupling. In more recent tests researchers have looked at determining all 18 flutter derivatives from a three-degree-of-freedom (3-DOF) elastic suspension system designed for

section model testing in wind tunnels (Sarkar, et al, 2003). Along with the new 3-DOF elastic suspension system, Chowdhury and Sarkar (2003) felt the need for an improved method of obtaining the 18 flutter derivatives. The development of a new system identification method known as iterative least squares method (ILS). The ILS-method uses the free vibration time histories obtained from wind tunnel testing using the new elastic suspension system on a section model to calculate the 18 flutter derivatives. The elastic suspension system used pneumatic bushings riding on polished steel rods to minimize frictional resistance and provide stability in the horizontal and vertical direction. Torsional assemblies were attached to both sides to allow for torsional movement. The study showed that it was far more challenging extracting flutter derivatives from a 3-DOF system; however the apparatus allowed for the constrained motion in any one degree or 2-DOF to further validate the 3-DOF analysis. The system proved successful in determining the 18 flutter derivatives for an airfoil using the 3-DOF elastic suspension system (Chowdhury & Sarkar, 2003).

For all the wind tunnel testing summarized above, the bridge section model is empty, in other words, there is no vehicle on the bridge deck. Obviously this is different from reality as traffic remains on slender long-span bridges most of the time. By tracing back to the origin of such an approximation, it is believed that it was originally for simplification purposes as well as the justification for a section model test. Basically, the assumption that flutter derivatives obtained from a section model can represent the whole bridge is based on the fact of uniform bridge deck profile along the span. With the presence of vehicles, the bridge deck profile will actually be changed. Due to the random nature of the distribution of individual vehicles along the bridge, the profiles of any bridge section with vehicles essentially vary from one another. However, if traffic is modeled on full bridge models in a wind tunnel, the vehicle models will be too small to provide enough details of the profiles. This dilemma poses challenges on experimentally investigating wind coefficients of bridge decks with traffic.

Not until recently, have there been limited studies which tried to consider vehicles on a bridge section model tests such as the wind-vehicle-bridge (WVB) model created by Li et al. (2009) represented a multi-track passenger railway bridge. WVB test were unique as a testing apparatus was built to look at the bridge and the vehicles moving on the bridge under crosswind conditions. The bridge and vehicle systems were equipped with force balance devices to measure the lift, drag, and moment coefficients. Several scenarios were examined such as vehicle position, speed, and size (additional train cars). The lift, drag and moment coefficients were then compared with the base line coefficients, where it could be seen that different scenarios increased and decreased the coefficients on both the bridge and vehicle. Based on the results it could be seen that relative locations between the bridge and vehicle have a definite impact on the aerodynamic characteristics of the bridge section model (Li, et al, 2009).

A case study on the Luling Bridge Section model (1/92 scale) with different traffic patterns was carried out by Cai et al. (2010). The study used mid-sized SUV/minivan as the standard vehicle and looked at three scenarios, the bridge section with all four lanes bumper to bumper traffic, two upstream lanes bumper to bumper traffic and two downstream lanes with bumper to bumper traffic. The flutter derivatives of all three cases were then compared to that of the empty bridge, to illustrate the changes of the bridge section aerodynamic performance (Cai, et al, 2010). All the existing studies either only tested several scenarios with assumed patterns of vehicle distributions on the bridge or the vehicle model was too small.

## **1.5 Significance of the Study**

The AASHTO LRFD Bridge Design Specification was primarily developed from bridges with spans shorter than 60 meters (AASHTO, 2007). For long-span bridges, they are typically individually designed and verified with extensive wind tunnel testing. However, as discussed

above, most existing wind tunnel tests neglected the aerodynamic wind effects on vehicles coupled with the bridge due the traditional assumption that the bridge would be empty during high wind situations. This is related to the benchmark of 90 km/hr wind velocity in which it is assumed that the bridge will be closed to traffic in the LRFD specification (AASHTO, 2007). With ever changing weather, natural disasters, valuable commerce and supplies traveling over many long-span bridges throughout the United States, the reality is that the bridges are usually not closed and there are still many vehicles on the bridges even with pretty high wind velocities. An extreme instance would be emergency evacuations due to a severe storm such as a hurricane or large natural disaster. Many long span bridges are located on critical arteries that would be experiencing extreme traffic volumes along with severe environmental conditions. Further understanding of a bridge's continued performance and functionality under such conditions are of great importance to engineers in providing safety and reliability to the public. Therefore, to rationally evaluate the aerodynamic performance of a bridge deck, the appropriate traffic model would be an integral part to any safety or serviceability study. As a critical step for the aerodynamic performance assessment, wind tunnel tests of a bridge deck with vehicle models representing stochastic traffic will be conducted in the present study.

## CHAPTER 2 EXPERIMENTAL DESIGNS

### 2.1 Bridge Model Design

The dimensions of the model section were initially determined by examining the test section of the industrial wind tunnel (IWT). The IWT has a working section of 1.8m by 1.8m with a maximum access window of 1.08m by 1.14m. The dimensions of the access window openings were also used to determine an appropriate maximum scale for the section model to fit within the tunnel, which was found to be 1/36. The dimensions of the section model were then decided based on the prototype which shares a similar profile of the cross section of the Luling Bridge in St. Charles Parish, Louisiana. The frequencies are different from the actual ones of the Luling Bridge. Based on the initial model parameters an estimated model mass 18-kg was used to determine the appropriate springs in which to suspend the model. The desired vertical natural frequency ( $f_v$ ) was then used to get the spring constant from Equation 2.11:

$$f_v = \frac{1}{\tau} = \frac{1}{2\pi} \sqrt{\frac{k}{m}} \text{ or } k = (2\pi f_v)^2 m$$

**Equation 2.11**

where  $\tau$  = period,  $m$  is the model mass and  $k$  is the spring constant which is divided by eight (the number of springs suspending the section model). Furthermore the torsional distance ( $d$  = spring spacing) needed to be confirmed using the desired torsional natural frequency ( $f_a$ ) and the spring constant determined from the vertical frequency.

In Figure 2.1 the free body diagram (FBD) is illustrated for the section model setup. Summing the moments about the centroid results in:

$$\sum M_c = I_c \ddot{\theta} \Rightarrow \left(-4k \frac{d}{2} \theta\right) \frac{d}{2} - \left(4k \frac{d}{2} \theta\right) \frac{d}{2} = I_c \ddot{\theta}$$

Equation 2.12

Eq. (2.2) can be simplified to:  $I_c \ddot{\theta} + 2kd^2 \theta = 0 \Rightarrow \ddot{\theta} + \frac{2kd^2 \theta}{I_c}$

Equation 2.3

The torsional frequency of the model can be obtained as:

$$f_\alpha = \frac{\omega_n}{2\pi} = \frac{\sqrt{\frac{2kd^2}{I_c}}}{2\pi}$$

Equation 2.4

or

$$d = f_\alpha 2\pi \sqrt{\frac{I_c}{2k}}$$

Equation 2.5

where  $\omega_n$  is the natural circular frequency. The processes is partially iterative as the moment of inertia typically differs slightly from the experimentally determined moment of inertia and possibly the mass may differ if the mass of the springs is neglected. To properly account for the springs an effective mass was found to be 1/3 the mass of the springs suspending the section

model which then can be added to the section model mass to find the total mass of the system.

The prototype and theoretical section model properties are listed in Table 2.1.

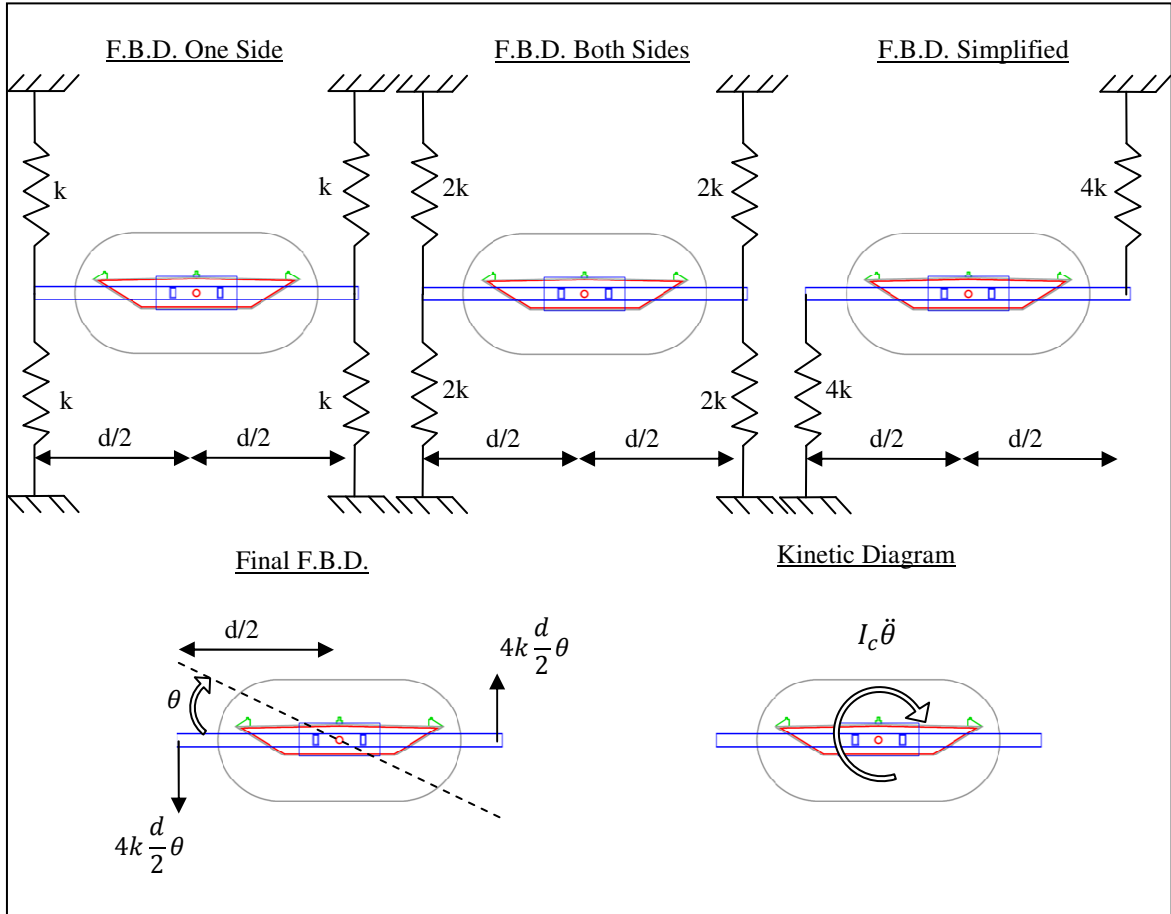


Figure 2.1: Free Body Diagram progression of section model to determine torsional distance

Table 2.1: Model and prototype bridge specifications and properties

Parameter	Label	Prototype	Unit	Scale Ratio	Model	Unit
Length	L	62.23	m	1/36	1.729	m
Width	B	28.01	m	1/36	0.778	m
Height	H	4.92	m	1/36	0.137	m
Mass/unit length	M	18072	kg/m	$\sim 1/36^2$	11.445	kg/m
Mass Moment of Inertia	$I_m$	796050	kg m <sup>2</sup> /m	$\sim 1/36^4$	0.3909	kg m <sup>2</sup> /m
1st Bending Frequency	$f_v, n1$	0.429	Hz	9/1	3.861	Hz
1st Torsional Frequency	$f_\alpha, n2$	1.078	Hz	9/1	9.702	Hz
Damping Ratio	$\zeta$	0.01				

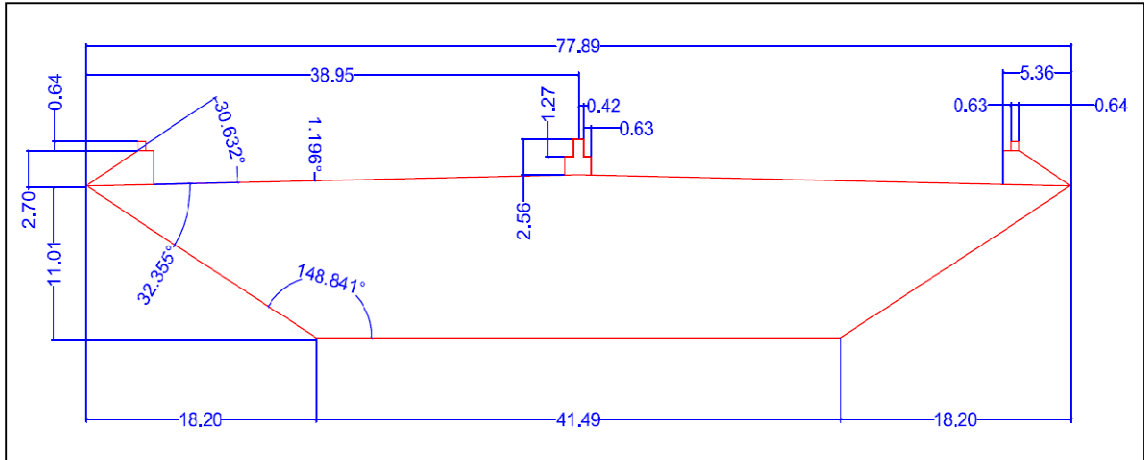


Figure 2.2: Dimensioned cross-section of the bridge section model (cm)

In Figure 2.2, the cross-sectional dimensions for the bridge section model are based on the assembly drawings of the Luling Bridge. The model was initially constructed out of wood and copper as both materials were easy to work with and required no specialty contractor to construct the model seen in Figure 2.3. During the preliminary testing it was determined the copper was not sufficiently stiff to provide accurate results. The copper mounting material was then replaced with aluminum in the revised mounting configuration as shown in Figs. 2.4-5.

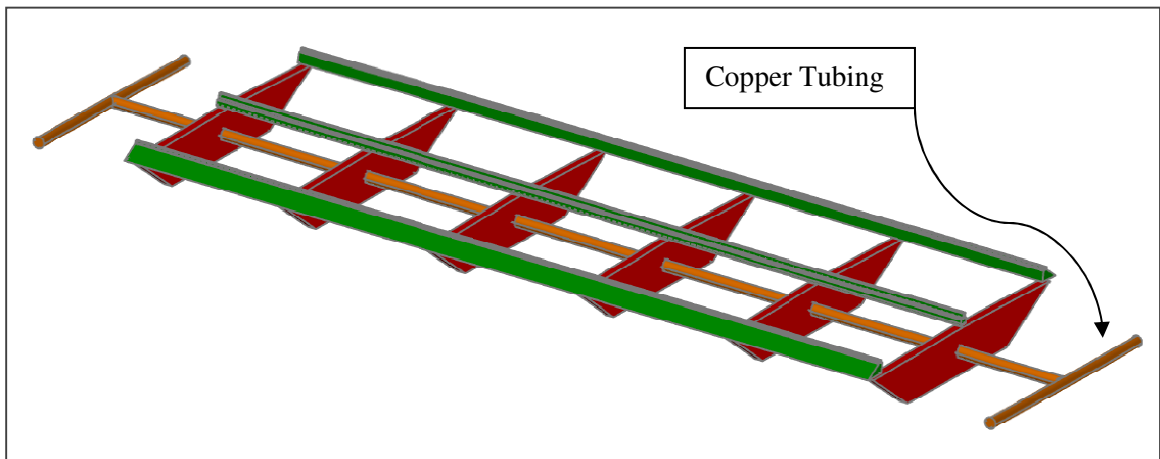


Figure 2.3: Original copper supports built into bridge section model

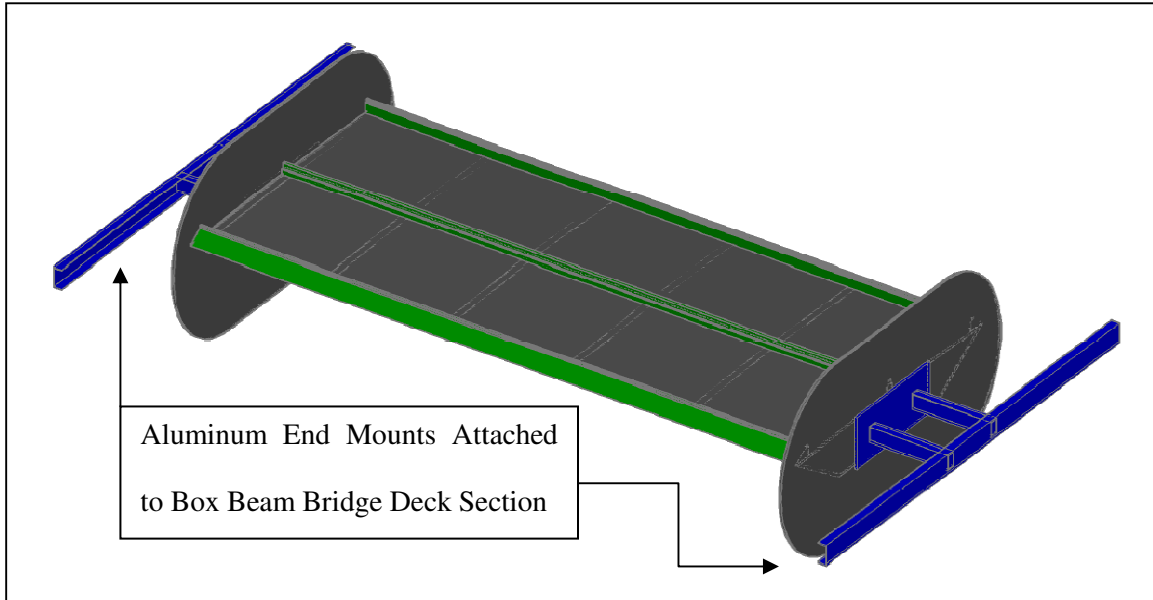


Figure 2.4: 3D view of sectional bridge deck model

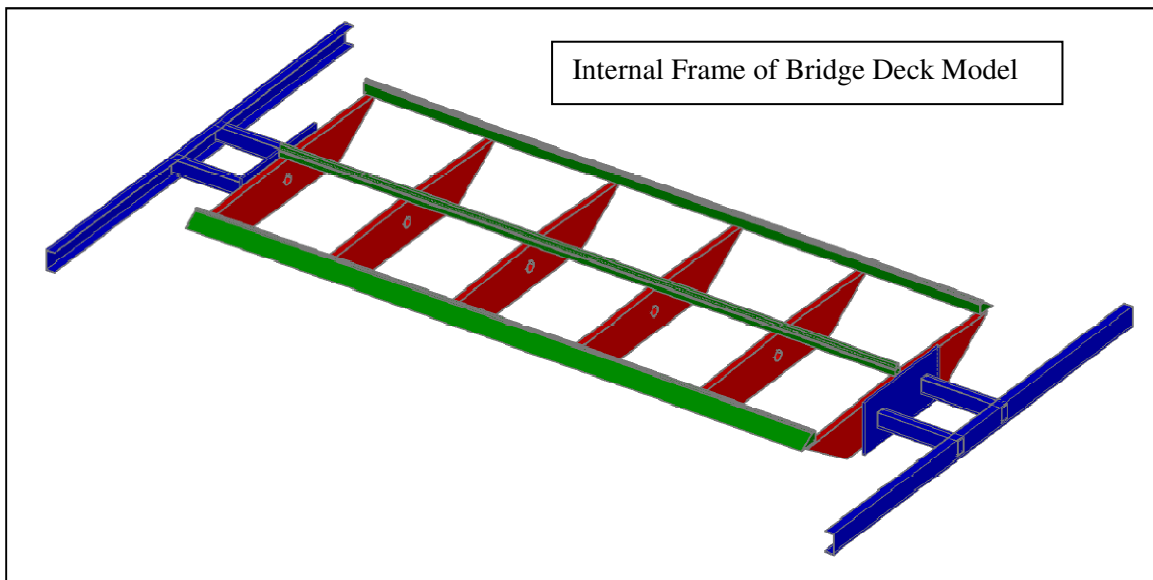
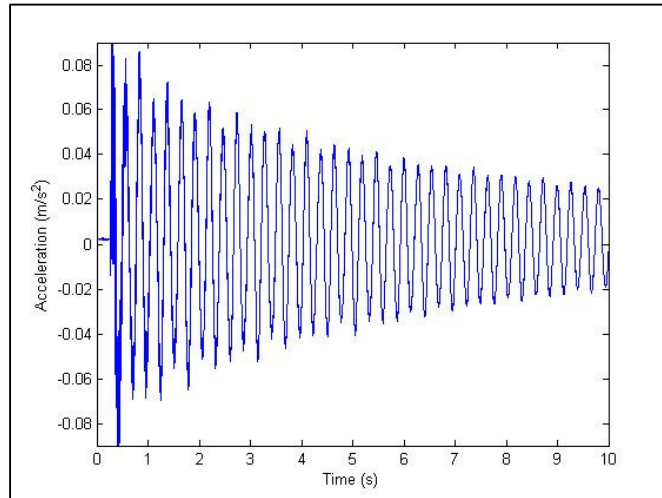


Figure 2.5: 3D view of sectional bridge deck model with removed plywood skin and end plates

The new configuration resulted in a critical damping ratio for the vertical and torsional motions of 0.0009. For testing purposes a critical damping ratio of approximately 0.005 is desired, so a viscous damping apparatus was attached to each side of the model as shown in Figure 2.8.

During the zero wind velocity testing the critical damping ratios were near 0.0055. Once the model was installed in the wind tunnel and the piano wires were attached the critical damping ratios increased slightly seen in Table 2.2. The increased damping came from the attachment of the piano wires which created additional small amount of mechanical damping. The critical damping ratios were determined by using time history plots from the accelerometers as shown in Figure 2.6 and 2.7.



**Figure 2.6: Vertical time history, no wind**

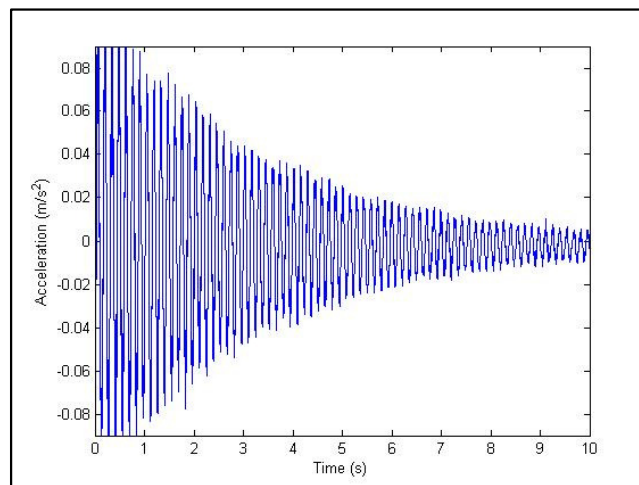


**Figure 2.7: Torsional time history, no wind**

The logarithmic decrement, from and Equation 2.15 was then used to calculate the critical damping ratio for vertical and torsional motions along with confirming the frequencies (Thomson & Dahleh, 1993).

$$\delta = \frac{2\pi\zeta}{\sqrt{1 - \zeta^2}}$$

**Equation 2.13**

where  $\zeta$  is the critical damping ratio for either vertical or torsional motion, as  $\zeta$  gets small  $\sqrt{1 - \zeta^2} \cong 1$ , and an approximate equation becomes:

$$\delta = 2\pi\zeta$$

**Equation 2.14**

for the time history the amplitude ratio for any two consecutive cycles is  $x_1/x_2 = e^\delta$  or  $x_0/x_n = e^{n\delta}$  for  $n$  representing the number of cycles. Solving the ratio equation for the logarithmic decrement then results in the following Equation 2.15.

$$\delta = \frac{1}{n} \ln \left( \frac{x_0}{x_n} \right)$$

**Equation 2.15**

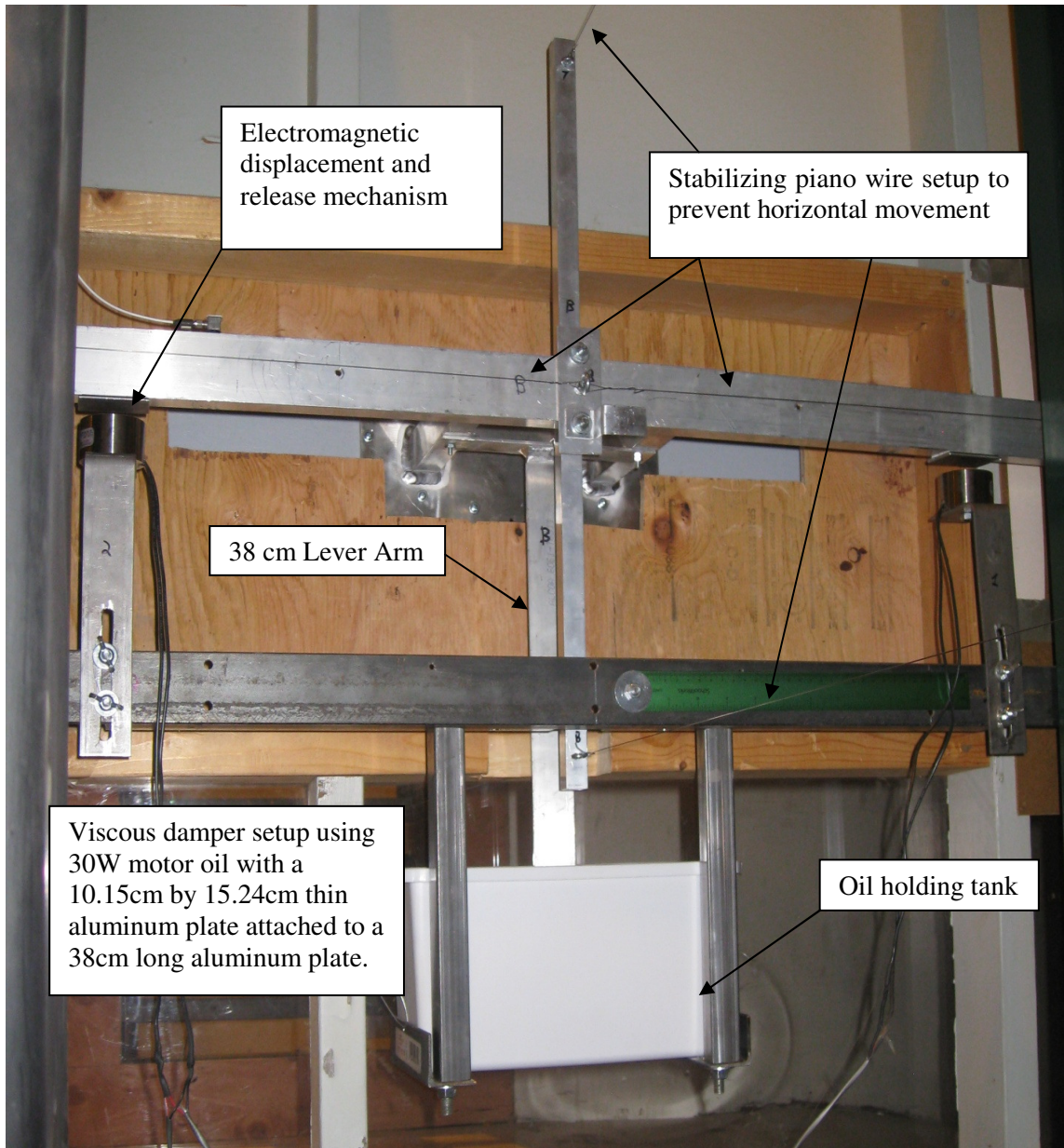


Figure 2.8: West side picture of model setup in wind tunnel frame



**Figure 2.9: Picture of bridge section in the Industrial Wind Tunnel**

The experimentally determined properties listed in Table 2.2 came from the initial zero wind velocity testing once the section model was setup in the wind tunnel. Several time histories were recorded for the section model. The section models were re-tested with additional steel bars placed on the top of the section model with the known mass and mass moment of inertia. The time histories allowed for the extraction of the  $f_v, f_a$  natural frequencies and  $f'_v, f'_a$  representing the changed natural frequencies of the section model due to the steel bars. The following steps and equations were used:

Step 1: Write out the equations for the natural frequencies.

$$f_v = \frac{1}{2\pi} \sqrt{\frac{k_v}{m}} \quad f'_v = \frac{1}{2\pi} \sqrt{\frac{k_v}{m + \Delta m}} \quad f_\alpha = \frac{1}{2\pi} \sqrt{\frac{k_\alpha}{I}} \quad f'_\alpha = \frac{1}{2\pi} \sqrt{\frac{k_\alpha}{I + \Delta I}}$$

Step 2: Re-write equations solving for  $k_v$  and  $k_\alpha$ .

$$k_v = m(2\pi f_v)^2 \quad k_v = (m + \Delta m)(2\pi f'_v)^2 \quad k_\alpha = I(2\pi f_\alpha)^2 \quad k_\alpha = (I + \Delta I)(2\pi f'_\alpha)^2$$

Step 3: Simplify equations by plugging in the known frequencies and the change of mass and mass moment of inertia and solving for original mass and mass moment of inertia.

$$\frac{m}{m + \Delta m} = \frac{f_v'^2}{f_v^2} \quad \frac{I}{I + \Delta I} = \frac{f_\alpha'^2}{f_\alpha^2}$$

The experimentally-determined properties in Table 2.2 differ slightly from the theoretical values in

Table 2.1. The small variations were expected, but care must be taken when determining the natural frequencies  $f_v$ ,  $f_\alpha$  and  $f'_v$ ,  $f'_\alpha$  as the calculations are very sensitive to small changes in frequency that could result in large differences in the calculated mass and mass moment of inertia. The larger difference seen for the mass moment of inertia was believed to be caused by the composite box beam design of the bridge section model resulting in an approximate theoretical mass moment of inertia value. The torsional frequency was also reduced purposely due to wind tunnel velocity constraints.

**Table 2.2: Model experimentally determined properties**

Parameter	Label	Prototype (SI)	Unit
Mass Moment of Inertia	$I_m$	0.764	kg m <sup>2</sup> /m
1st Bending Frequency	$f_v, n1$	3.68	Hz
1st Torsional Frequency	$f_a, n2$	7.01	Hz
Mass/unit length	$M$	11.511	kg/m
Critical Damping Ratio	$\zeta_v$	0.00585	Vertical
Critical Damping Ratio	$\zeta_a$	0.00827	Torsional

## 2.2 Vehicle Model Design

In determining the vehicle model design the goal was to have an accurate representation of typical traffic flows. The following five vehicles were chosen as shown in Table 2.3, to represent the diversity of vehicles typically seen on a roadway. The vehicle masses were scaled down by using Equation 2.16, in which the  $M_r$  and  $M_m$  were average mass of the real vehicle and mass of the model respectively.

$$M_r \div 36^3 \times (\lambda_{mp}) = M_m$$

**Equation 2.16**

The air density scale in Equation 1.7 and the density scale comparing the model to the prototype mass ratio were examined to appropriately scale the vehicle masses. The prototype bridge being located at the sea level and the model testing conducted at the CSU Engineering Research Center (ERC) at 1,525m in elevation resulted in an air density scale of ( $\lambda_p = 0.86$ ) and the final mass ratio of constructed model to prototype was ( $\lambda_{mp}$ ) 0.82. The model to prototype mass ratio was chosen as the reduction factor as lighter models allow for a more measureable response at reduced wind velocities.

The vehicle models were constructed from foam, initially cut with a hot wire knife then sanded and painted to remove any excess roughness. Several small holes were drilled from the bottom of the models to insert steel BB's to achieve the desired mass. In the end, the models of four semi trucks, five delivery trucks, 10 large SUVs, 10 SUVs and 14 cars were manufactured in Table 2.3 to allow for a multitude of different traffic scenarios. A picture of all the vehicles can be seen in Figure 2.10.

**Table 2.3: Vehicle model specifications and dimensions (cm)**

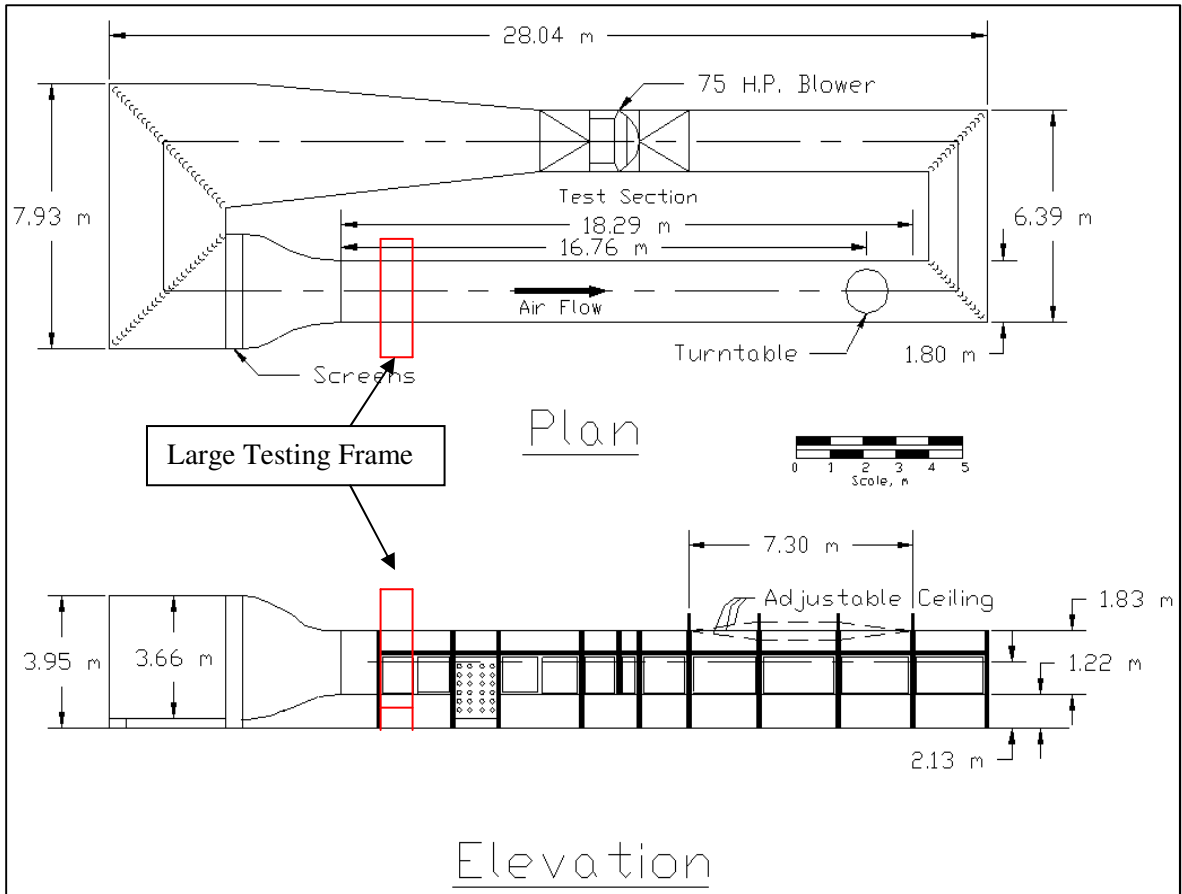
Vehicle Type & Specifications	Vehicle Outline
<p style="text-align: center;">Semi Truck</p> <p>Model Weight = 400 g Actual Weight = 22,730 kg Scale = 1/36</p>	
<p style="text-align: center;">Delivery Truck</p> <p>Model Weight = 160 g Actual Weight = 9,090 kg Scale = 1/36</p>	
<p style="text-align: center;">Large SUV</p> <p>Model Weight = 56 g Actual Weight = 3,180 kg Scale = 1/36</p>	
<p style="text-align: center;">SUV</p> <p>Model Weight = 44 g Actual Weight = 2,500 kg Scale = 1/36</p>	
<p style="text-align: center;">Car</p> <p>Model Weight = 30 g Actual Weight = 1,730 kg Scale = 1/36</p>	



Figure 2.10: Photograph of model vehicles

### 2.3 Equipment & Test Setup

All the tests were conducted at the Engineering Research Center in the Wind Engineering and Fluids Laboratory at Colorado State University. The Industrial Aerodynamics Wind Tunnel (IWT) was utilized, which has the capacity to continuously vary wind speeds up to 24 m/s. The layout and dimensions of the IWT can be seen in Figure 2.11.



**Figure 2.11: Industrial Aerodynamics Wind Tunnel at Colorado State University**

The large testing frame roughly located in Figure 2.11 was used as the base to configure and mount a smaller mobile frame that was as close to the perimeter of the wind tunnel as possible. The design goal of the mobile frame was to provide a rigid mounting point to suspend the bridge section and be usable with or without the wind tunnel. The frame would serve multiple roles allowing for static tests to be performed while the wind tunnel was in use, and then could be easily moved for educational demonstrations later on. The complete mobile frame can be seen in Figure 2.12. When installed for wind tunnels testing the mobile frame bracing members were removed and the base was bolted to the larger frame and smaller bracing members attached to the wind tunnel to provide required support.

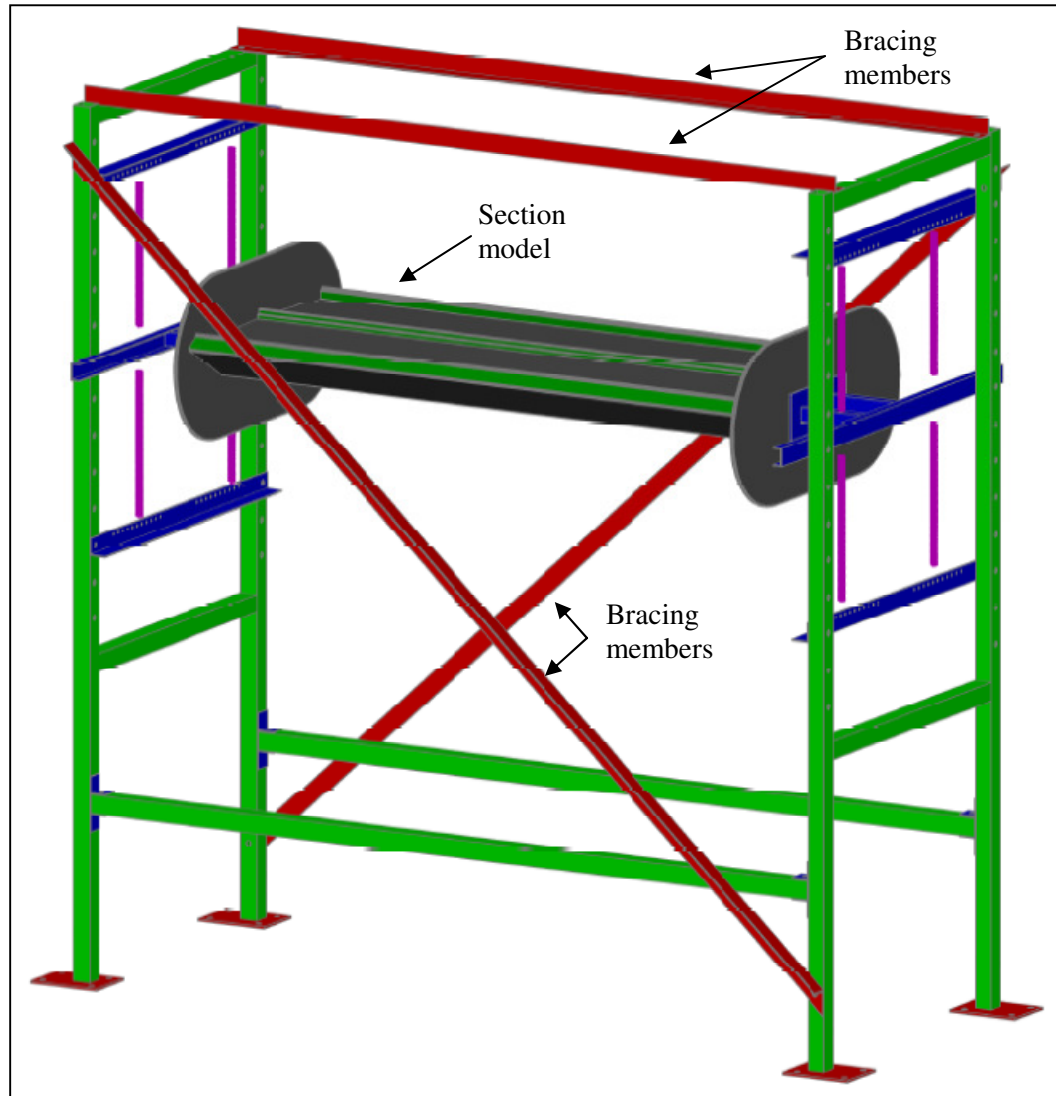


Figure 2.12: Mobile support frame for bridge section model

The basic setup for the section model test consists of the following:

- The section model was suspended from eight linear extension springs allowing for the 2-DOF being torsion and vertical motions.
- The horizontal movement parallel and perpendicular to the wind flow direction was restrained by the use of piano wires as shown in Figure 2.13.

- An electromagnetic release mechanism was utilized to provide the initial displacement and simultaneous release of both sides of the model in pure torsion, vertical and couple motion depending on the test requirements.
- A pitot tube connected to an electronic manometer was used to measure the mean wind velocity. The pitot tube was positioned downstream of the section model and positioned centrally in the wind tunnel.
- A computerized data acquisition system was utilized, which consisted of using LabView Signal Express by National Instruments (NI), coupled with NI data logger which connected to three NI accelerometers attached to the bridge section (Figure 2.13).

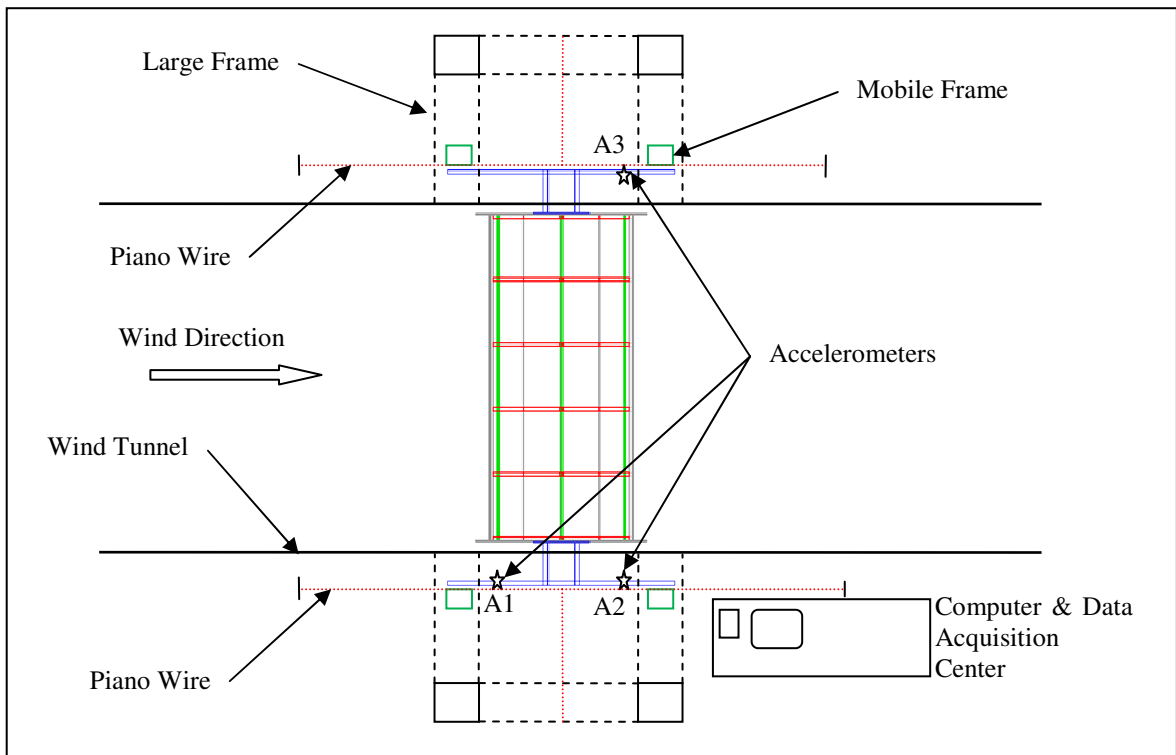


Figure 2.13: Top view of bridge section mounted in wind tunnel

## 2.4 Test Scenarios

There were 26 different test scenarios chosen, which are listed in Table 2.4. Each scenario was tested for a given set of velocities, with each velocity test repeated three times to reduce random error in the data. The tests scenarios were determined by examining four main categories, the first being the control group consisting of several bridge section tests with no vehicles observing pure torsion and vertical motion along with coupled motion. The second group involved the extreme cases bumper to bumper traffic both-sides, bumper to bumper windward side only and bumper to bumper leeward side only. The third group looked at snapshots of stochastic spatial dependent traffic flows and the forth group looked at stochastic time dependent traffic flows.

**Table 2.4: Test scenarios and wind speeds**

Test Name	Description	Wind Speeds (m/s)	Number of Tests	Observed Buffeting or Vortex Shedding
TOR_ATZ	Coupled, 0 degree, no vehicles	0,2,4,6,8,10,12	21	
TOR_ATK3P	Coupled, +3 degree, no vehicles	0,2,4,6,8,10,12	21	6 m/s
TOR_ATK3N	Coupled, -3 degree, no vehicles	0,2,4,6,8,10,12	21	
TOR_AT3N_BBER	Coupled, -3 degree, bumper to bumper both sides	0,2,4,6,8,10,12	21	
TOR_AT3N_BBVD	Coupled, -3 degree, bumper to bumper vehicles leeward side only	0,2,4,6,8,10,12	21	
TOR_AT3N_BBVU	Coupled, -3 degree, bumper to bumper vehicles windward side only	0,2,4,6,8,10,12	21	
TOR_AT3P_BBER	Coupled, +3 degree, bumper to bumper both sides	0,2,4,6,8,10,12	21	4 m/s
TOR_AT3P_BBVD	Coupled, +3 degree, bumper to bumper vehicles leeward side only	0,2,4,6,8,10,12	21	
TOR_AT3P_BBVU	Coupled, +3 degree, bumper to bumper vehicles windward side only	0,2,4,6,8,10,12	21	4 m/s
TOR_ATZ_BBER	Coupled, 0 degree, bumper to bumper both sides	0,2,4,6,8,10,12	21	4 m/s
TOR_ATZ_BBVD	Coupled, 0 degree, bumper to bumper vehicles leeward side only	0,2,4,6,8,10,12	21	6 m/s
TOR_ATZ_BBVU	Coupled, 0 degree, bumper to bumper vehicles windward side only	0,2,4,6,8,10,12	21	
TOR_STC21	Coupled, 0 degree, Spatial Case #2.1 20 veh/km/ln	0,4,8,12	12	8 m/s
TOR_STC22	Coupled, 0 degree, Spatial Case #2.2 20 veh/km/ln	0,4,8,12	12	8 m/s
TOR_STC23	Coupled, 0 degree, Spatial Case #2.3 20 veh/km/ln	0,4,8,12	12	8 m/s
TOR_STC31	Coupled, 0 degree, Spatial Case #3.1 32 veh/km/ln	0,4,6,8,12	15	4 m/s
TOR_STC32	Coupled, 0 degree, Spatial Case #3.2 32 veh/km/ln	0,4,6,8,12	15	4 m/s
TOR_STC33	Coupled, 0 degree, Spatial Case #3.3 32 veh/km/ln	0,4,6,8,12	15	4 m/s
TOR_TT11	Coupled, 0 degree, Time Case #1.1 20 veh/km/ln	0,4,8,12	12	
TOR_TT12	Coupled, 0 degree, Time Case #1.2 20 veh/km/ln	0,4,8,10,12	15	8 m/s
TOR_TT13	Coupled, 0 degree, Time Case #1.3 20 veh/km/ln	0,4,8,10,12	15	8 m/s
TOR_TT21	Coupled, 0 degree, Time Case #2.1 32 veh/km/ln	0,4,8,10,12	15	8 m/s
TOR_TT22	Coupled, 0 degree, Time Case #2.2 32 veh/km/ln	0,4,6,8,12	15	4 m/s
TOR_TT23	Coupled, 0 degree, Time Case #2.3 32 veh/km/ln	0,4,6,8,12	15	4 m/s
VERT_ATZ	Pure Vertical, 0 degree, No vehicles	0,2,4,6,8,10	18	
PURE_TORSION	Pure Torsion, 0 degree, No vehicles	0,2,4,6,8,10,12	21	
Total =			459	

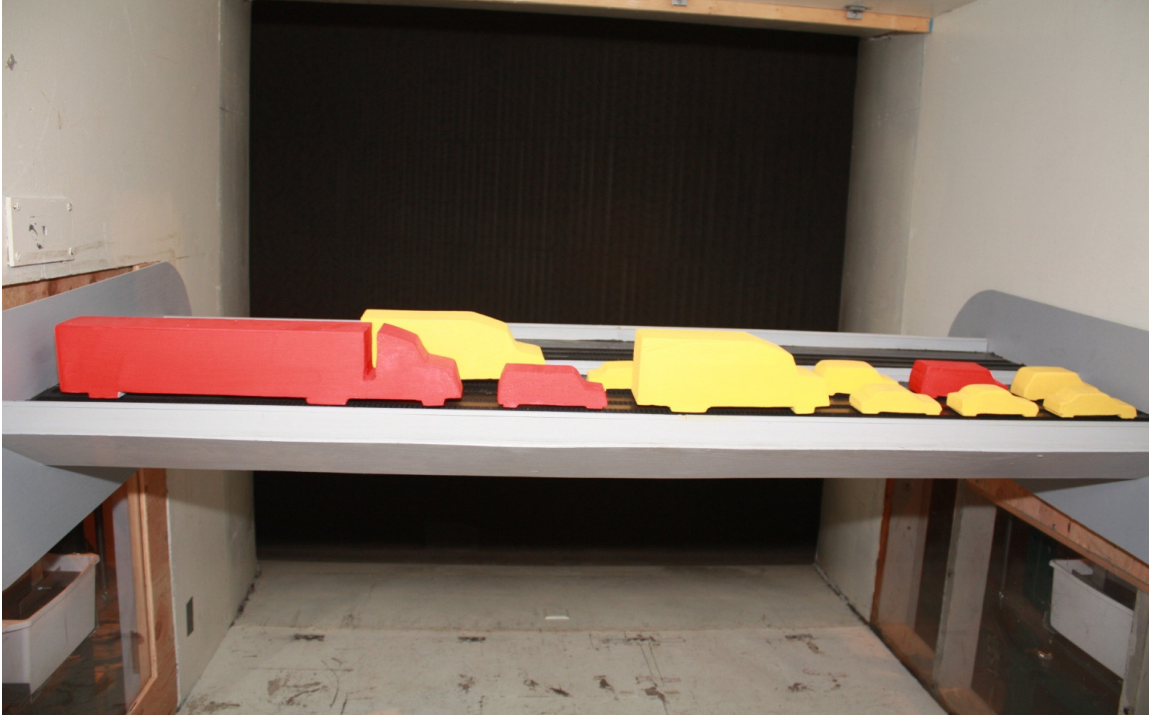


Figure 2.14: Photograph bumper to bumper leeward side traffic

## 2.5 Identification of Flutter Derivatives

In determining the flutter derivatives for the 2-DOF bridge section model the equations of motion about the center of mass can be written as follows:

$$m\ddot{h} + S\ddot{\alpha} + c_h\dot{h} + C_h h = L_{se}$$

Equation 2.17

$$S\ddot{h} + I\ddot{\alpha} + c_\alpha\dot{\alpha} + C_\alpha\alpha = M_{se}$$

Equation 2.18

where  $m$  and  $I$  are the mass and mass moment of inertia per unit length of the section model, respectively.  $S$  is the static unbalance (equal to the product of the mass  $m$  and the distance ( $a$ ) which separates the center of mass from the elastic center), vertical and torsional restoring forces characterized by the spring constant  $C_h$  and  $C_\alpha$ , the coefficients of viscous damping  $c_h$  and  $c_\alpha$ , the

$L_{se}$  and  $M_{se}$  are the self-excited forces of lift and moment respectively, which can be seen in their entirety in Equations 1.4 & 1.5 (Simiu & Scanlan, 1996) (see Figure 2.15 for illustration).

Furthermore the linear self excited aerodynamic forces can be written for 2-DOF as:

$$L_{se} = m_h [H_1 \dot{h} + H_2 \dot{\alpha} + H_3 \alpha + H_4 h]$$

Equation 2.19

$$M_{se} = I_\alpha [A_1 \dot{h} + A_2 \dot{\alpha} + A_3 \alpha + A_4 h]$$

Equation 2.20

The coefficients,  $H_i$  and  $A_i$  ( $i = 1-4$ ) are determined experimentally and be written utilizing a combination of Equations 1.4 & 1.5 along with Equations 2.12 & 2.13 in their non-dimensional form as follows:

$$\begin{aligned} H_1^* &= \frac{2m_h H_1}{\rho B^2 \omega} & A_1^* &= \frac{2I_\alpha A_1}{\rho B^3 \omega} \\ H_2^* &= \frac{2m_h H_2}{\rho B^3 \omega} & A_2^* &= \frac{2I_\alpha A_2}{\rho B^4 \omega} \\ H_3^* &= \frac{2m_h H_3}{\rho B^3 \omega^2} & A_3^* &= \frac{2I_\alpha A_3}{\rho B^4 \omega^2} \\ H_4^* &= \frac{2m_h H_4}{\rho B^2 \omega^2} & A_4^* &= \frac{2I_\alpha A_4}{\rho B^3 \omega^2} \end{aligned}$$

Equation 2.21

The flutter derivatives  $H_i^*$  and  $A_i^*$  depend on the attack angle and reduced frequency  $K$ , which is defined as:

$$K = \frac{B\omega}{U} = \frac{B(2\pi n)}{U}$$

Equation 2.22

where  $B$  is the chord (deck width) (Figure 2.15,  $U$  is the uniform approach velocity of the wind and  $\omega$  is the circular frequency of oscillation ( $n$  is the frequency of oscillation) (Simiu & Scanlan, 1996).

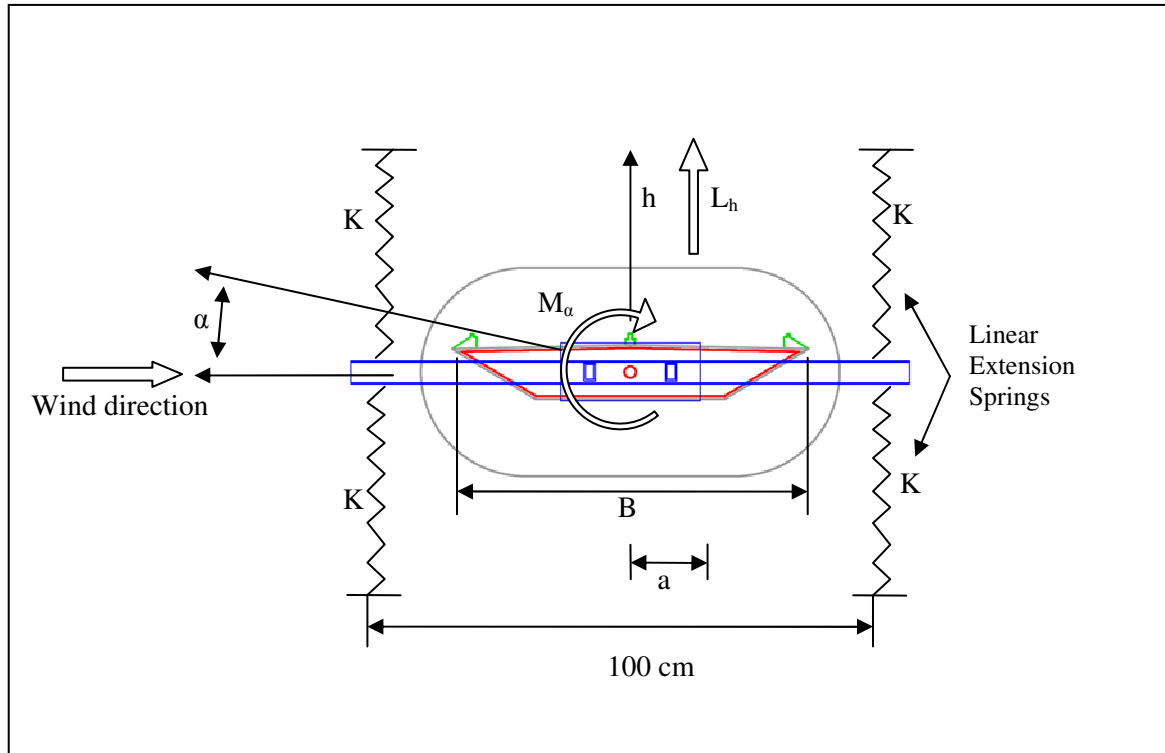


Figure 2.15: 2-DOF bridge deck cross-section view

Among various approaches on identifying flutter derivatives such as:

1. Ibrahim Time Domain
2. Modified Ibrahim Time Domain
3. Covariance Block Hankel Matrix
4. Unifying Least Squares

The Iterative Least Squares (ILS) method has considerable advantage on efficiently identifying the flutter derivatives and is introduced in the following.

## 2.6 ILS-Method

Based on the previous work of Chowdhury and Sarkar (2003) the Iterative Least Squares (ILS) method was used to extract the flutter derivatives from free vibration displacement time-histories from the section model tests in the wind tunnel. Chowdhury and Sarkar (2003) developed the ILS method to work with 3-DOF model, for the present study it was modified for 2-DOF section model test as follows:

$$\underline{\dot{y}} + \underline{M}^{-1}\underline{C}\underline{\dot{y}} + \underline{M}^{-1}\underline{K}\underline{y} = \underline{M}^{-1}\underline{F}_{ae}$$

Equation 2.23

where

$$\underline{y} = \{h \ \alpha\}^T, \quad \underline{M} = \begin{bmatrix} m_h & 0 \\ 0 & I_\alpha \end{bmatrix}, \quad \underline{M}^{-1}\underline{C} = \begin{bmatrix} 2\zeta_h\omega_h & 0 \\ 0 & 2\zeta_\alpha\omega_\alpha \end{bmatrix}, \quad \underline{M}^{-1}\underline{K} = \begin{bmatrix} \omega_h^2 & 0 \\ 0 & \omega_\alpha^2 \end{bmatrix}.$$

The aeroelastic force vector can be written as follows:

$$\begin{Bmatrix} L_h \\ M_\alpha \end{Bmatrix} = \begin{bmatrix} 0.5\rho U^2 B & 0 \\ 0 & 0.5\rho U^2 B^2 \end{bmatrix} \begin{bmatrix} KH_1^*/U & KH_2^*B/U & K^2 H_3^* & K^2 H_4^*/B \\ KA_1^*/U & KA_2^*B/U & K^2 A_3^* & K^2 A_4^*/B \end{bmatrix} \begin{Bmatrix} \dot{h} \\ \dot{\alpha} \\ h \\ \alpha \end{Bmatrix}$$

Equation 2.24

Substituting Equation 2.24 in Equation 2.23 and bringing all terms to the left hand side, aeroelastically modified free-vibration equations of motion are obtained:

$$\underline{\dot{y}} + \underline{C}^{eff}\underline{\dot{y}} + \underline{K}^{eff}\underline{y} = \underline{0}$$

Equation 2.25

where  $\underline{C}^{eff}$  and  $\underline{K}^{eff}$  are the aeroelastically modified effective damping and stiffness matrices, respectively determined from wind tunnel tested at different mean wind velocities. The  $\underline{C}^{mech}$  and

$K^{mech}$  are the mechanical damping and stiffness matrices for zero wind speed, respectively. The flutter derivatives for a 2-DOF section model can be written as (Chowdhury & Sarkar, 2003):

$$\begin{aligned}
 H_1^*(K) &= -\frac{2m_h}{\rho B^2 \omega} (C_{11}^{eff} - C_{11}^{mech}) & A_1^*(K) &= -\frac{2I_\alpha}{\rho B^3 \omega} (C_{21}^{eff} - C_{21}^{mech}) \\
 H_2^*(K) &= -\frac{2m_h}{\rho B^3 \omega} (C_{12}^{eff} - C_{12}^{mech}) & A_2^*(K) &= -\frac{2I_\alpha}{\rho B^4 \omega} (C_{22}^{eff} - C_{22}^{mech}) \\
 H_3^*(K) &= -\frac{2m_h}{\rho B^3 \omega^2} (K_{12}^{eff} - K_{12}^{mech}) & A_3^*(K) &= -\frac{2I_\alpha}{\rho B^4 \omega^2} (K_{22}^{eff} - K_{22}^{mech}) \\
 H_4^*(K) &= -\frac{2m_h}{\rho B^2 \omega^2} (K_{11}^{eff} - K_{11}^{mech}) & A_4^*(K) &= -\frac{2I_\alpha}{\rho B^3 \omega^2} (K_{21}^{eff} - K_{21}^{mech})
 \end{aligned}$$

Equation 2.26

where  $K = B\omega/U$  in the non-dimensional reduced frequency;  $U$  is the mean wind velocity;  $\omega$  is the circular frequency of oscillation,  $m_h$  and  $I_\alpha$  are mass and mass moment of inertia of the model, per unit length.

In implementing the ILS method Equation 2.25 can be written in state-space model as:

$$\dot{\underline{X}} = \underline{A}\underline{X}$$

Equation 2.27

where  $\underline{X} = \begin{Bmatrix} \underline{y} \\ \underline{\dot{y}} \end{Bmatrix}$ ,  $\underline{A} = \begin{bmatrix} 0 & I \\ -\underline{K}^{eff} & -\underline{C}^{eff} \end{bmatrix}$ .

The  $A$  matrix is  $2n \times 2n$  square matrix, where  $n$  is the number of degree of freedom for the dynamic system;  $I$  is the identity matrix of size  $n \times n$ . The  $A$  matrix can be identified if acceleration, velocity and displacement data can be recorded for all  $n$  degree of freedom for at least  $2n$  different instants of time (Chowdhury & Sarkar, 2003). The present experimental setup used would not allow for this and in most practical applications it is un-reasonable. The

alternative approach utilizes noisy acceleration time-histories, which are then filtered using zero-phase digital filtering (MATLAB low-pass digital Butterworth filter). The filter data could then be used to generate velocity and displacement time-histories by taking the derivative of the acceleration data. Before continuing the data needed to be further manipulated due to initial noise upon release of the section model and inherent error in using the MATLAB Butterworth Filter, the beginning and end of the displacement, velocity and acceleration time-histories were cropped to reduce error. The new cropped section of each time-history was used to extract the elements of the  $A$  matrix by the ILS method. A computer code created in MATLAB was utilized to identify the parameters of the  $A$  matrix, which is summarized in the following algorithm:

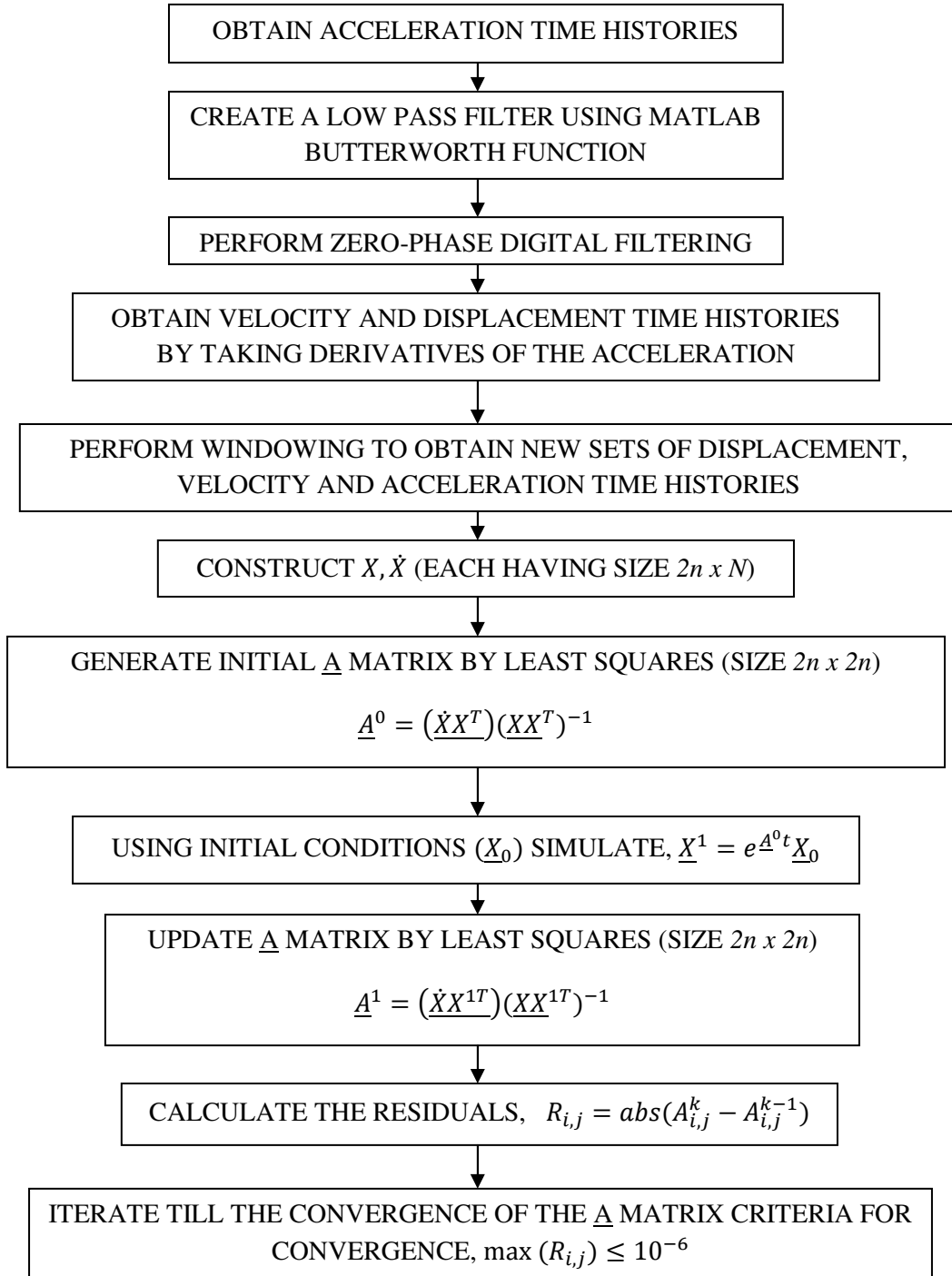


Figure 2.16: Iterative Least Squares, similar to (Chowdhury & Sarkar, 2003)

## CHAPTER 3 WIND TUNNEL TEST RESULTS

### 3.1 Calibration Tests without Vehicles

Before extensive tests were conducted to identify the wind flutter derivative coefficients, a series of calibration tests were conducted for the bridge section model without vehicles. The calibration process was basically to compare the flutter derivative results from single-degree-of-freedom (SDOF) tests of vertical and torsional only and the results from coupled multi-degree-of-freedom (MDOF) testing. Generally, the SDOF testing will derive a number of flutter coefficients which are located on the diagonal terms of the coupled aerodynamic matrix. The MDOF tests will derive all the flutter derivatives including both diagonal terms and also some off-diagonal terms (coupling-related coefficients). By comparing the diagonal coefficients from both SDOF and MDOF, the accuracy of the MDOF tests can be verified. As discussed earlier, in order to avoid random errors from the testing and measurements, for each testing scenario, the test was repeated three times.

Figure 3.1 gives the three repeated testing results of  $H1^*$  from “Pure vertical” (SDOF) and “Coupled vertical” (MDOF), respectively. It can be seen from the figures that the testing results from SDOF and MDOF of the three different tests are very similar, showing good consistency of the testing results. Fig. 3.2 shows the averaged results from three repeated tests for “Pure Vertical Motion” and “Coupled Motion”, respectively. Very good agreements can be found between the average results between SDOF and MDOF results.

Similarly, the results of  $H4^*$ ,  $A2^*$  and  $A3^*$  are shown in Figs. 3.3-4, Figs. 3.5-6, Figs. 3.7-8, respectively. As compared to the results related to vertical ( $H1^*$  and  $H4^*$ ), it was found that the

calibration results for torsion related coefficients ( $A2^*$  and  $A3^*$ ) had relatively larger errors when wind speeds increased.

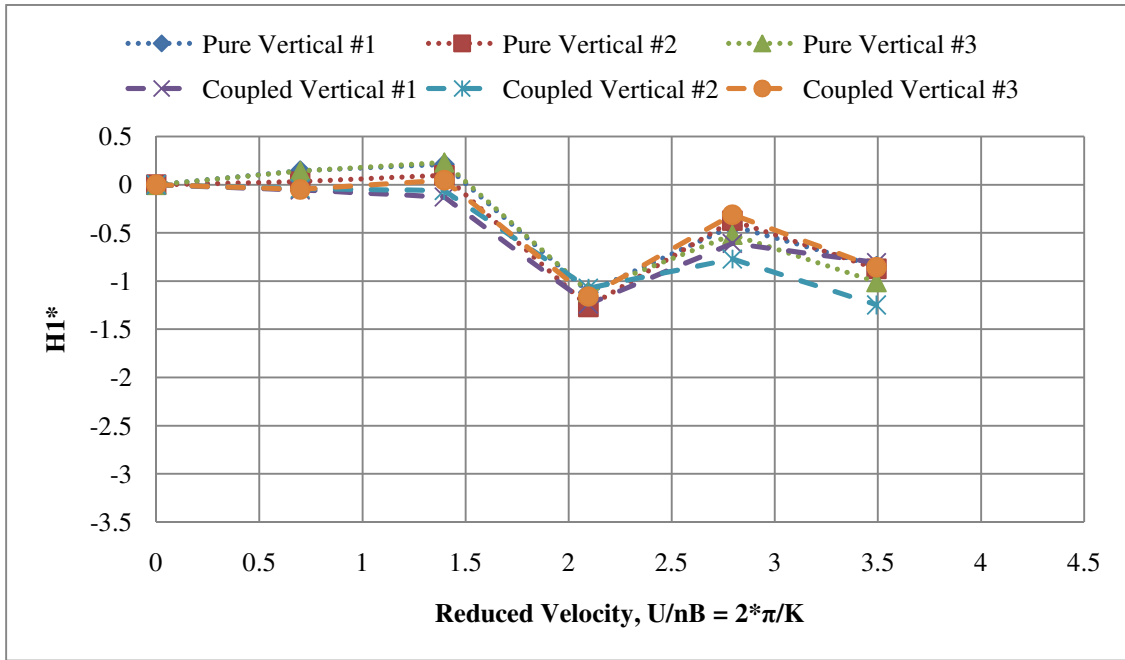


Figure 3.1: Three calibration tests of pure vertical and coupled flutter analysis of  $H1^*$

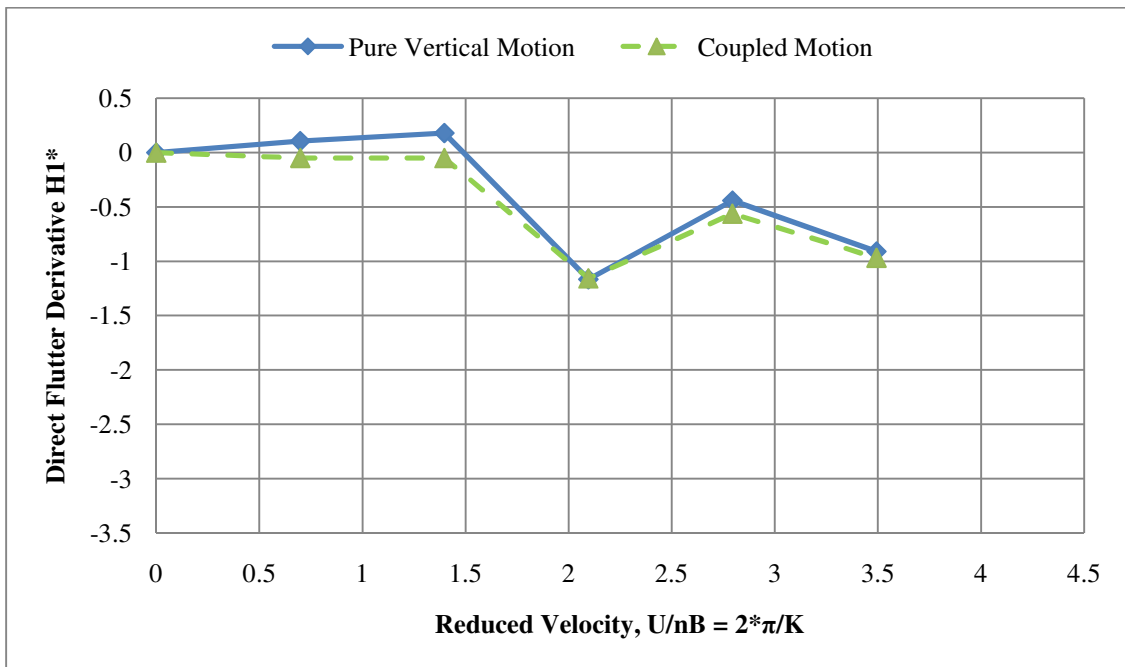


Figure 3.2: The average results of pure vertical and coupled flutter analysis of  $H1^*$

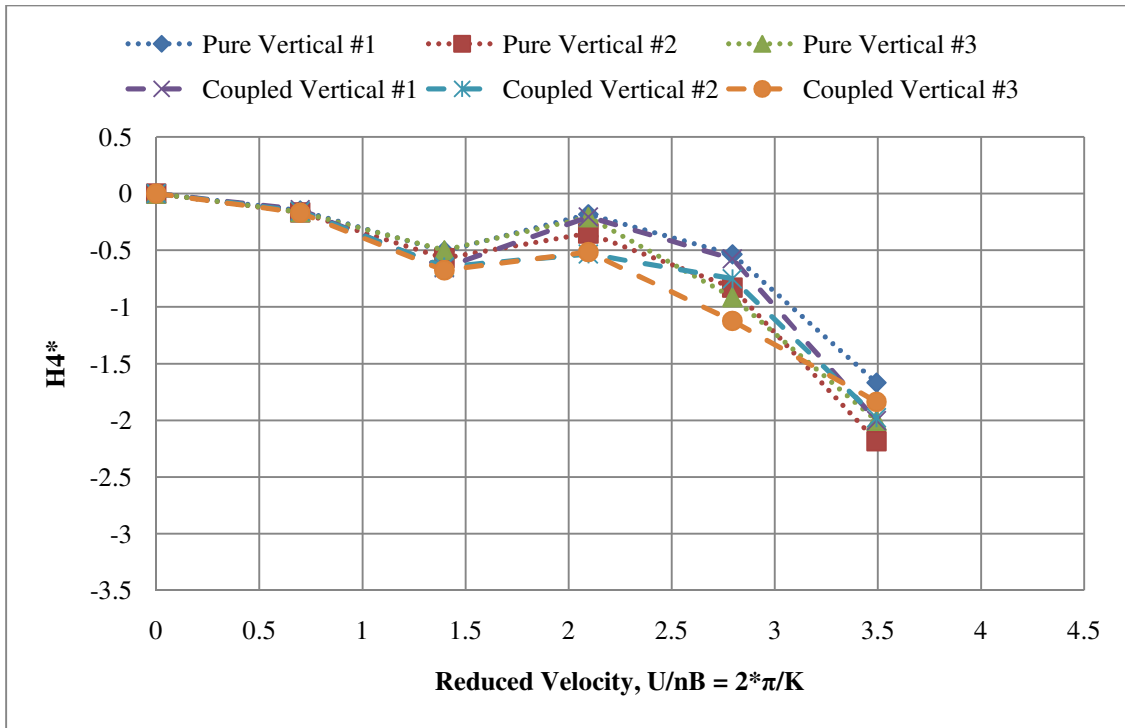


Figure 3.3: Three tests of pure vertical and coupled flutter analysis of  $H4^*$

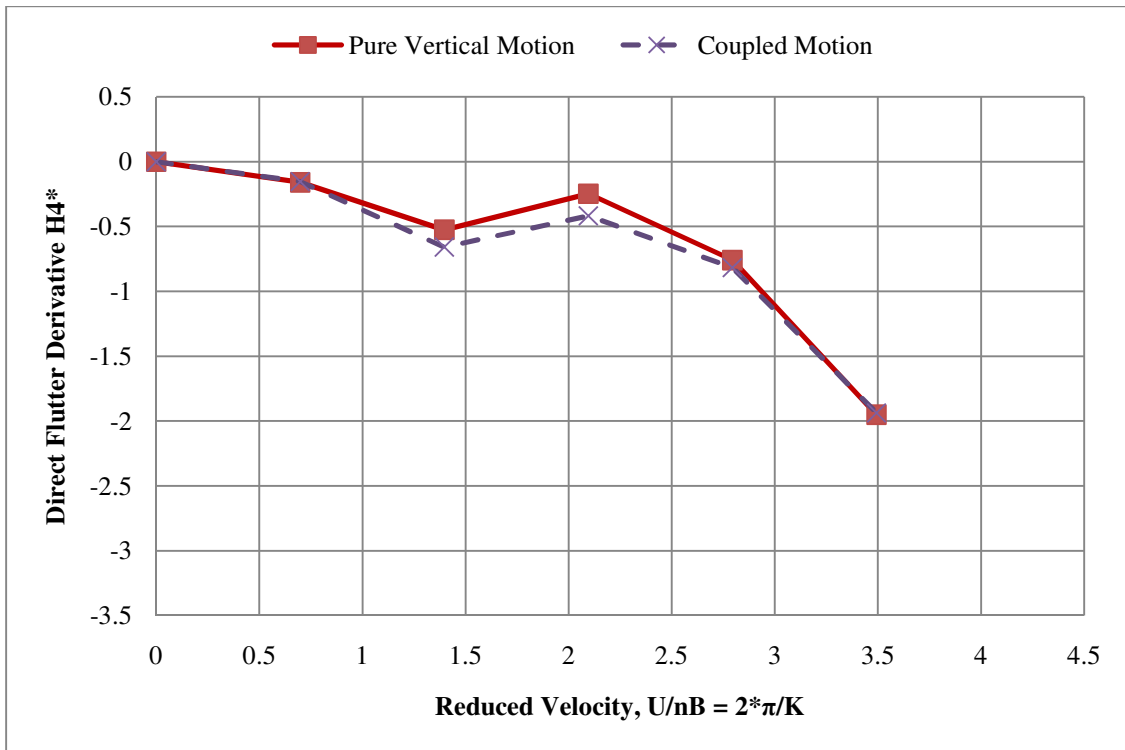


Figure 3.4: The average results of pure vertical and coupled flutter analysis of  $H4^*$

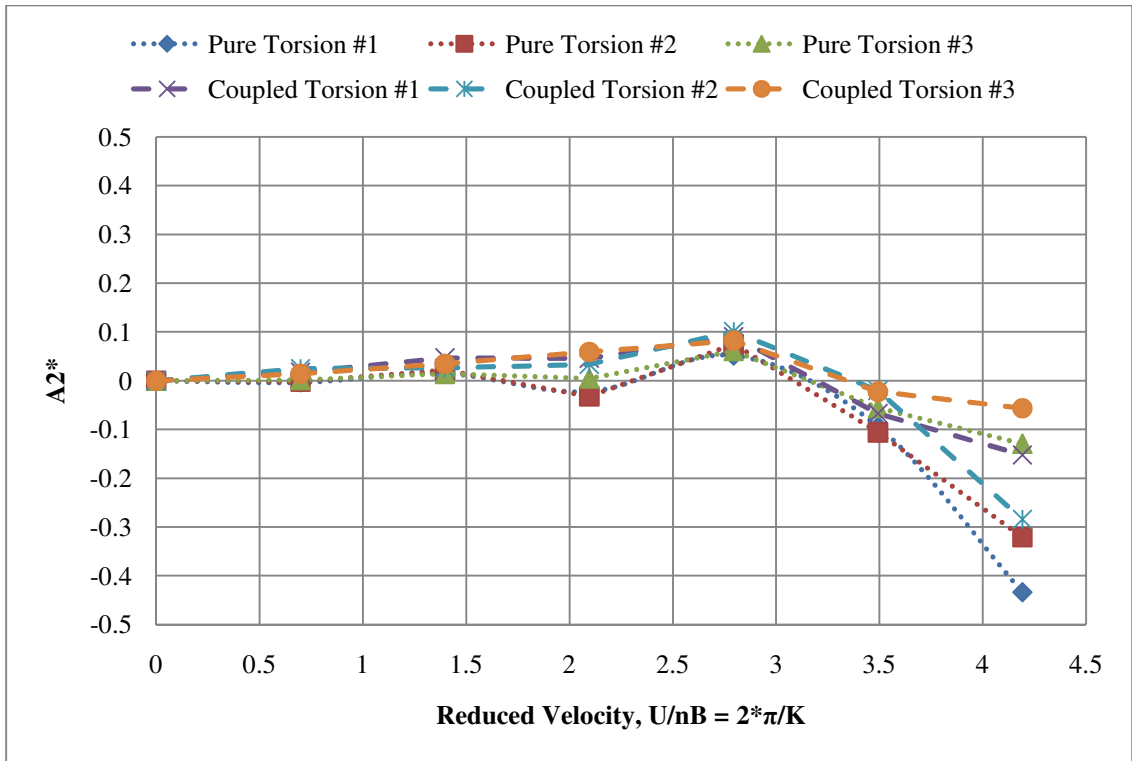


Figure 3.5: Three tests of pure torsional and coupled flutter analysis of  $A2^*$

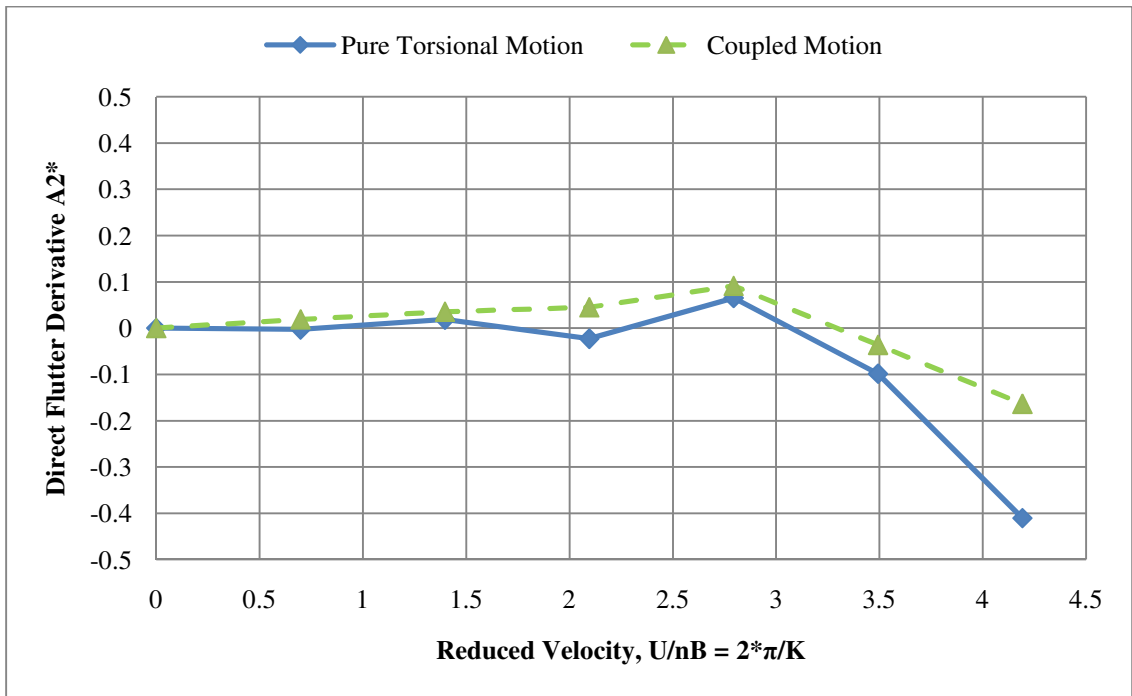


Figure 3.6: The average results of pure torsional and coupled flutter analysis of  $A2^*$

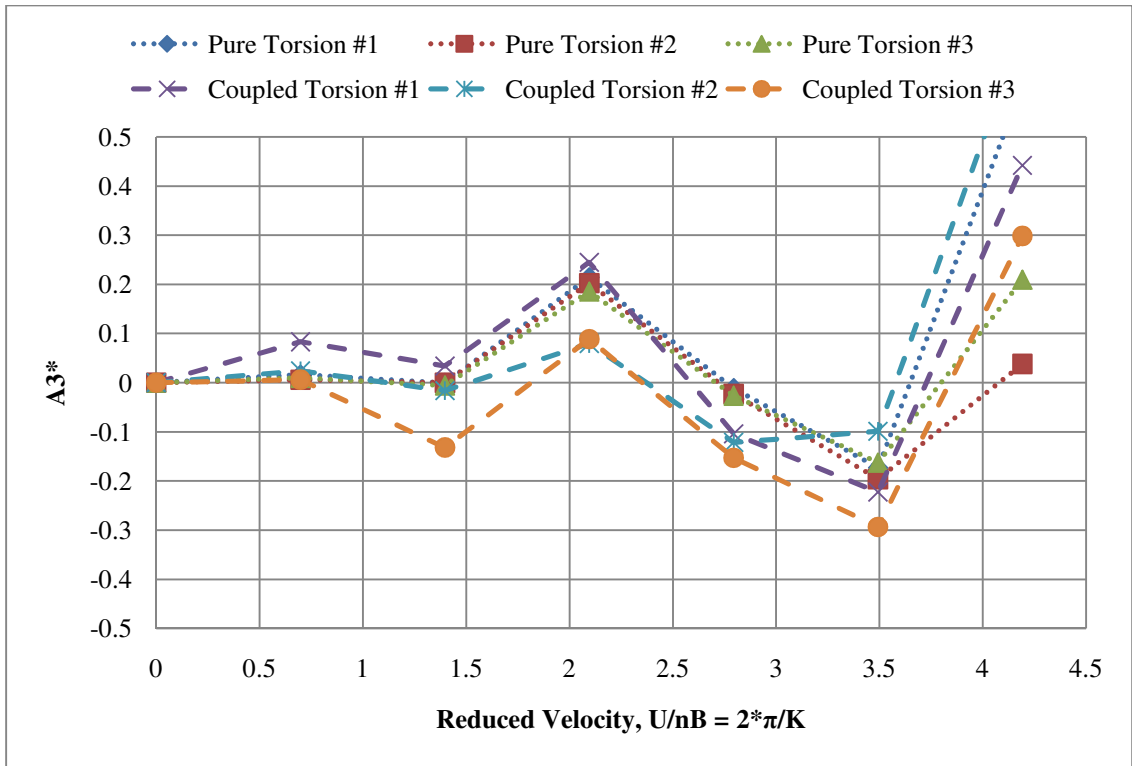


Figure 3.7: Three tests of pure torsional and coupled flutter analysis of  $A3^*$

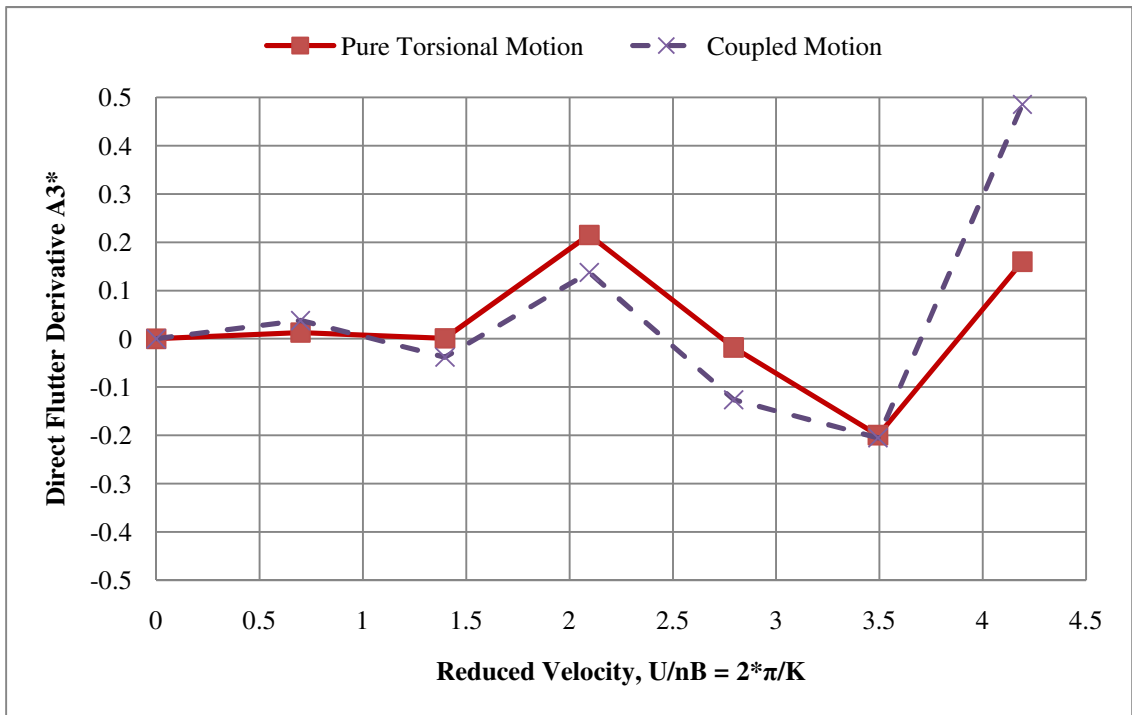


Figure 3.8: The average results of pure torsional and coupled flutter analysis of  $A3^*$

The calibration results were also examined statistically to give some quantitative results between the SDOF and MDOF analysis results. The Tables 3.1-2 show the mean, standard deviation and coefficient of variation for the direct flutter derivatives in the SDOF analysis. Tables 3.3-6 represent the statistical results of all the flutter derivatives from the MDOF analysis. The statistical results were carefully examined as the flutter derivatives were very small numbers which may easily cause inherent statistical difficulties. The tables show very small means (close to zero) that can result in the large coefficient of variation value. As expected, the standard deviations increase with wind velocity, but stayed reasonably small and consistent between the SDOF and MDOF analysis.

**Table 3.1: SDOF statistical results for A2\* and A3\***

U/nB = 2*pi/K	A2*			A3*		
	$\sigma$	mean	CoV	$\sigma$	mean	CoV
0.699	0.003	-0.001	-1.928	0.005	0.011	0.489
1.397	0.004	0.017	0.251	0.003	-0.002	-1.387
2.096	0.019	-0.017	-1.153	0.014	0.201	0.072
2.794	0.012	0.062	0.185	0.008	-0.020	-0.385
3.493	0.026	-0.086	-0.305	0.017	-0.177	-0.096
4.191	0.154	-0.295	-0.522	0.291	0.284	1.023

**Table 3.2: SDOF statistical results for H1\* and H4\***

U/nB = 2*pi/K	H1*			H4*		
	$\sigma$	mean	CoV	$\sigma$	mean	CoV
0.699	0.064	0.106	0.607	0.009	-0.160	-0.056
1.397	0.071	0.180	0.396	0.038	-0.525	-0.073
2.096	0.089	-1.165	-0.076	0.091	-0.247	-0.367
2.794	0.073	-0.441	-0.165	0.198	-0.759	-0.261
3.493	0.088	-0.909	-0.097	0.262	-1.951	-0.134

**Table 3.3: MDOF statistical results for A1\* and A2\***

	A1*			A2*		
U/nB = 2*pi/K	$\sigma$	mean	CoV	$\sigma$	mean	CoV
0.699	0.035	0.036	0.968	0.005	0.019	0.288
1.397	0.088	-0.007	-12.912	0.010	0.036	0.291
2.096	0.083	-0.096	-0.866	0.013	0.046	0.281
2.794	0.097	-0.249	-0.390	0.009	0.091	0.103
3.493	0.164	-0.255	-0.641	0.027	-0.037	-0.722
4.191	0.195	-0.170	-1.151	0.114	-0.165	-0.695

**Table 3.4: MDOF statistical results for A3\* and A4\***

	A3*			A4*		
U/nB = 2*pi/K	$\sigma$	mean	CoV	$\sigma$	mean	CoV
0.699	0.040	0.038	1.063	0.026	0.010	2.599
1.397	0.085	-0.038	-2.242	0.105	-0.024	-4.365
2.096	0.093	0.137	0.676	0.201	-0.105	-1.908
2.794	0.025	-0.126	-0.196	0.011	-0.154	-0.073
3.493	0.099	-0.205	-0.481	0.192	-0.165	-1.160
4.191	0.212	0.485	0.437	0.150	-0.207	-0.726

**Table 3.5: MDOF statistical results for H1\* and H2\***

	H1*			H2*		
U/nB = 2*pi/K	$\sigma$	mean	CoV	$\sigma$	mean	CoV
0.699	0.007	-0.048	-0.148	0.002	-0.011	-0.203
1.397	0.087	-0.047	-1.859	0.013	-0.005	-2.753
2.096	0.083	-1.157	-0.072	0.039	0.022	1.792
2.794	0.233	-0.564	-0.413	0.006	-0.006	-0.984
3.493	0.241	-0.971	-0.249	0.068	0.038	1.802
4.191	0.609	-1.467	-0.415	0.102	-0.023	-4.532

**Table 3.6: MDOF statistical results for H3\* and H4\***

U/nB = 2*pi/K	H3*			H4*		
	$\sigma$	mean	CoV	$\sigma$	mean	CoV
0.699	0.006	-0.006	-0.981	0.014	-0.154	-0.093
1.397	0.001	0.039	0.036	0.016	-0.658	-0.024
2.096	0.024	0.007	3.459	0.184	-0.418	-0.440
2.794	0.037	0.060	0.617	0.280	-0.817	-0.343
3.493	0.047	0.099	0.477	0.089	-1.938	-0.046
4.191	0.463	0.424	1.093	0.502	-2.634	-0.191

## 3.2 Spatial Dependent Traffic Test Results

### 3.2.1 Spatial Cases 2.1-2.3 with Traffic Density of 20 vehicles/km/ln

The spatial dependent traffic scenarios originally consisted of five different traffic volumes along the main span of the bridge listed below.

1. Traffic Density of 10 vehicles/km/ln
2. Traffic Density of 20 vehicles/km/ln
3. Traffic Density of 32 vehicles/km/ln
4. Bumper to bumper both sides
5. Bumper to bumper windward or leeward

The fourth and fifth scenarios were not tested as they were similar to the extreme traffic cases, which will be discussed separately in Section 3.4. The first scenario was eliminated due to time constraints in the wind tunnel and the fact that most of the simulations only had one or two vehicles on the road which was assumed to be of less significance as compared to higher traffic densities.

According to the scaling rule, it is known that the bridge section model represent a bridge deck segment 62m in length. In order to investigate the impacts on the flutter derivatives from

spatially distributed traffic on the bridge deck, three “snapshots” of the vehicle distribution on the three continuous segments in the middle of the main span are made. These “snapshots” were obtained from the traffic flow simulations and the vehicle distribution results for each “snapshot” are shown in Fig. 3.9 and are referred to “Case 2.1-2.3” from left to right when the traffic density equals 20 vehicles/km/ln. Additional vehicle model descriptions can be found in Table 2.3, Chapter 2. Under each “snapshot”, flutter derivatives are identified and compared with those without vehicles.

The results are shown in Figs. 3.10-13 for  $A1^*$ - $A4^*$  and in Figs.3.14-17 for  $H1^*$ - $H4^*$ , respectively when the traffic density equals to 20 vehicles/km/ln. The observations of these flutter derivatives are discussed in the following:

$A1^*$ : Generally increases with the presence of vehicles as compared to the results without any vehicles. The impact from the spatial dependent traffic gets stronger with the increase of wind speed. For example, when the reduced velocity is about 2.79, the average difference is about 100% when compared to the bridge section without vehicles. In Fig. 3.10 the  $A1^*$  derivative was originally negative and became positive after the traffic was added in all cases. It is significant that the sign of the derivative changed with each case, however one must consider this is only three snapshots of the spatial traffic flow and the full dynamic effect of actual traffic flow is not necessarily fully represented.

$A2^*$ : With the presence of traffic,  $A2^*$  varies in a complex pattern: decreased first and then slightly increased when the wind speed was high. It is known that  $A2^*$  is related to the aerodynamic damping of torsion, which is very critical to flutter stability. The complex nature of the variation of  $A2^*$  with traffic shows that a general conclusion in terms of impact of traffic on flutter stability cannot be easily made. However, the change from negative value to close to zero in higher wind speeds suggest that there is possibility that the bridge becomes vulnerable to

flutter with the presence of traffic. More specific conclusion can only be made after an actual flutter analysis with all the flutter derivatives is made.

$A3^*$ : When wind speed is low, different cases have similar  $A3^*$  values. With the increase of wind speed, the spatial difference of traffic causes considerably different  $A3^*$  values. Since  $A3^*$  is related to the aerodynamic stiffness, the impacts to the flutter stability or buffeting response from  $A3^*$  are usually limited.

$A4^*$ : Similar to  $A1^*$  and  $A3^*$ , the spatial difference of traffic caused different  $A4^*$  values when the wind speed gets higher. With the presence of traffic,  $A4^*$  gradually increased from negative to positive when the wind speed increases.  $A1^*$  and  $A4^*$  are the coupled damping and stiffness terms, respectively. More significant variations of  $A1^*$  and  $A4^*$  from without traffic to with traffic in higher wind speeds show that the coupling effects between the vertical and torsion modes may become stronger because of the presence of traffic. In order to quantify the coupling effects and the impacts on flutter stability and buffeting response, a more comprehensive analysis has to be made.

$H1^*$ : Similar to  $A2^*$ , the presence of traffic has increasing impact on the values of  $H1^*$  when wind becomes stronger. The different spatial distributions of traffic will cause different  $H1^*$  values only when wind speed increases. When wind speed gets higher,  $H1^*$  further decrease as a negative value. Since  $H1^*$  is related to the damping terms of vertical motion, the decrease of  $H1^*$  in negative means the increase of aerodynamic damping of vertical motion as compared to without traffic. The resultant effect to typical coupled flutter is not clear, along with the changes of  $A2$  and other coefficients.

$H2^*$  &  $H3^*$ : There is nearly no considerable difference on  $H2^*$  and  $H3^*$  between the cases with traffic and without traffic. All the values are close to zero.

H4\*: It can be observed that the different cases (i.e. traffic distributions) have some impacts on H4\* values only when wind speed gets higher. Similar to A3\*, H4\* is related to the aerodynamic stiffness (about vertical motion).

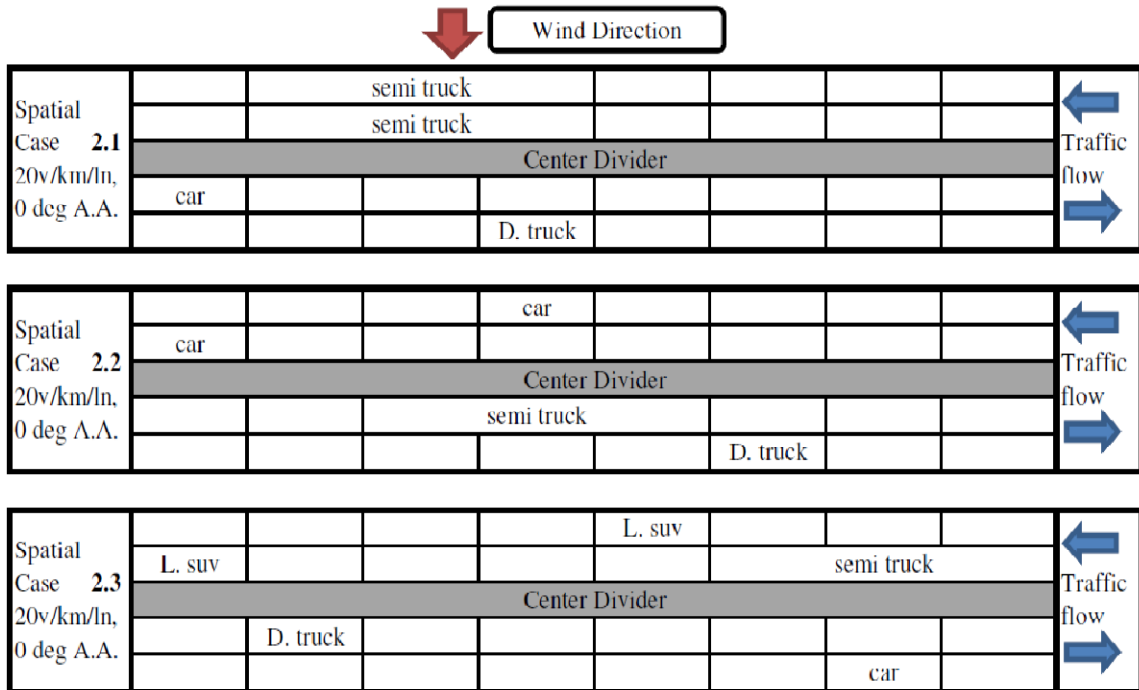


Figure 3.9: Spatial dependent vehicle positioning for cases 2.1-2.3 with 20 vehicles/km/lane

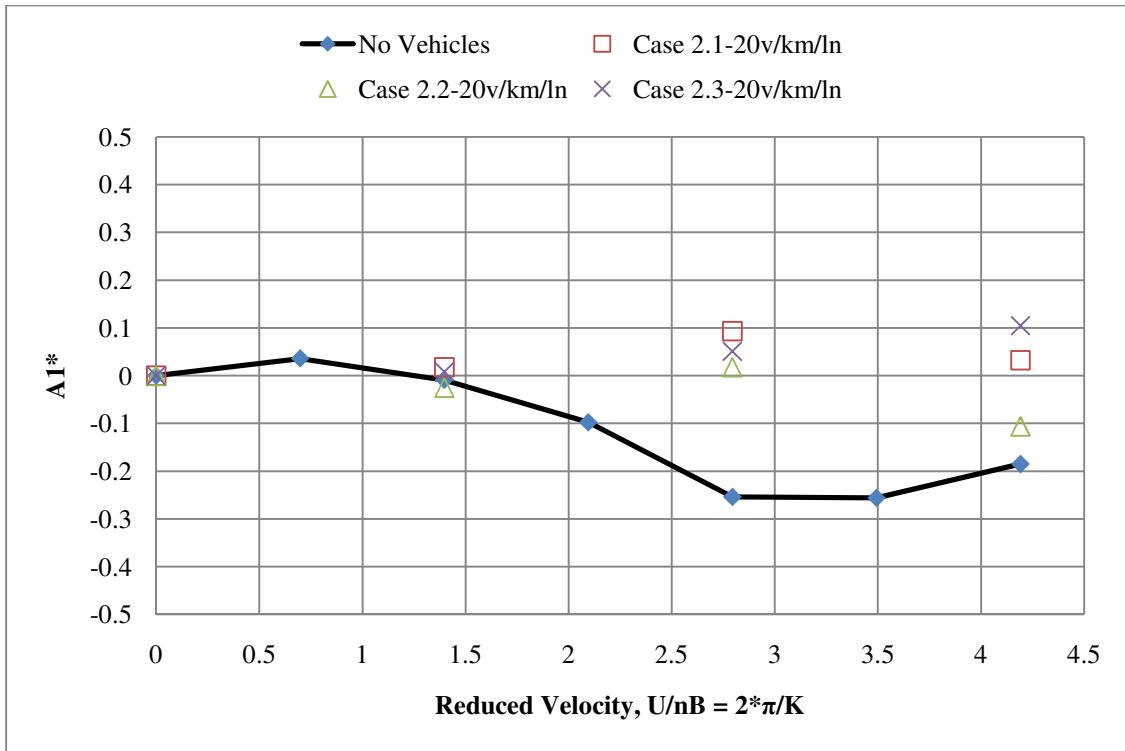


Figure 3.10: Flutter derivative  $A1^*$  for Spatial Cases 2.1-2.3

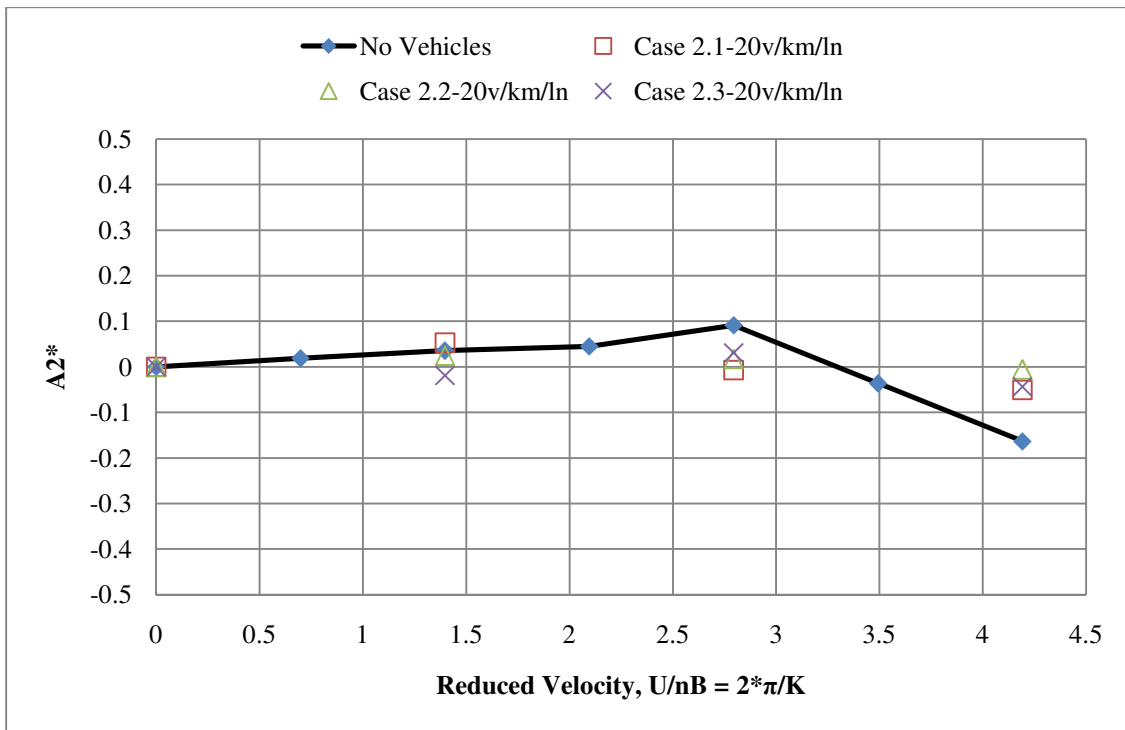


Figure 3.11: Flutter derivative  $A2^*$  for Spatial Cases 2.1-2.3

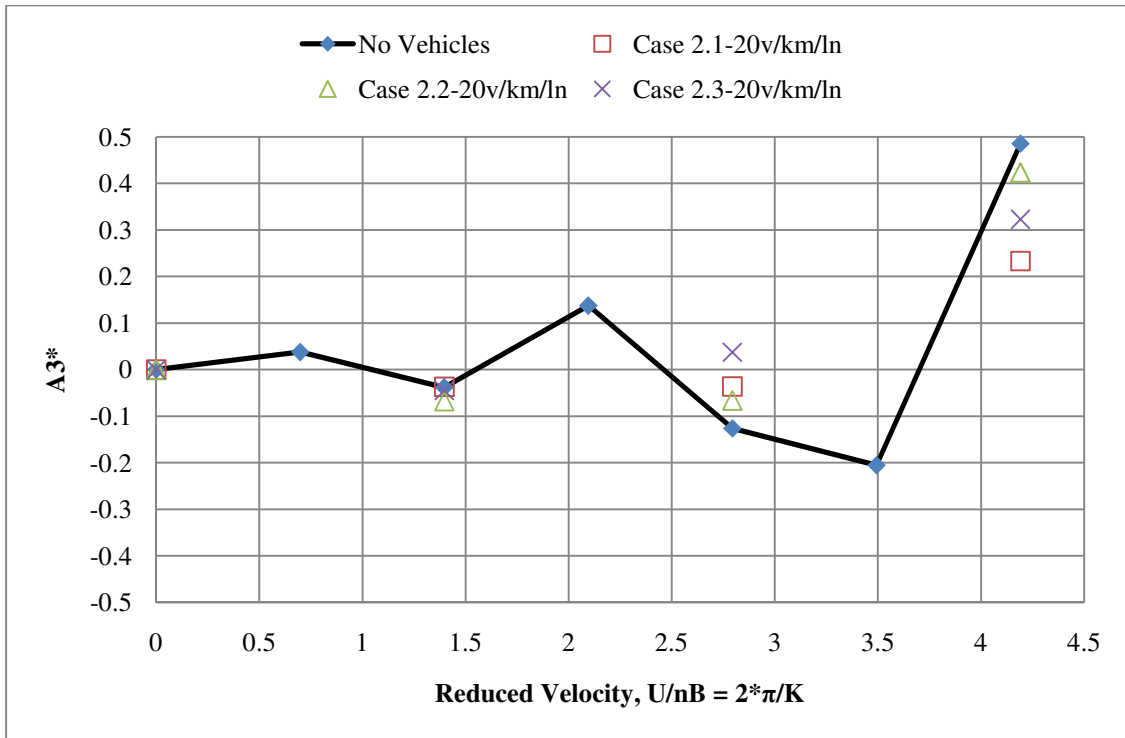


Figure 3.12: Flutter derivative  $A3^*$  for Spatial Cases 2.1-2.3

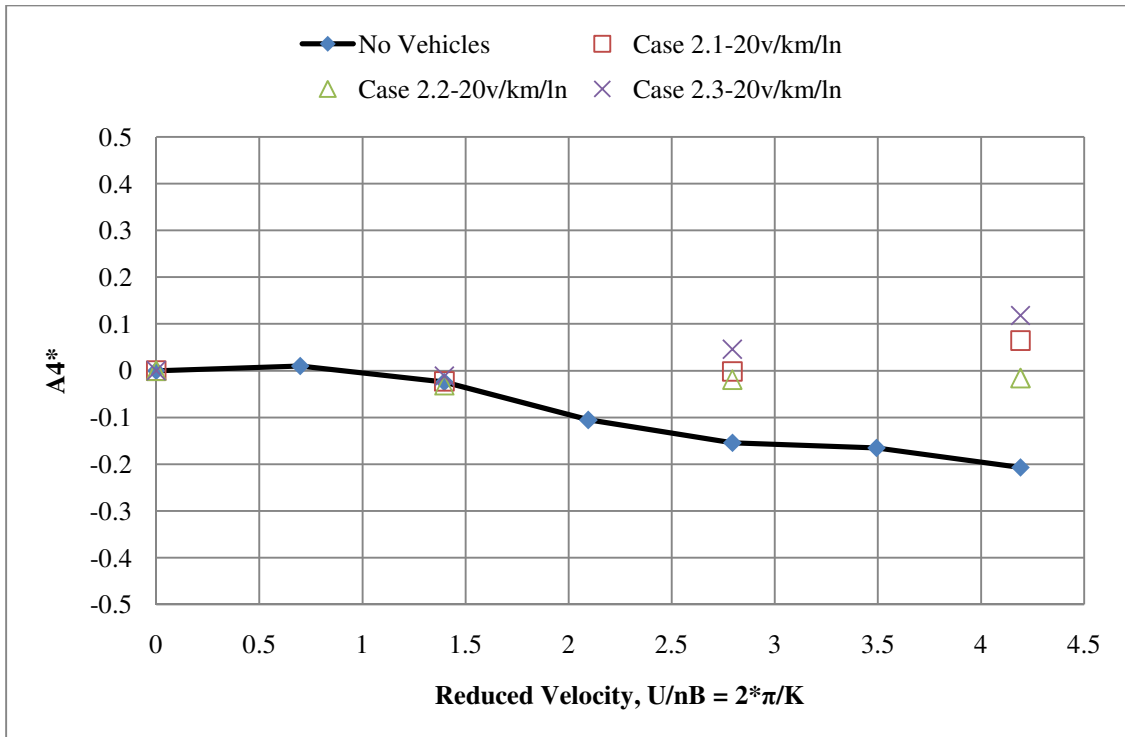


Figure 3.13: Flutter derivative  $A4^*$  for Spatial Cases 2.1-2.3

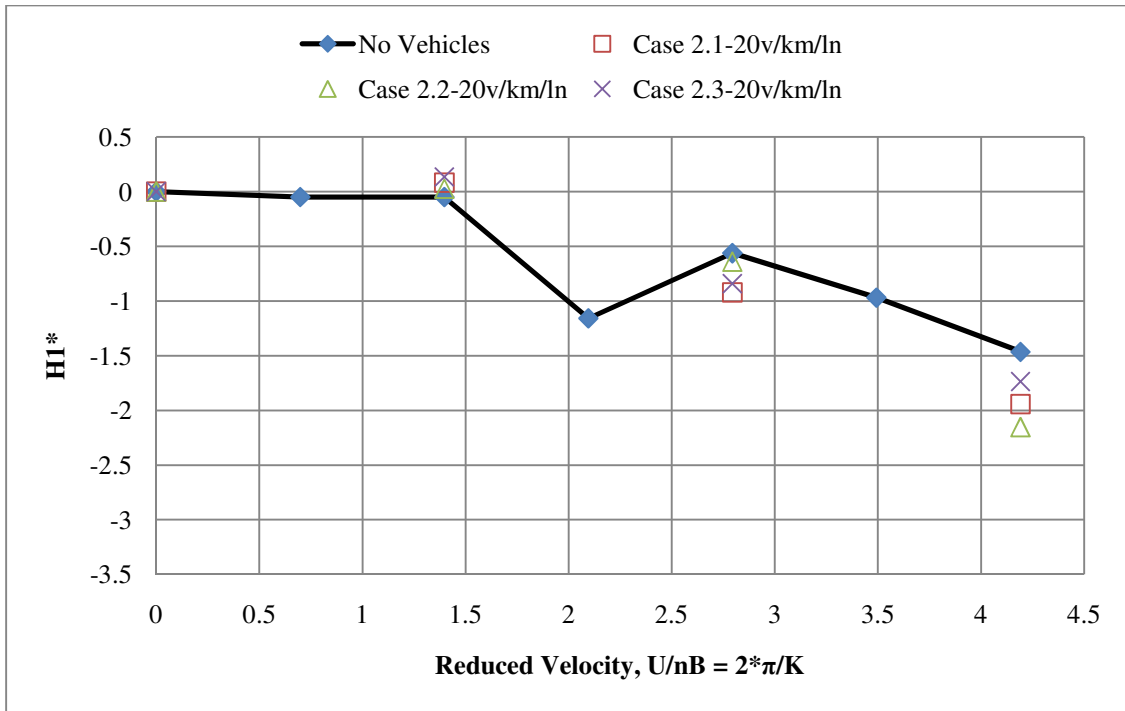


Figure 3.14: Flutter derivative  $H1^*$  for Spatial Cases 2.1-2.3

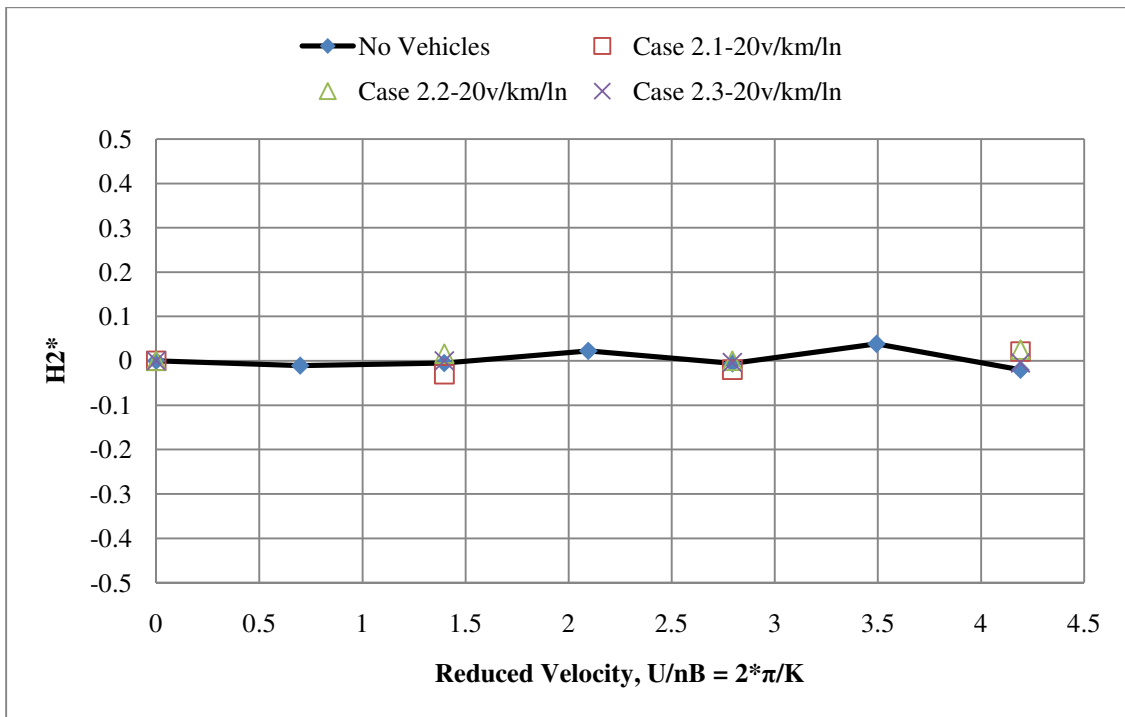


Figure 3.15: Flutter derivative  $H2^*$  for Spatial Cases 2.1-2.3

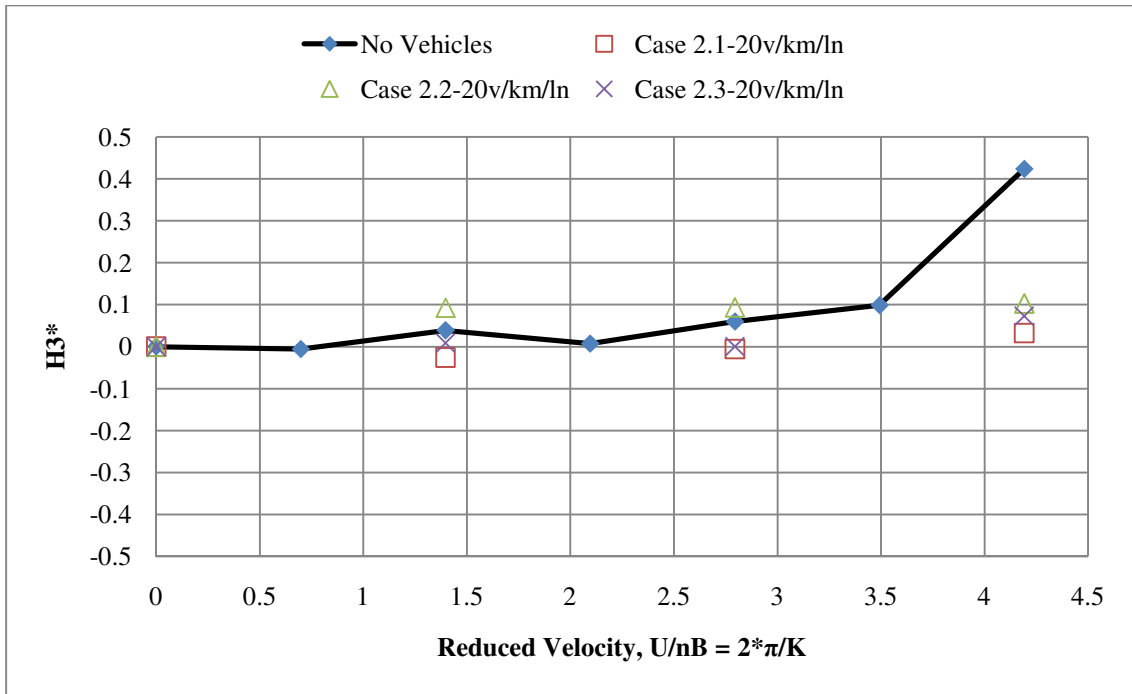


Figure 3.16: Flutter derivative  $H3^*$  for Spatial Cases 2.1-2.3

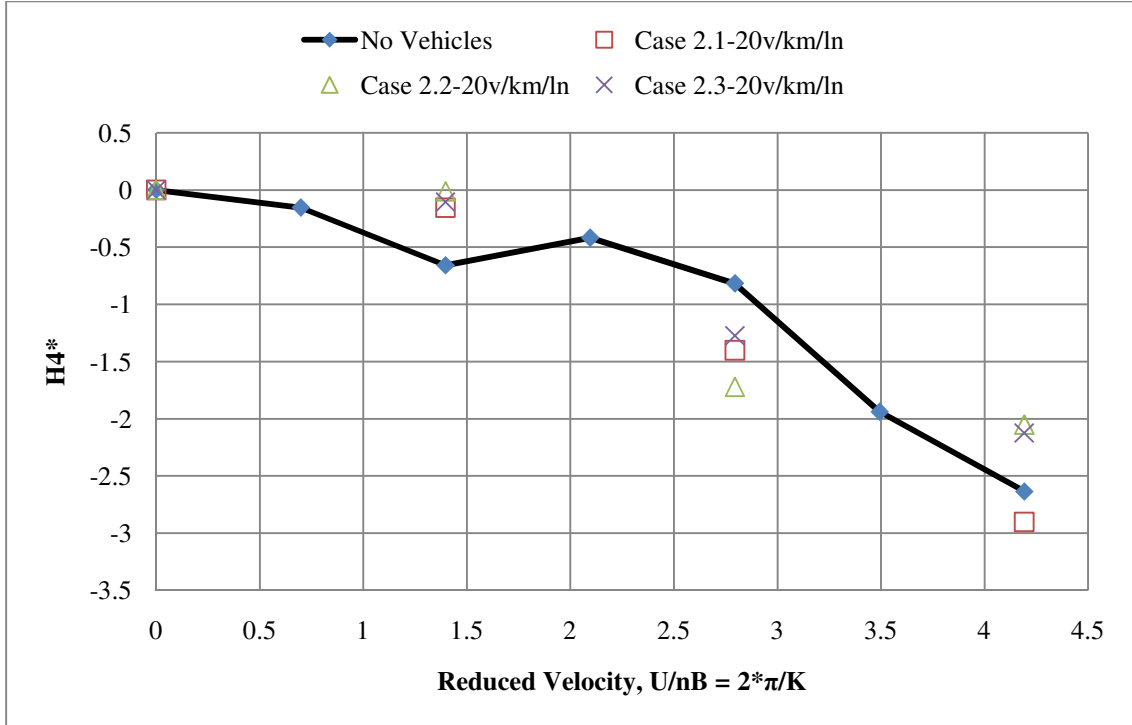


Figure 3.17: Flutter derivative  $H4^*$  for Spatial Cases 2.1-2.3

### 3.2.2 Spatial Cases 3.1-3.3 with Traffic Density of 32 vehicles/km/ln

In Figure 3.18, the vehicle distributions on the bridge deck are shown for spatial cases 3.1-3.3 with a traffic density of 32 vehicles/km/ln. Each case represents a different spatial segment of the simulated traffic flow on the bridge.

The wind coefficients of A1-4\* and H1-4\* are shown in Figs. 3.19-22 and 3.23-26, respectively. The comparisons between the results in Figs. 3.19-26 and Figs. 3.10-17 were made. It is found that busier spatial traffic (32 veh/km/ln vs. 20 veh/km/ln) did not cause considerable difference on the flutter derivatives. However, the 32 veh/km/ln did exhibit a strong vortex shedding at a reduced velocity of 1.39, which was not observed in the 20 veh/km/ln cases.

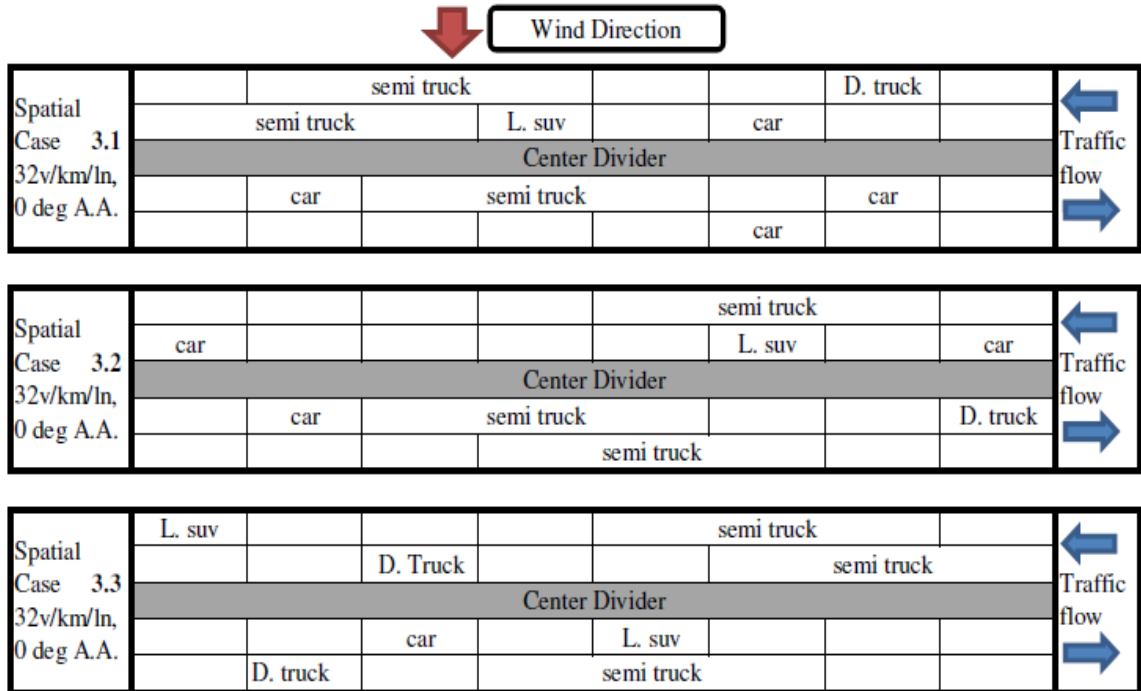


Figure 3.18: Spatial dependent vehicle positioning for cases 3.1-3.3 with 32 vehicles/km/lane

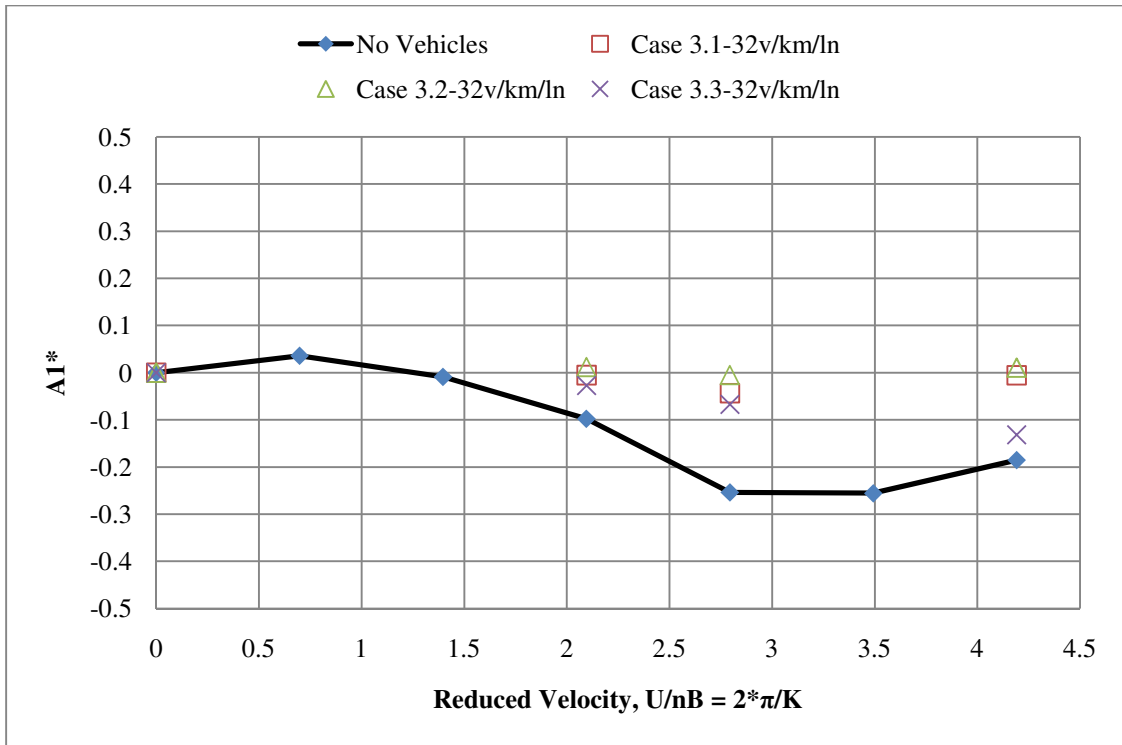


Figure 3.19: Flutter derivative  $A1^*$  for Spatial Cases 3.1-3.3

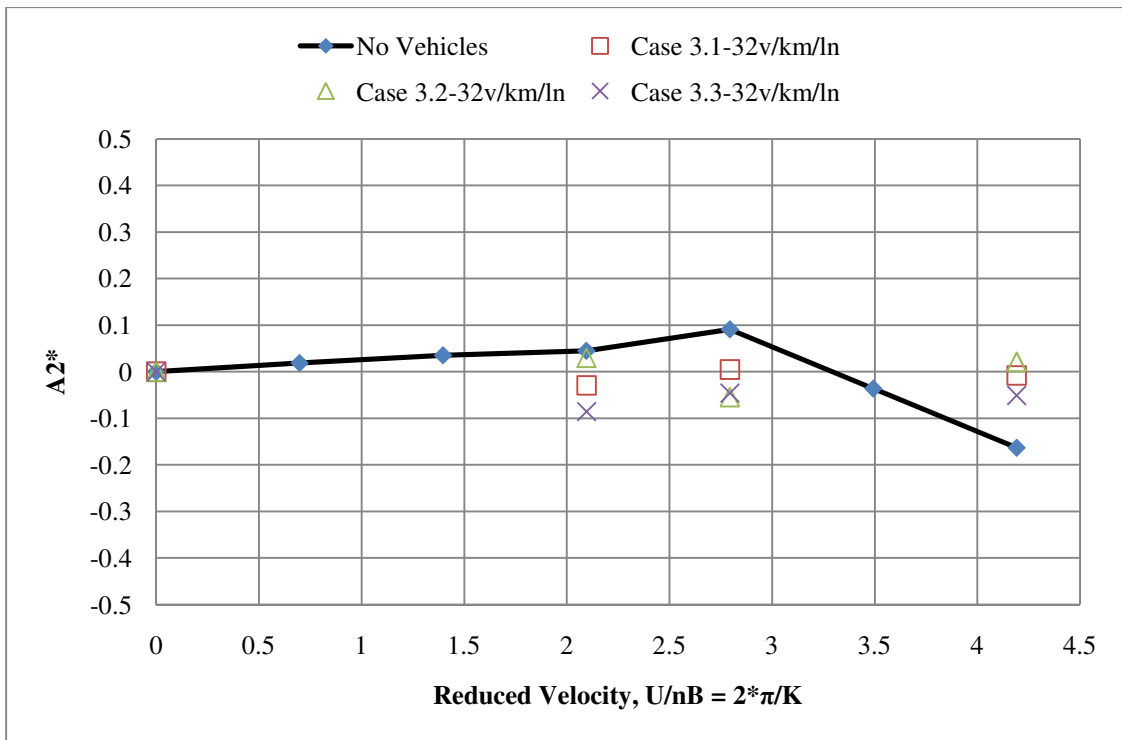


Figure 3.20: Flutter derivative  $A2^*$  for Spatial Cases 3.1-3.3

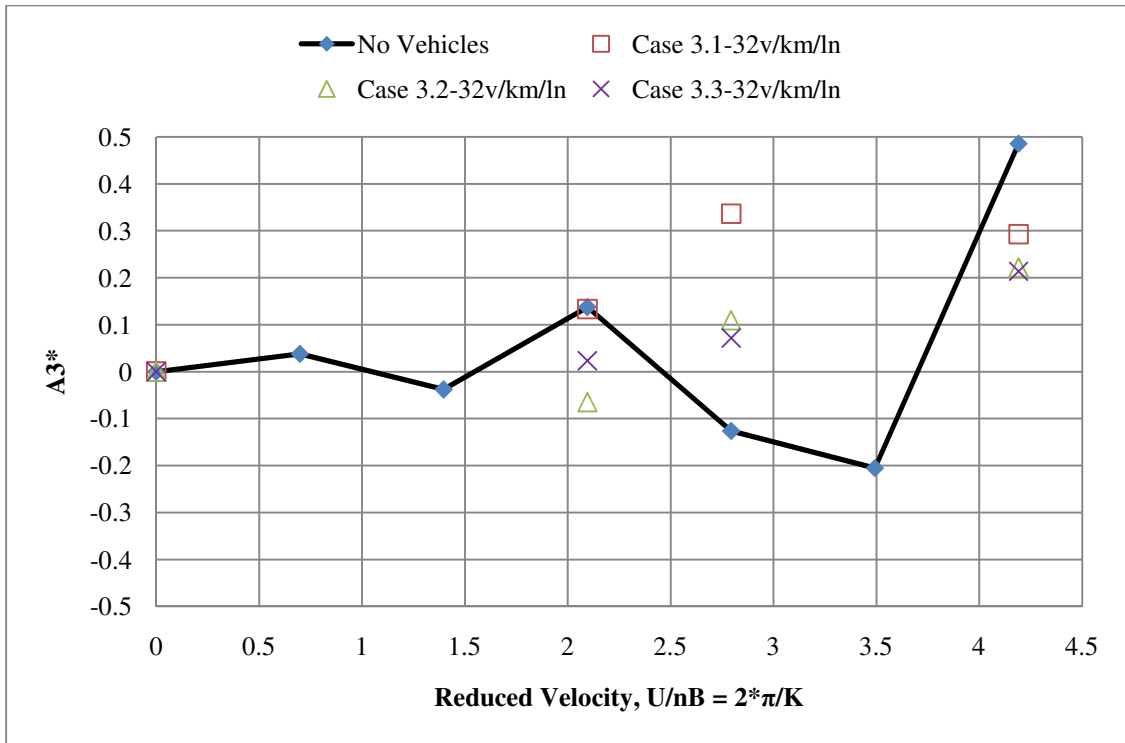


Figure 3.21: Flutter derivative  $A3^*$  for Spatial Cases 3.1-3.3

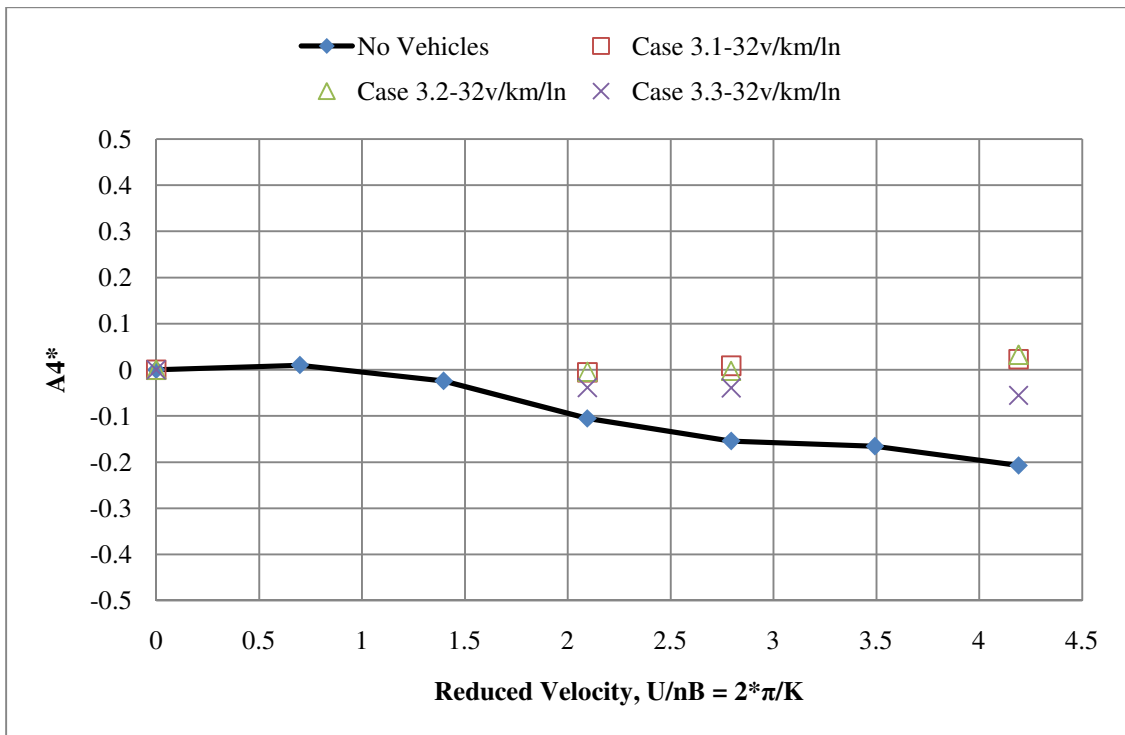


Figure 3.22: Flutter derivative  $A4^*$  for Spatial Cases 3.1-3.3

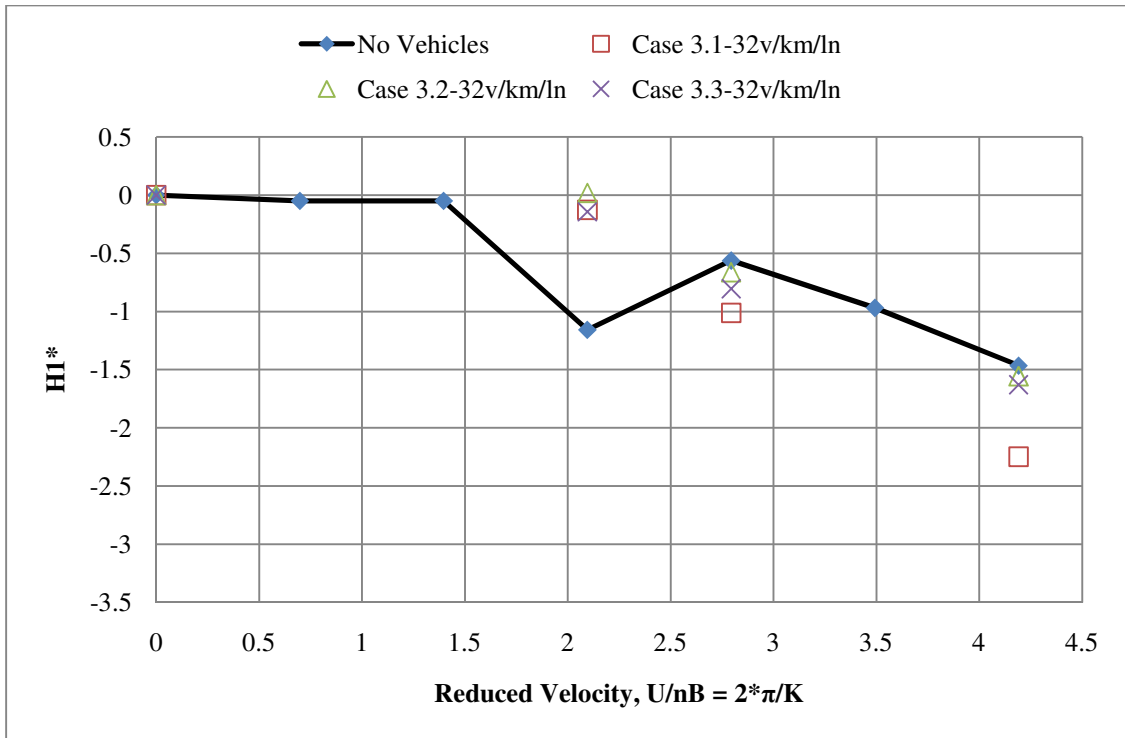


Figure 3.23: Flutter derivative  $H1^*$  for Spatial Cases 3.1-3.3

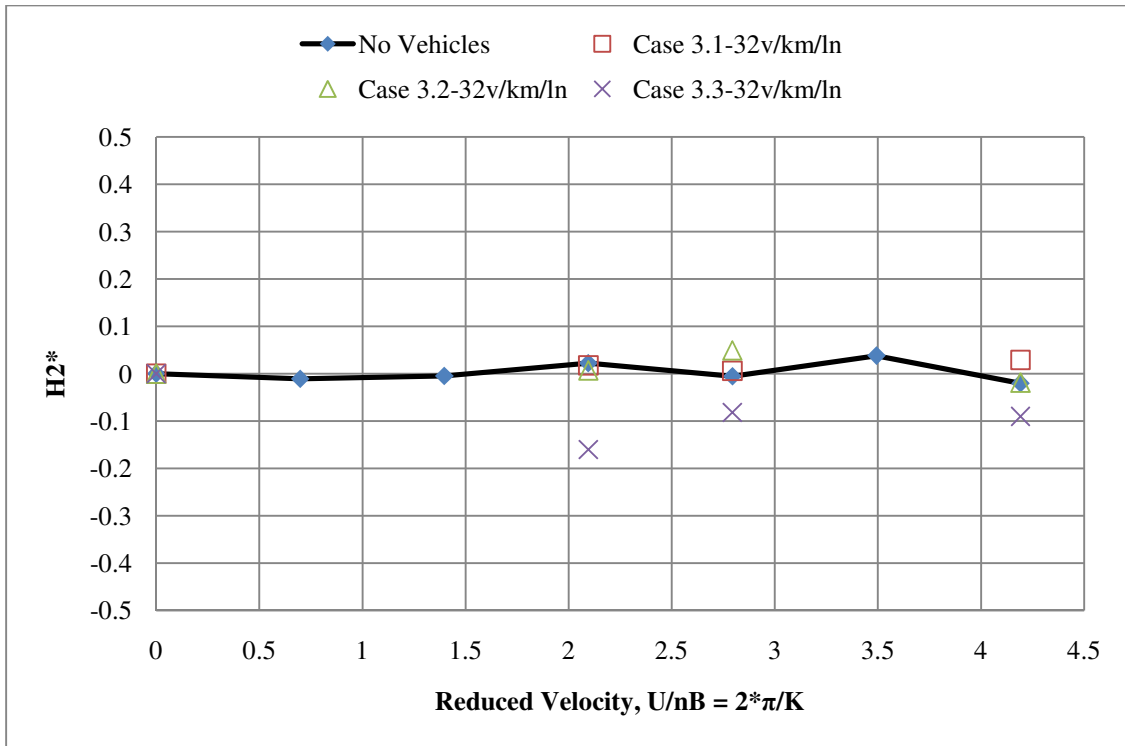


Figure 3.24: Flutter derivative  $H2^*$  for Spatial Cases 3.1-3.3

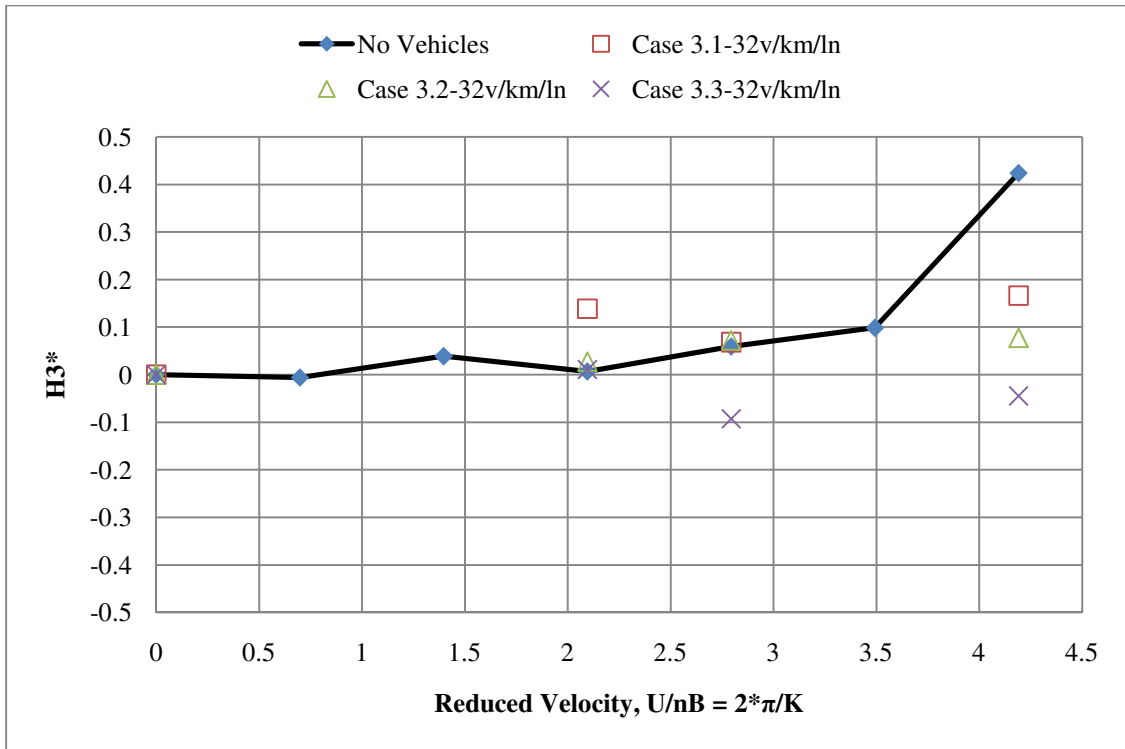


Figure 3.25: Flutter derivative  $H3^*$  for Spatial Cases 3.1-3.3

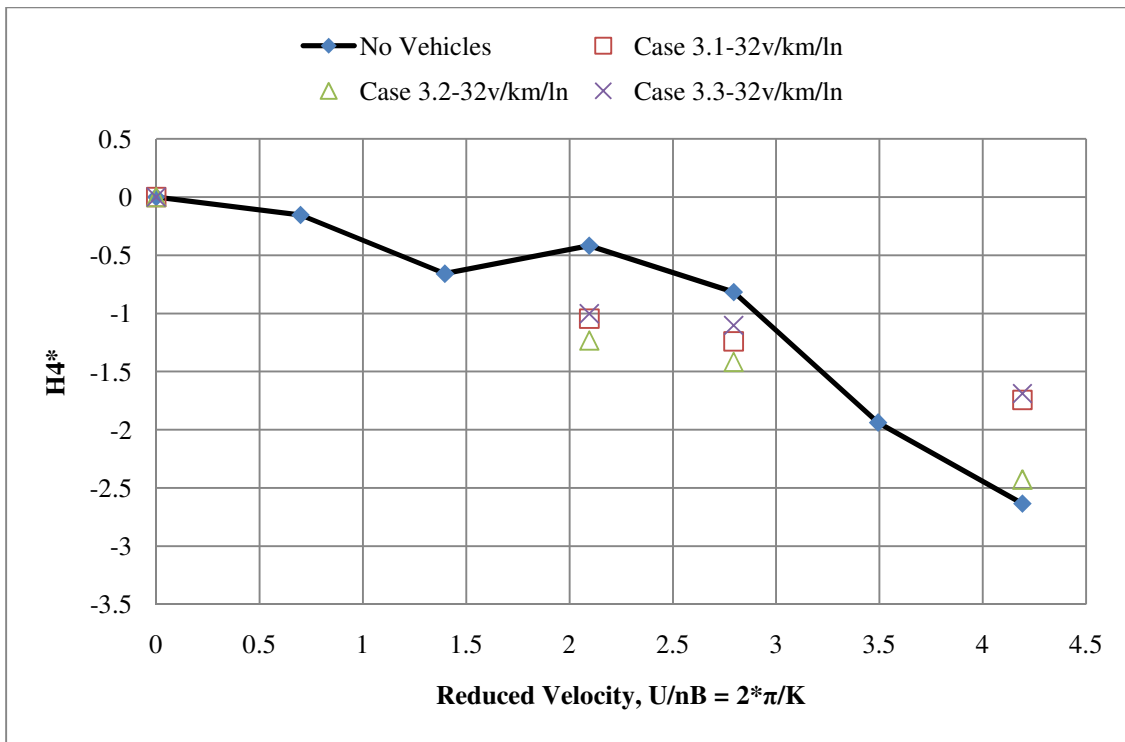


Figure 3.26: Flutter derivative  $H4^*$  for Spatial Cases 3.1-3.3

### 3.3 Time Dependent Traffic Test Results

Following two scenarios will be studied:

1. Traffic density of 20 vehicles/km/ln
2. Traffic density of 32 vehicles/km/ln

#### 3.3.1 Time Cases 1.1-1.3 with 20 vehicles/km/ln

The time-continuous studies are different from the spatial-continuous studies as discussed in Section 3.2. The time-continuous study utilizes the same segment in the middle of the main span of the bridge. The “snapshots” are taken at the same segment continuously with the 5-second interval of the traffic flow simulated. This is to study the variations of stochastic traffic passing through the same observation location and the impacts on the flutter derivatives. Figure 3.27 shows three “snapshots” of traffic on the same segments at three time instants when traffic density is 20 veh/km/ln. In Figs. 3.28-31 and Figs. 3.32-35 are shown the flutter derivatives of  $A1-4^*$  and  $H1-4^*$ , respectively.

Except for  $H2^*$  and  $H3^*$ , the presence of traffic caused considerable impact on other flutter derivatives. Similar to the previous results, such impacts get more significant when wind speed increases. The comparisons between the results of different time instants disclosed that some flutter derivatives are more sensitive to different time instants when different vehicle distributions exist, such as  $A1-4^*$ , and  $H4^*$ .  $H1^*$  has limited impact by different distributions of traffic at different instants. The results suggest that time-variant characteristics of flutter derivatives of the same traffic flow moving on the bridge need to be considered for most flutter derivatives, especially those related to torsion motion. It is noted that the observation here is purely based on the values of flutter derivatives. The sensitivity analysis of the impacts on flutter critical wind speed or dynamic response from these variations should be conducted, which are beyond the scope of this thesis.

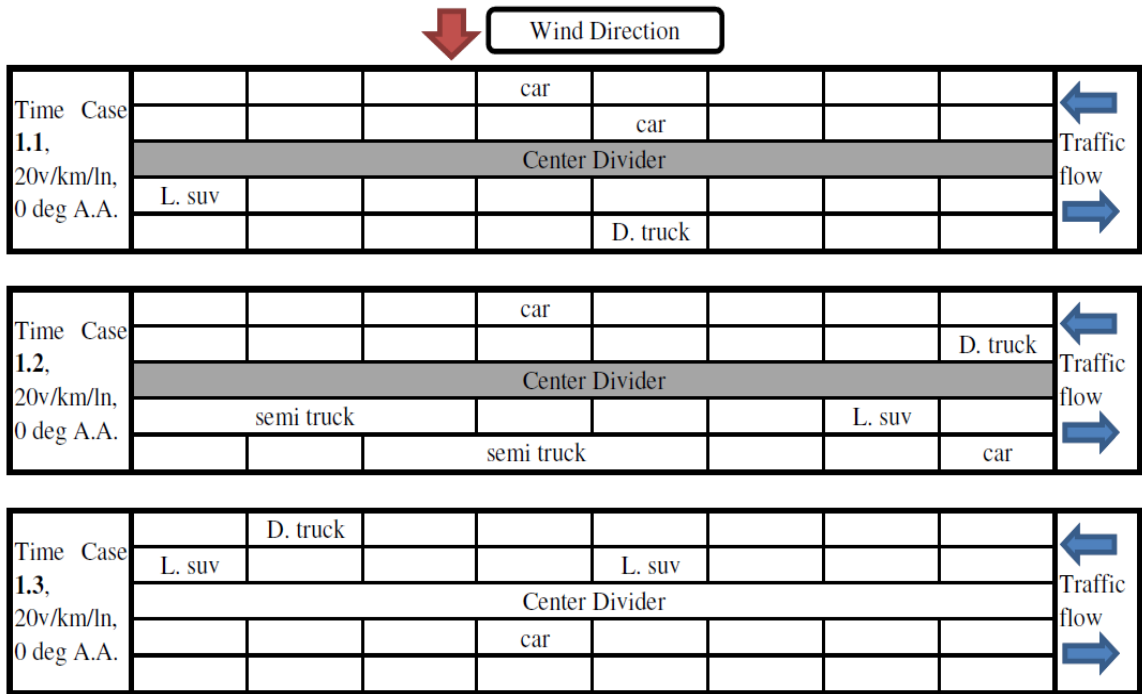


Figure 3.27: Time dependent vehicle positioning for cases 1.1-1.3 with 20 vehicles/km/lane

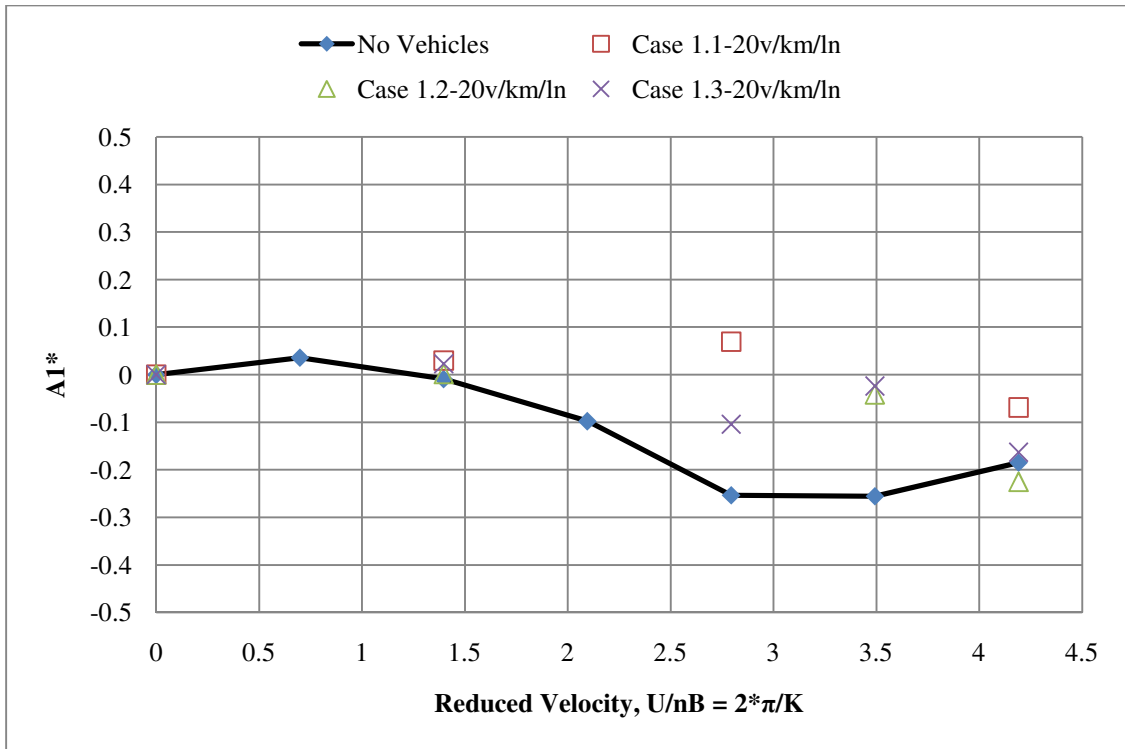


Figure 3.28: Flutter derivative  $A1^*$  for Time Cases 1.1-1.3

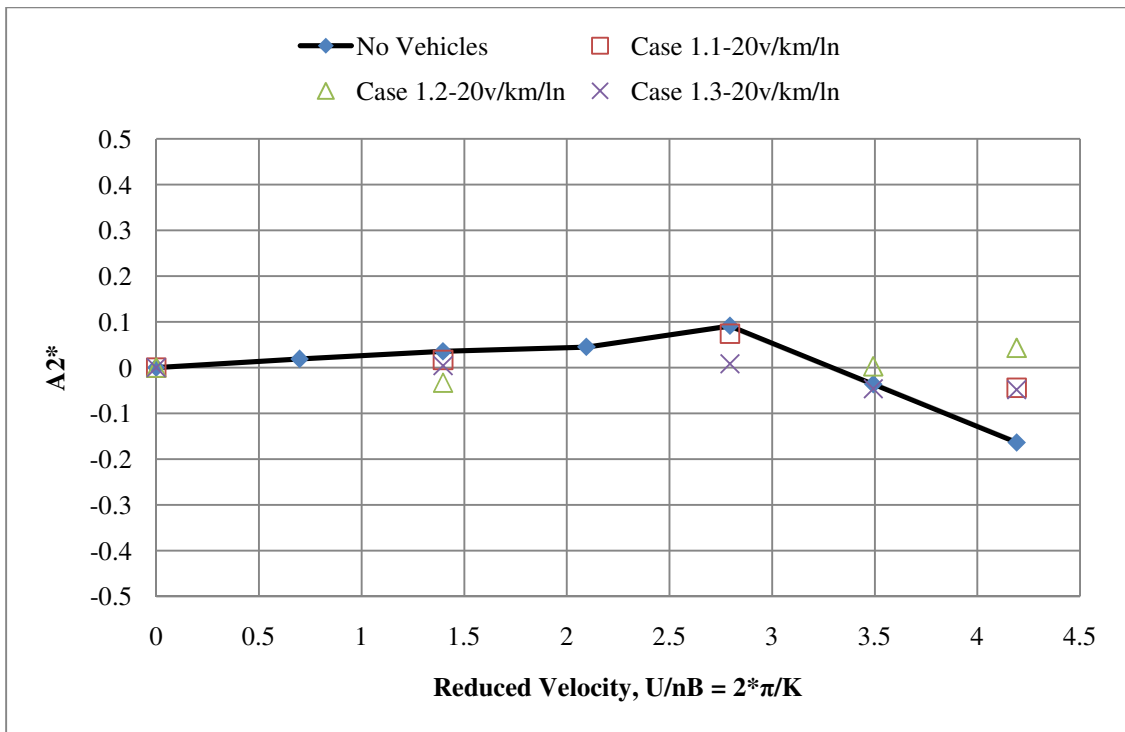


Figure 3.29: Flutter derivative  $A2^*$  for Time Cases 1.1-1.3

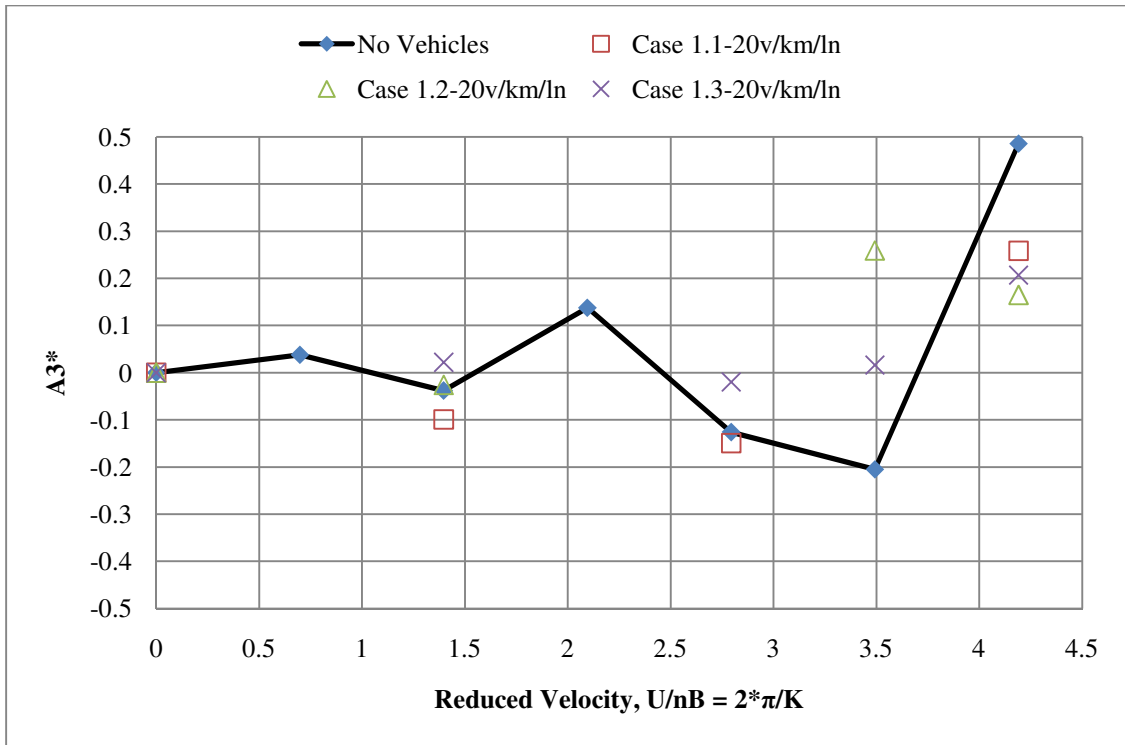


Figure 3.30: Flutter derivative  $A3^*$  for Time Cases 1.1-1.3

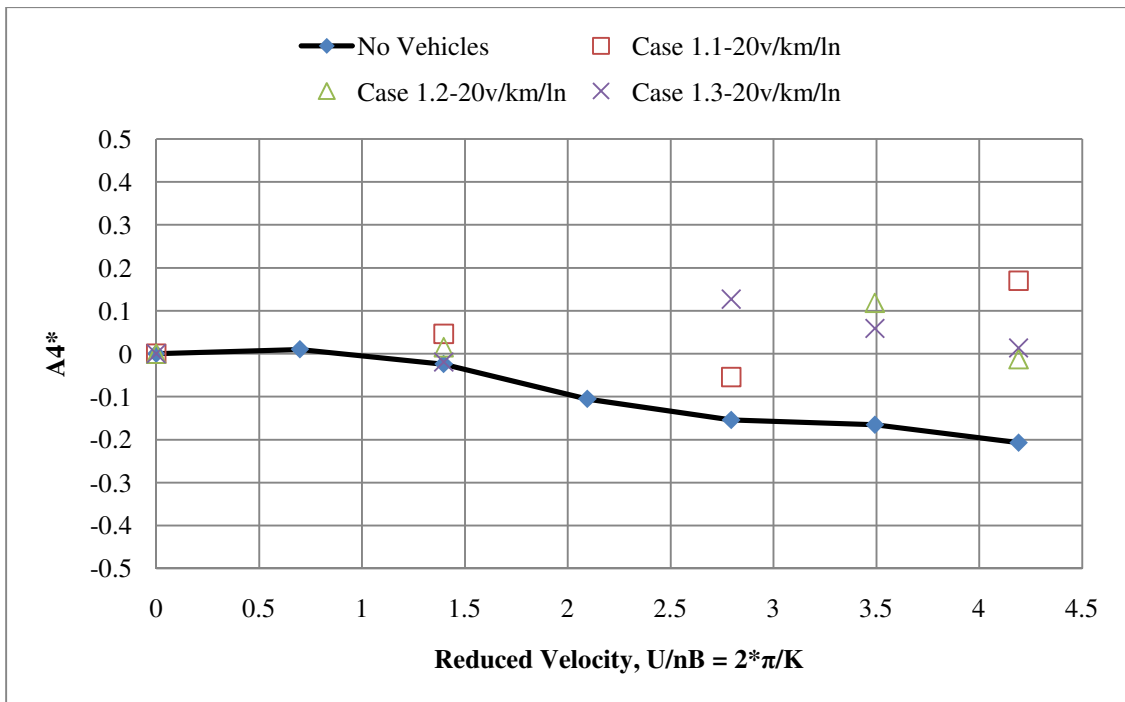


Figure 3.31: Flutter derivative  $A4^*$  for Time Cases 1.1-1.3

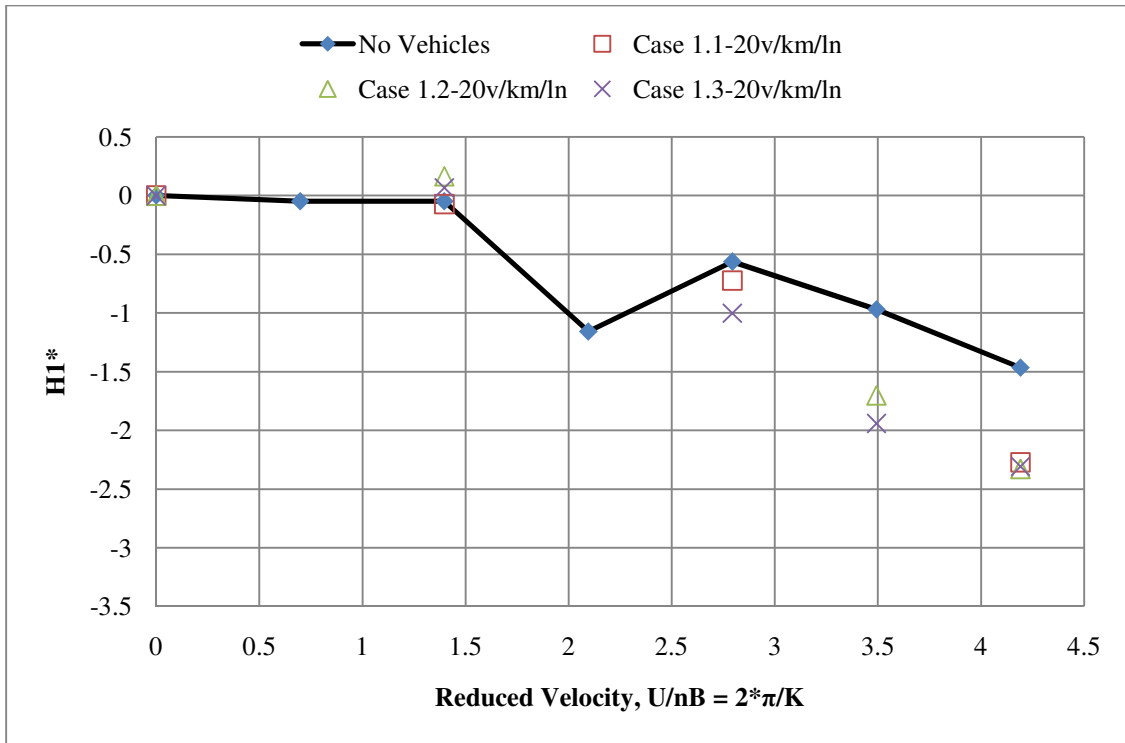


Figure 3.32: Flutter derivative  $H1^*$  for Time Cases 1.1-1.3

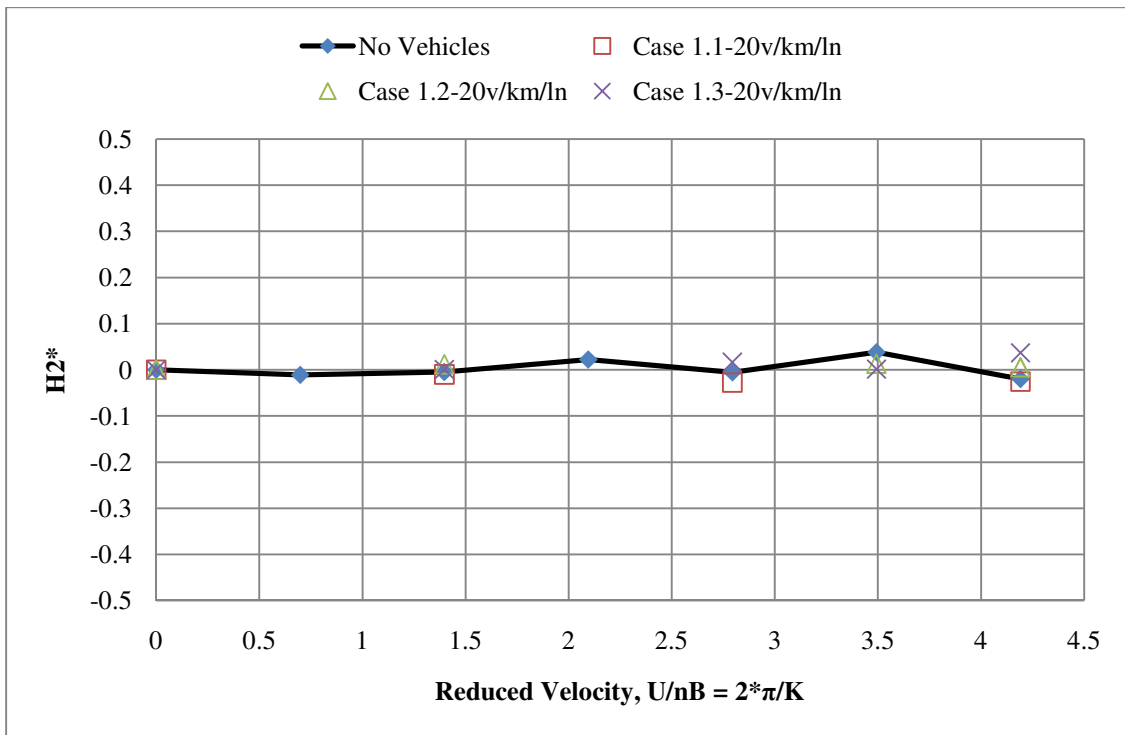


Figure 3.33: Flutter derivative  $H2^*$  for Time Cases 1.1-1.3

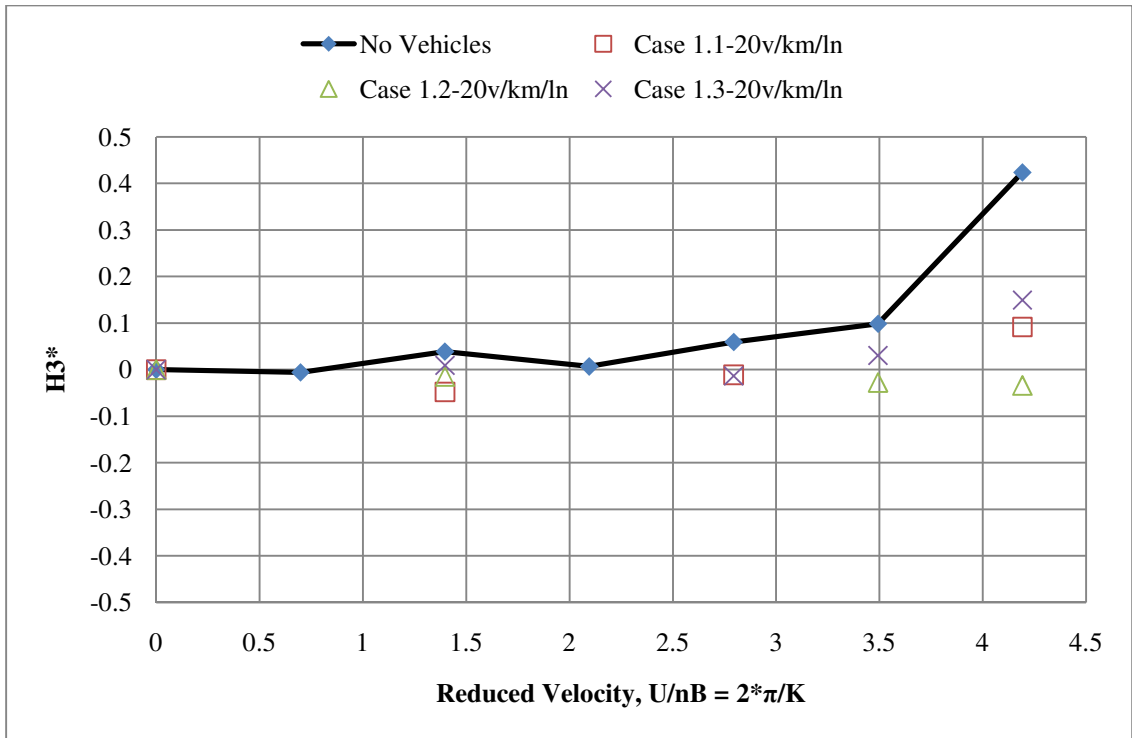


Figure 3.34: Flutter derivative  $H3^*$  for Time Cases 1.1-1.3

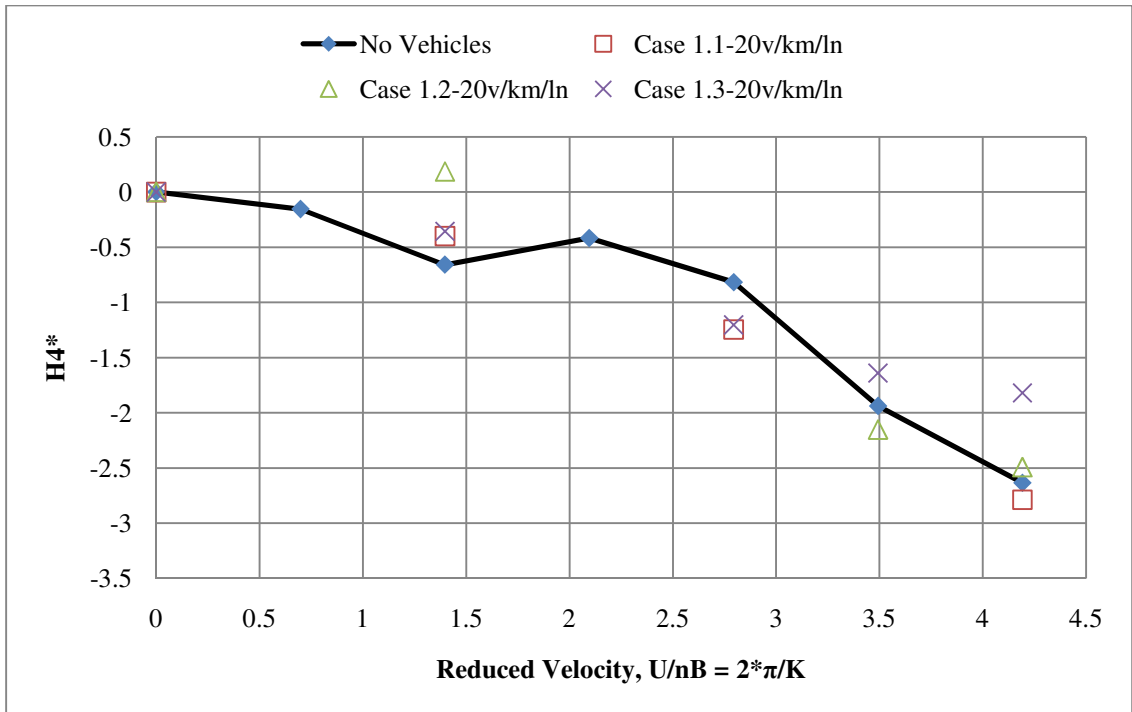


Figure 3.35: Flutter derivative  $H4^*$  for Time Cases 1.1-1.3

### 3.3.2 Time Cases 2.1-2.3 with 32 vehicles/km/ln

When the traffic density equals 32 veh/km/ln, Figure 3.36 gives the corresponding vehicle distributions at three time instants. The flutter derivatives results are shown in Figs. 3.37-44. For busier traffic, similar phenomena can be observed for the results in different time instants. Similar to the spatial-continuous study in the previous section, the increase of traffic density does not cause considerable difference on the flutter derivatives. It is likely that the traffic density is not so critical to flutter derivatives as long as the traffic with moderate or typical traffic densities is considered.

The time dependent cases 1.1-3 and 2.1-3 all exhibit significantly more observed issues with vortex shedding at low wind velocities. In most of the figures below, it can be seen that the data points vary from case to case as the reduced velocity had to be adjusted to achieve reasonable data for flutter derivative calculations. The vortex shedding phenomenon is discussed further in Section 3.7.

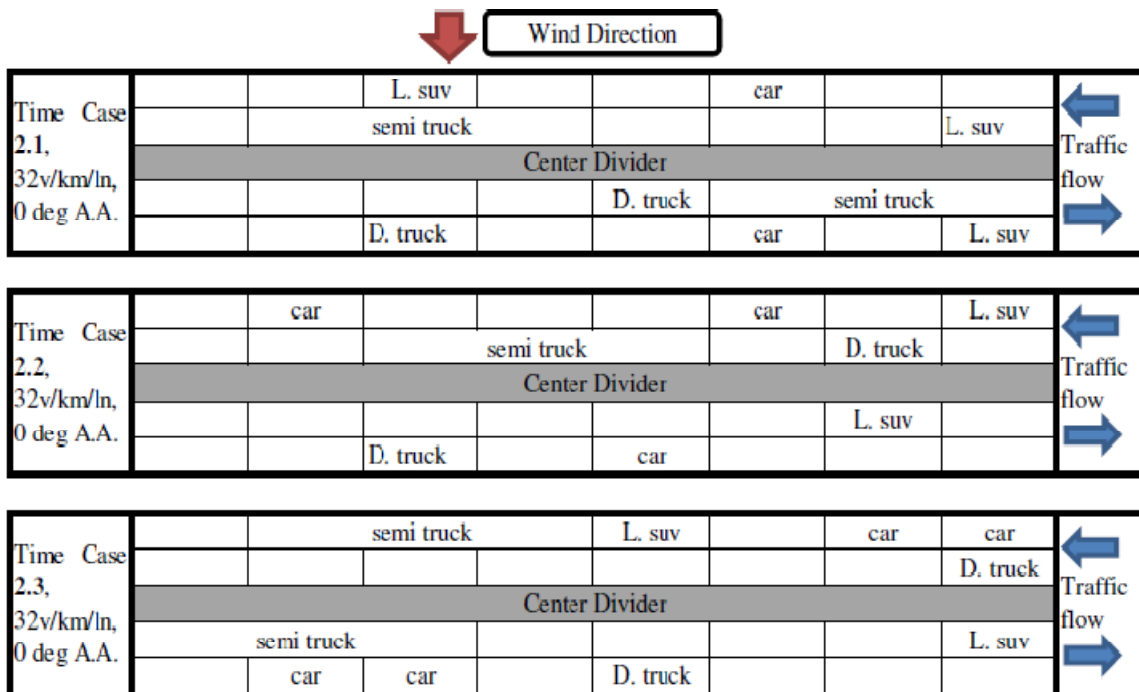


Figure 3.36: Time dependent vehicle positioning for cases 2.1-2.3 with 32 vehicles/km/lane

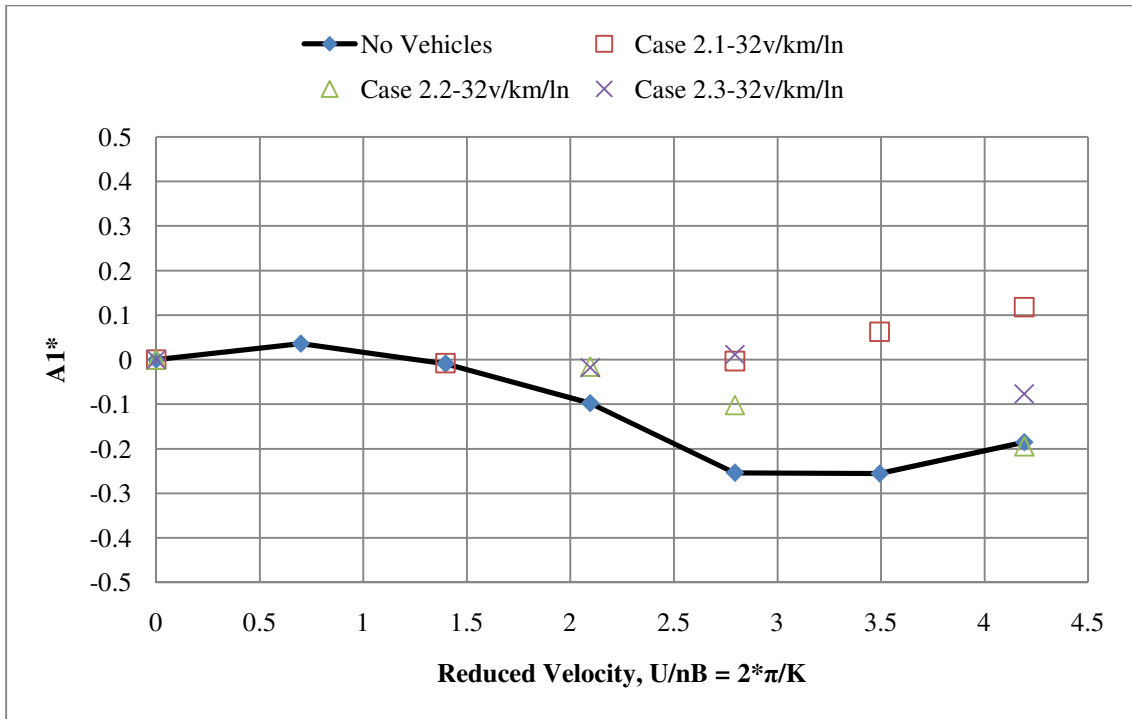


Figure 3.37: Flutter derivative  $A1^*$  for Time Cases 2.1-2.3

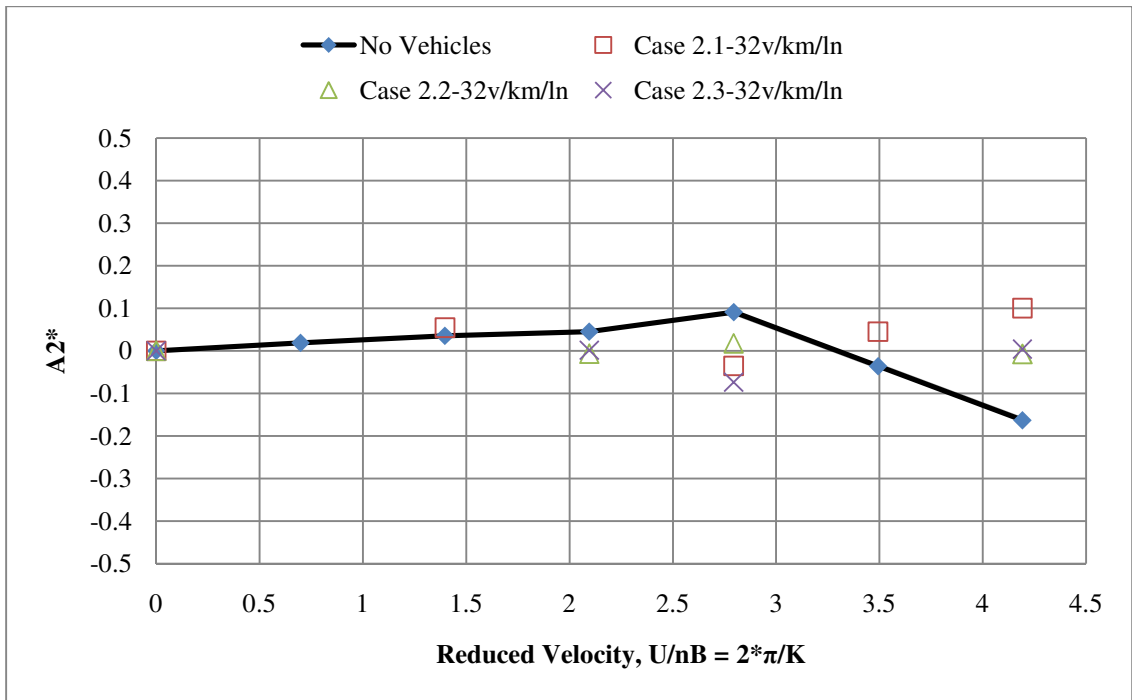


Figure 3.38: Flutter derivative  $A2^*$  for Time Cases 2.1-2.3

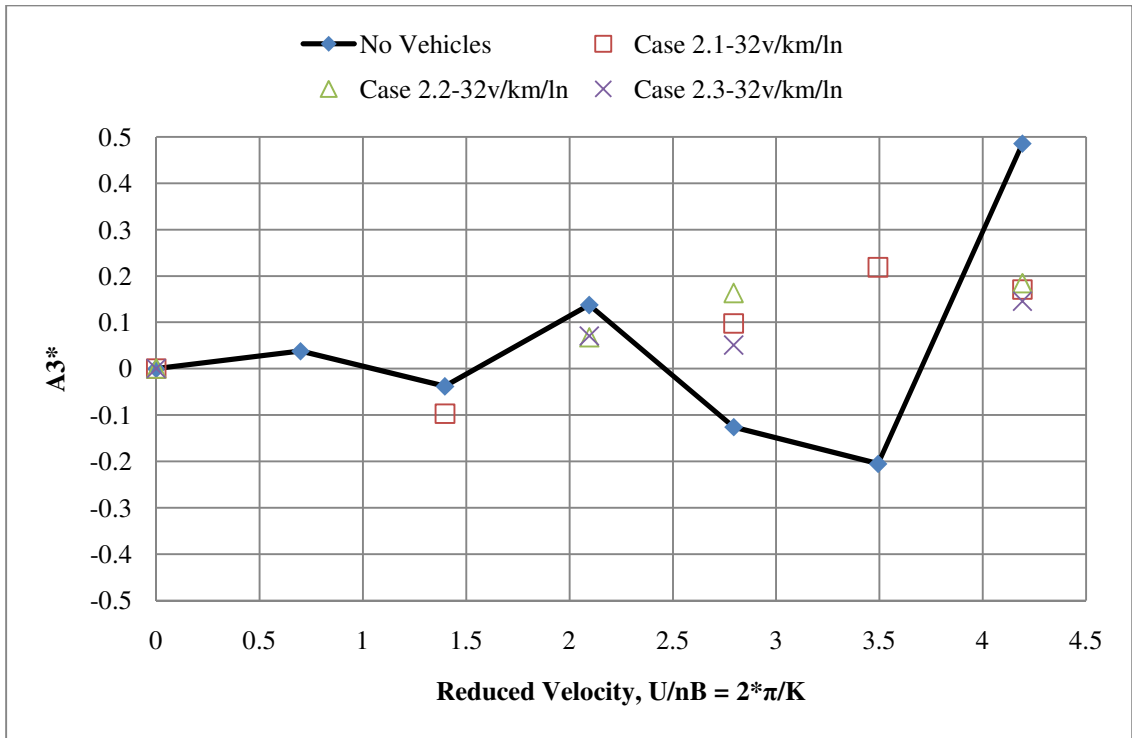


Figure 3.39: Flutter derivative  $A3^*$  for Time Cases 2.1-2.3

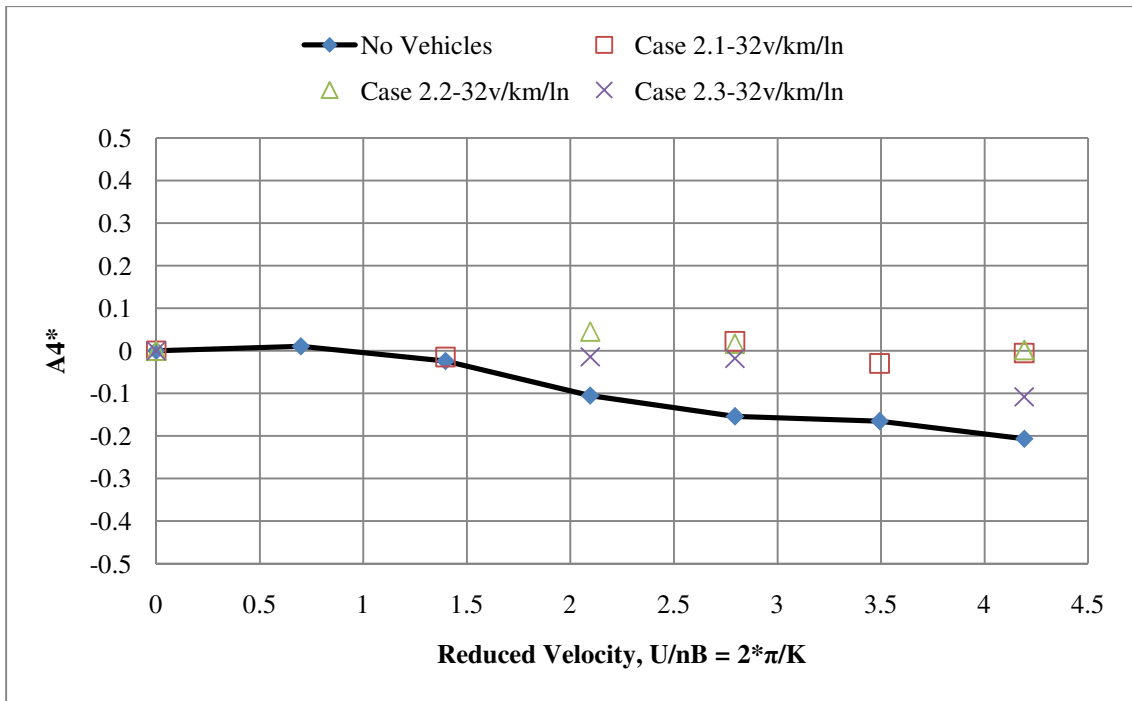


Figure 3.40: Flutter derivative  $A4^*$  for Time Cases 2.1-2.3

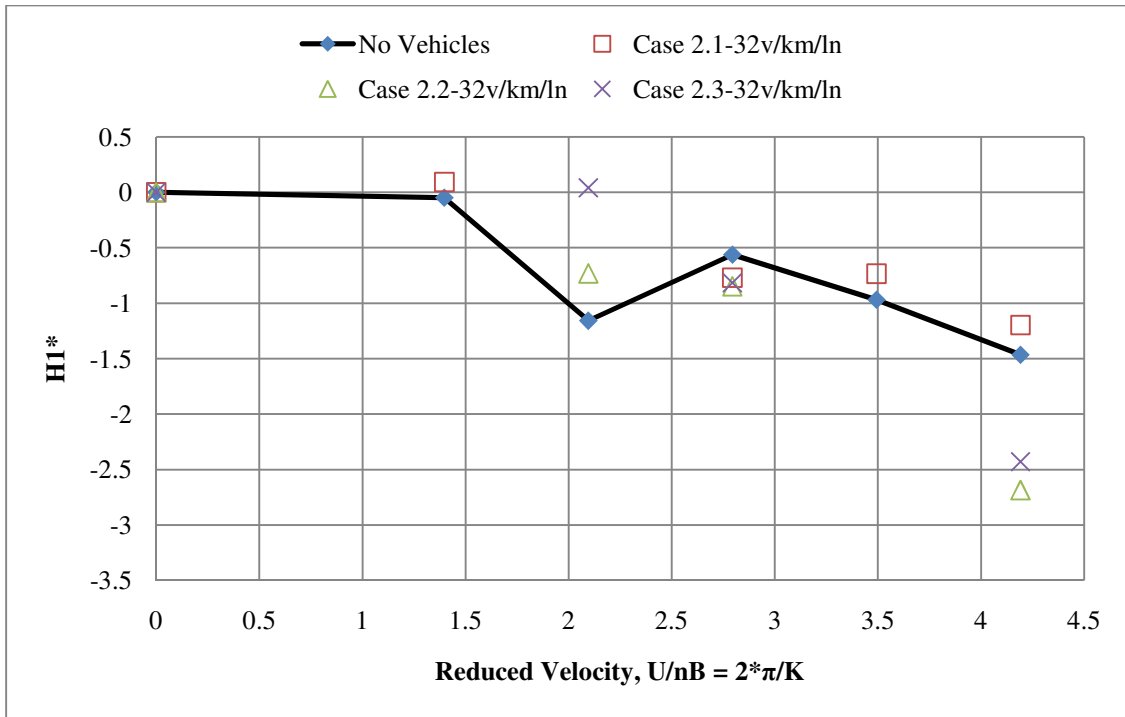


Figure 3.41: Flutter derivative  $H1^*$  for Time Cases 2.1-2.3

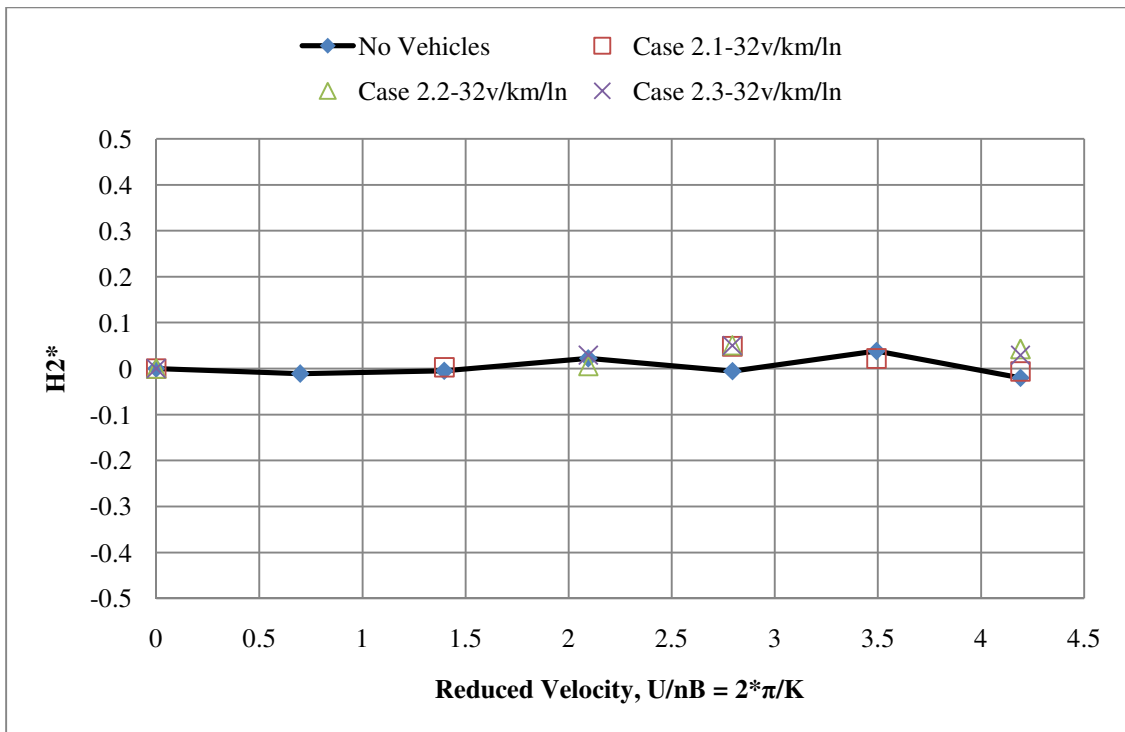


Figure 3.42: Flutter derivative  $H2^*$  for Time Cases 2.1-2.3

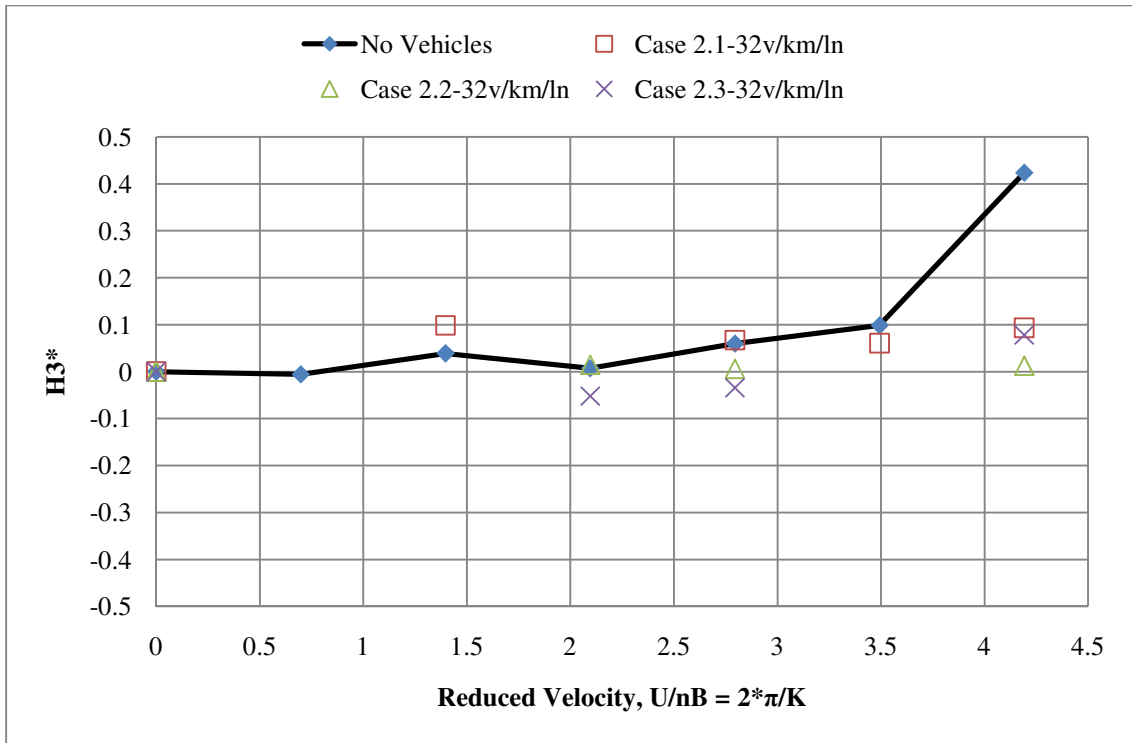


Figure 3.43: Flutter derivative  $H3^*$  for Time Cases 2.1-2.3

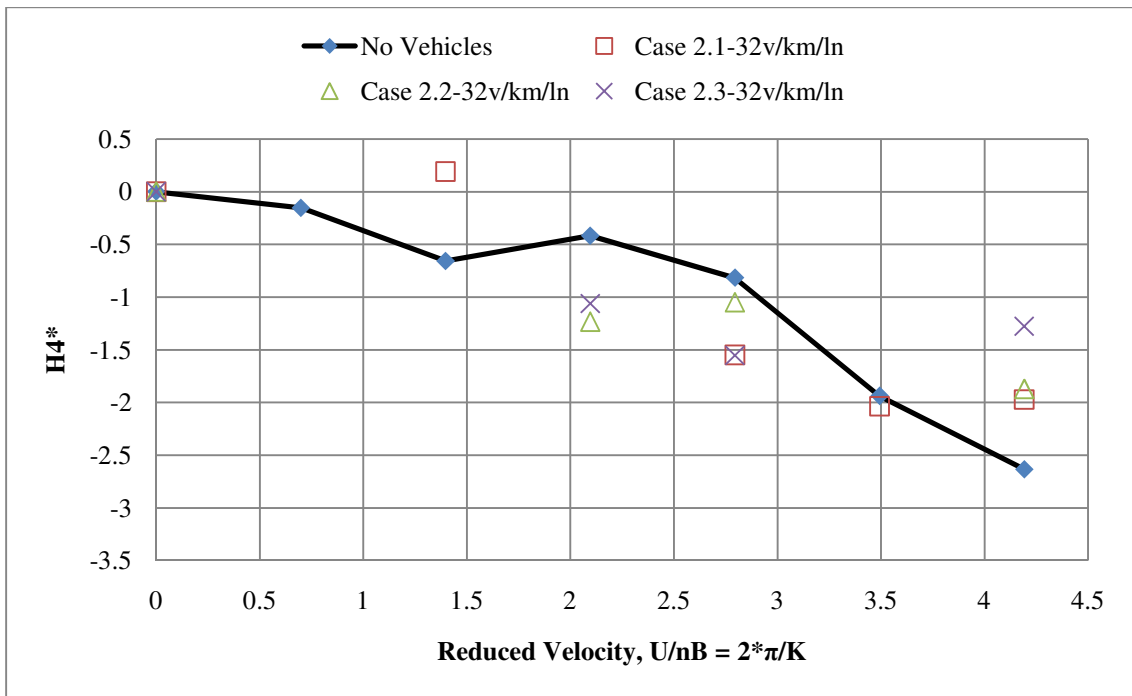


Figure 3.44: Flutter derivative  $H4^*$  for Time Cases 2.1-2.3

## 3.4 Extreme Traffic Test Results

### 3.4.1 Extreme Traffic Zero Attack Angle

The extreme traffic conditions represent the worst cases scenarios being:

1. Bumper to bumper vehicles on both sides;
2. Bumper to bumper vehicles on windward side only; and
3. Bumper to bumper vehicles on leeward side only.

These scenarios are representative of the possible emergency evacuation or accident conditions. The extreme traffic scenarios were also examined at different attack angles (e.g.  $\pm 3^\circ$ ). The flutter derivatives for the zero attack angle scenarios are shown in Figs. 3.46-53. The flutter derivatives were found to exhibit very little change as compared to without traffic, with the exception being the  $A1^*$ ,  $A4^*$  and  $H4^*$ , which showed trends of becoming positive sooner than the results of without traffic. There were also interesting changes shown in Figure 3.50 at the reduced velocities of 1.39 and 2.09, this is believed to be connected with the vortex shedding phenomenon, which was visually witnessed during testing. The testing results for the case with bumper to bumper vehicles on both sides did not utilize the reduced velocity of 1.39 and the bumper to bumper vehicles on leeward side only case did not utilize the reduced velocity of 2.09, because of the vortex shedding phenomenon.

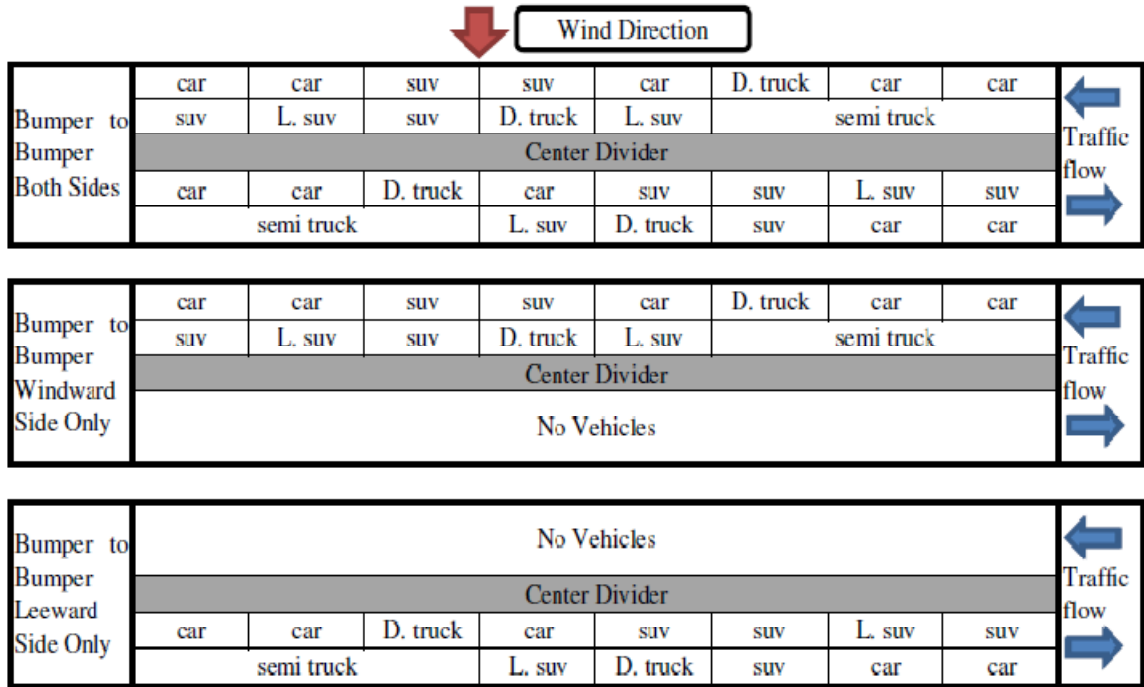


Figure 3.45: Extreme traffic scenarios vehicle layouts

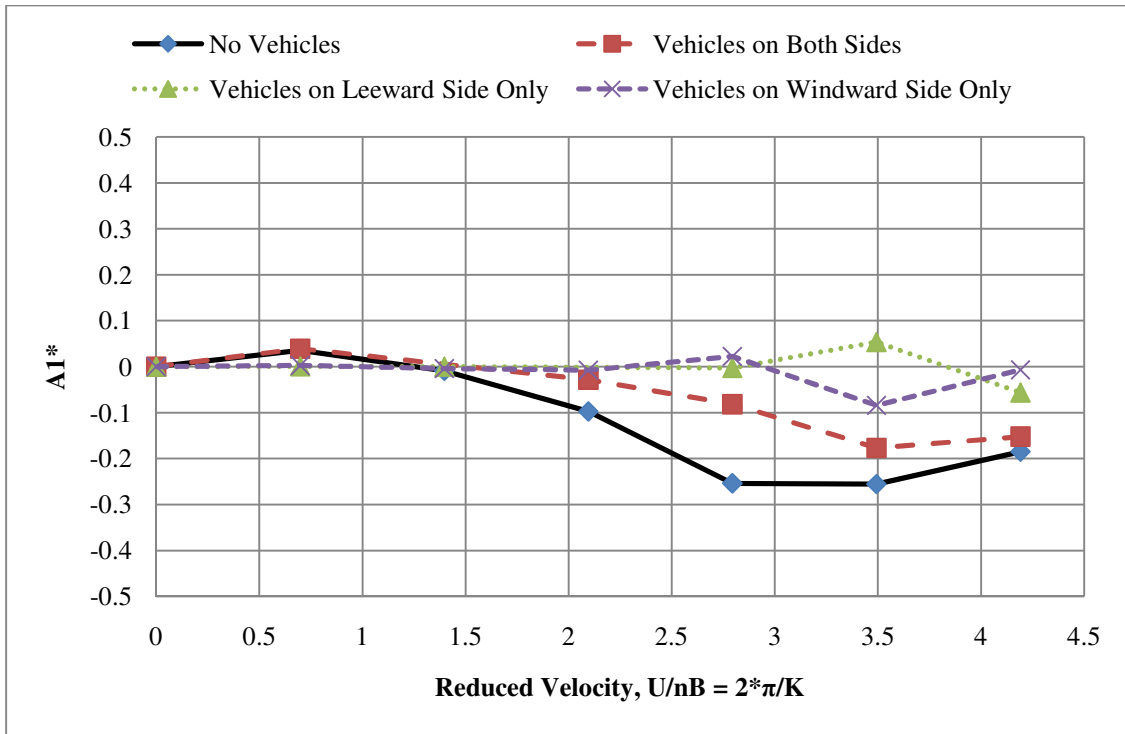


Figure 3.46: Flutter derivative  $A1^*$  for extreme traffic scenarios

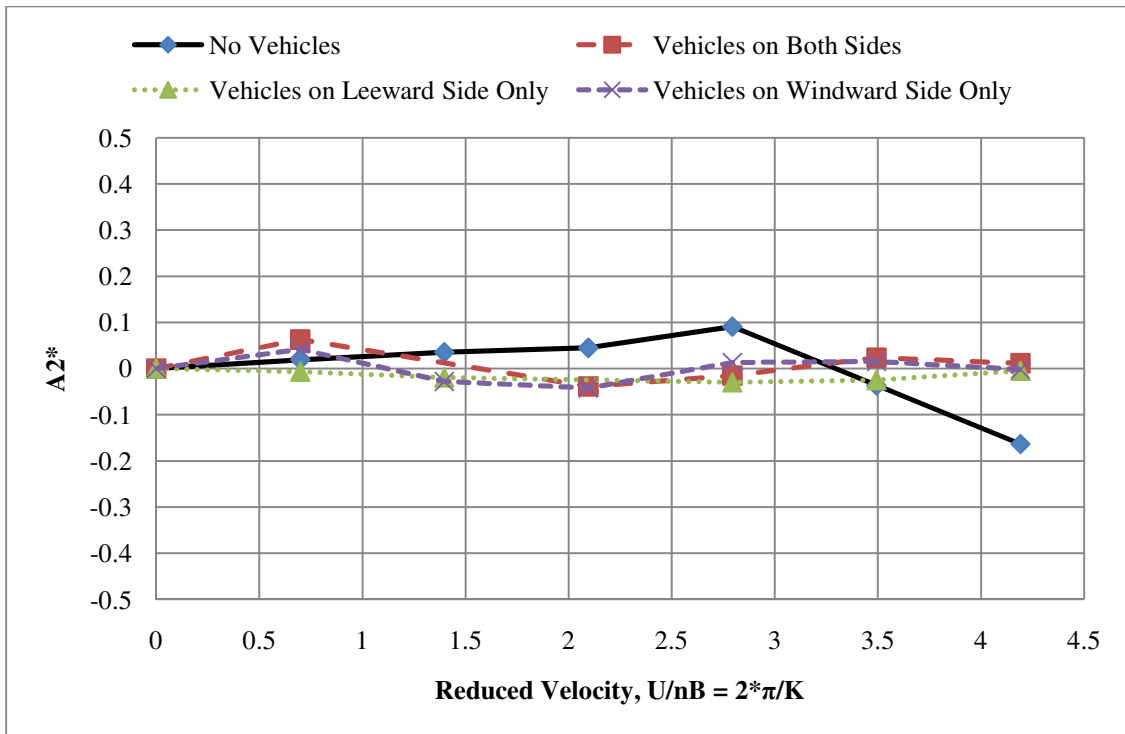


Figure 3.47: Flutter derivative  $A2^*$  for extreme traffic scenarios

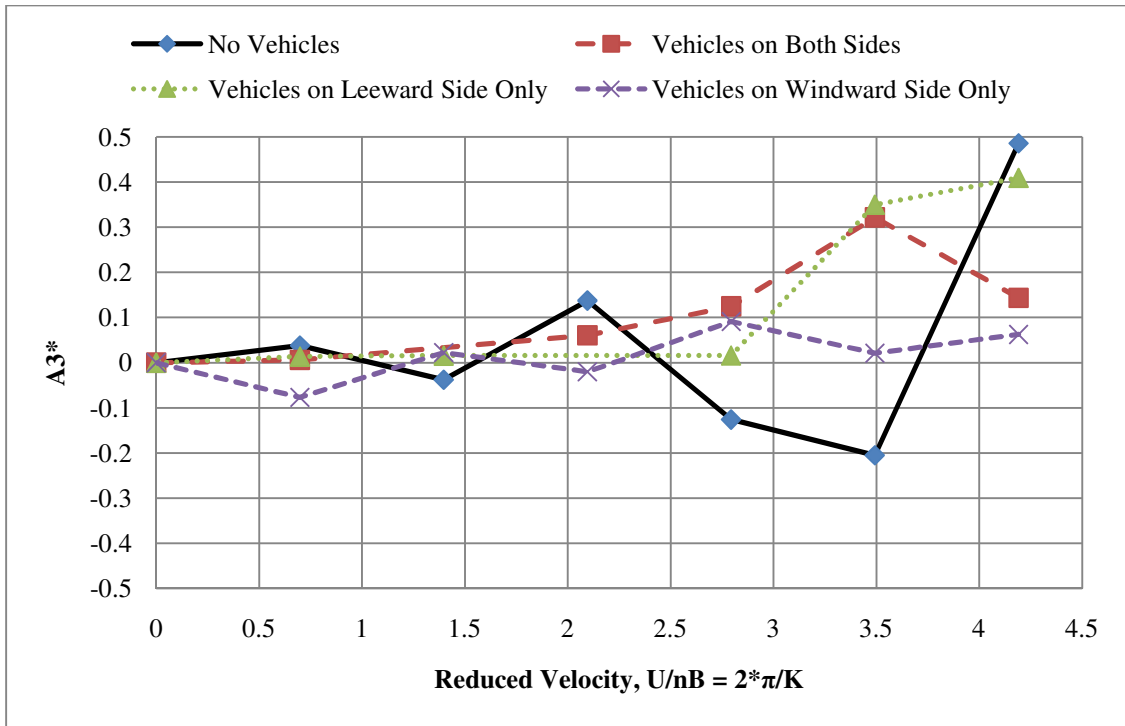


Figure 3.48: Flutter derivative  $A3^*$  for extreme traffic scenarios

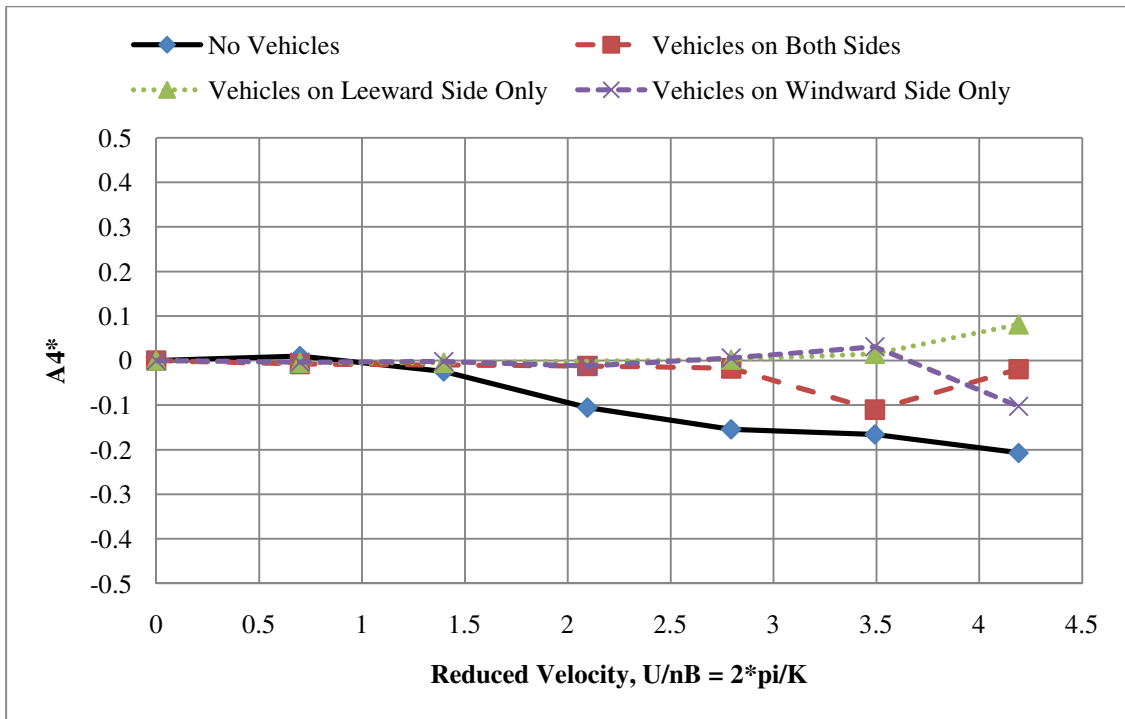


Figure 3.49: Flutter derivative  $A4^*$  for extreme traffic scenarios

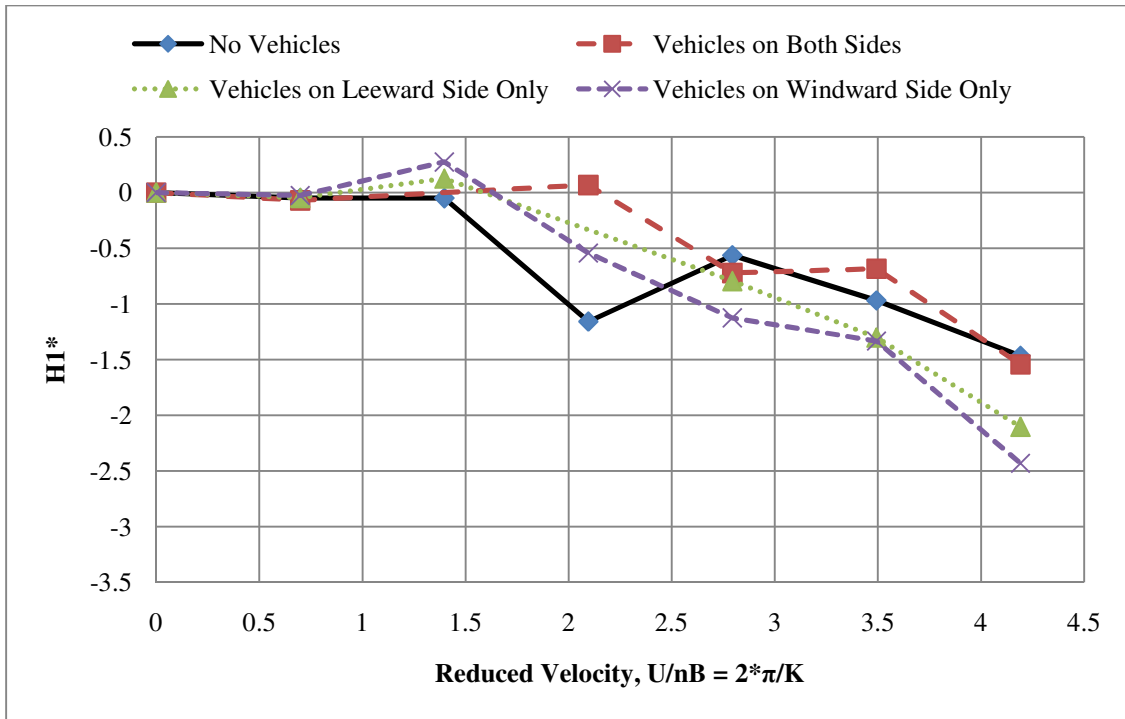


Figure 3.50: Flutter derivative  $H1^*$  for extreme traffic scenarios

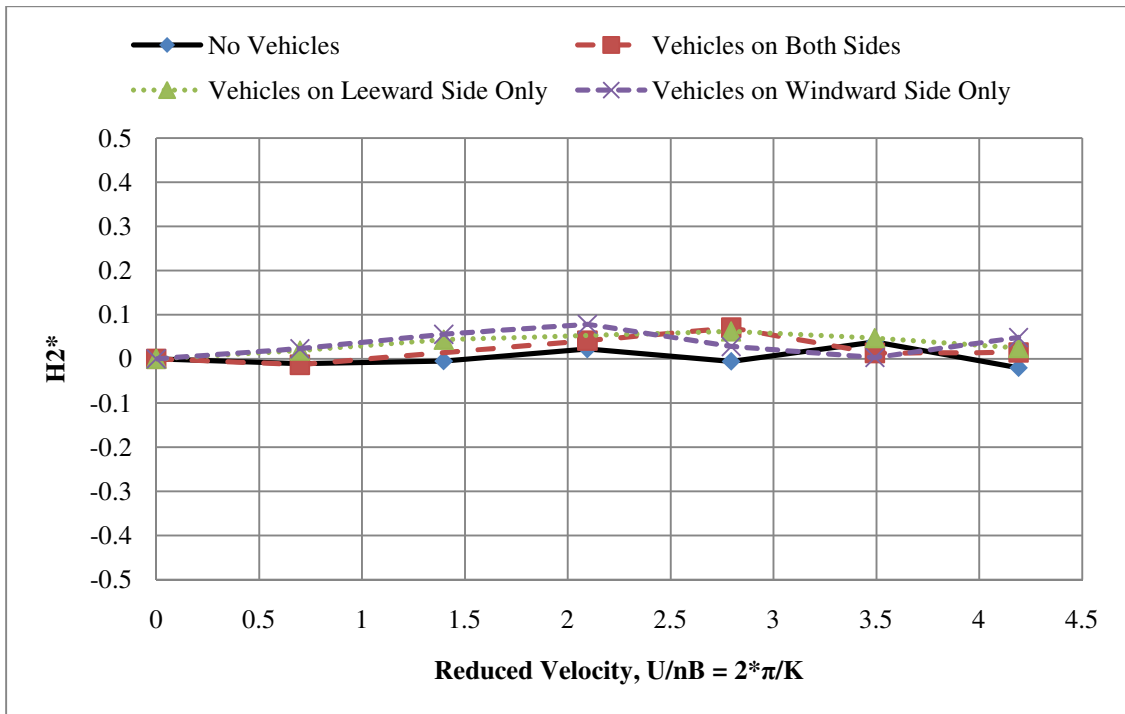


Figure 3.51: Flutter derivative  $H2^*$  for extreme traffic scenarios

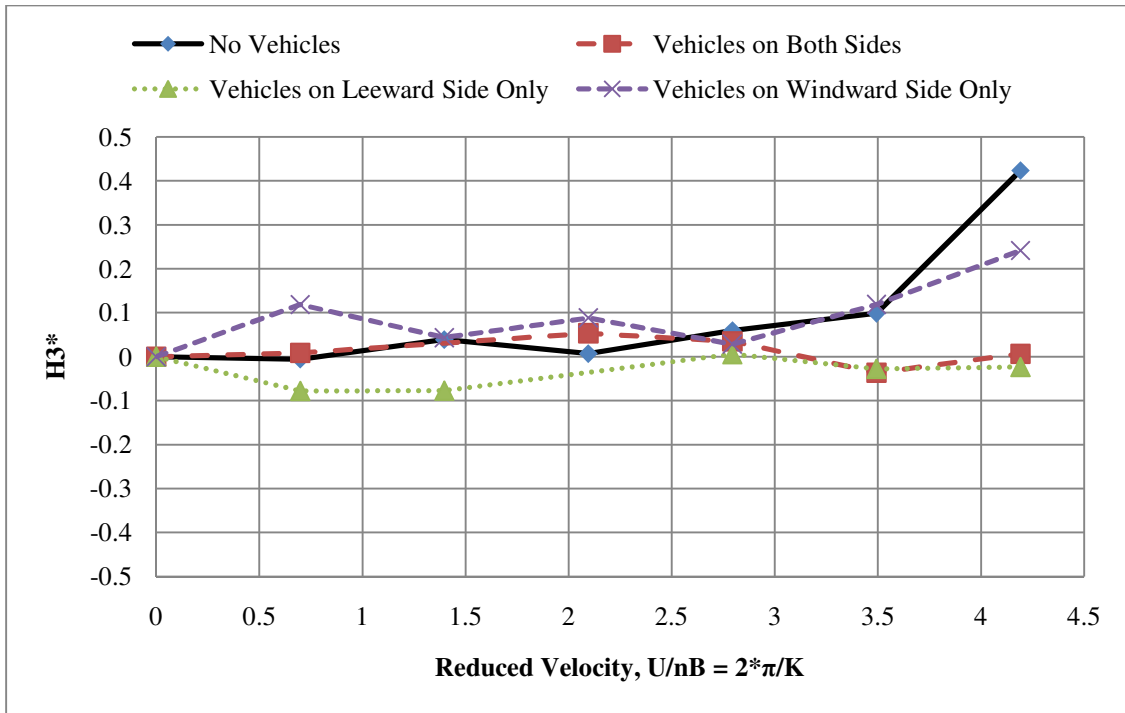


Figure 3.52: Flutter derivative  $H3^*$  for extreme traffic scenarios

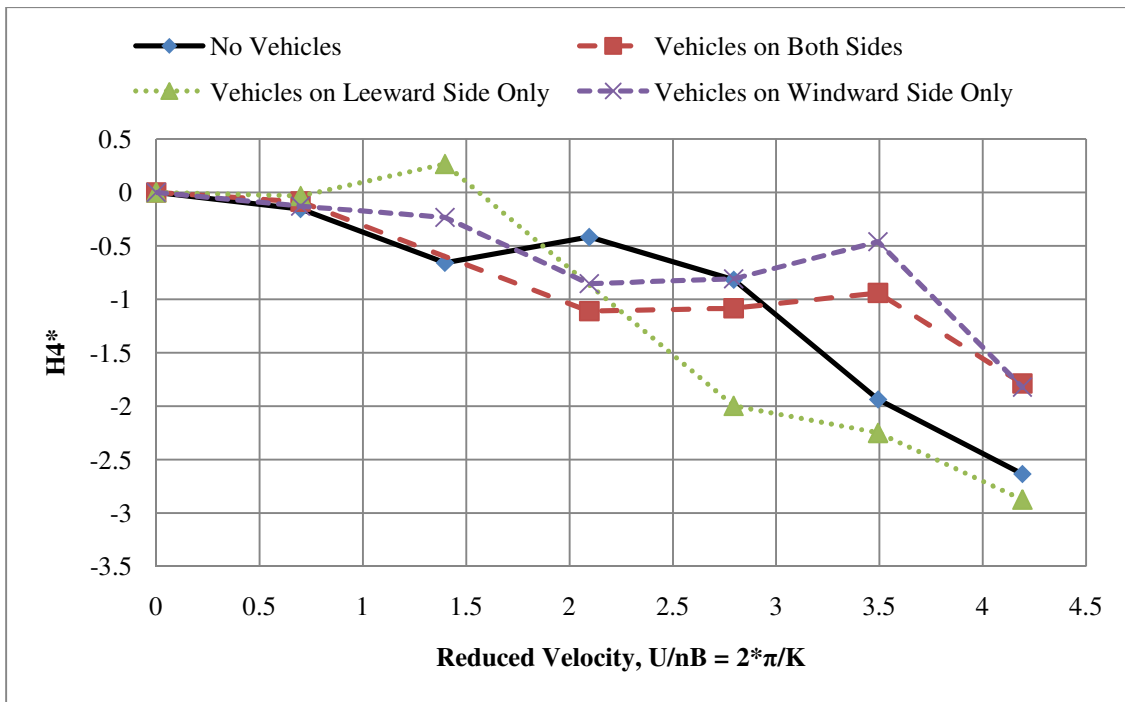


Figure 3.53: Flutter derivative  $H4^*$  for extreme traffic scenarios

### 3.4.2 Extreme Traffic Scenarios with negative 3° Attack Angle

The change of the attack angle for the wind flow was achieved by rotating the bridge about its long axis as shown in Figure 3.54. The bridge section was then re-tested for the 3 extreme cases. The results of the flutter derivatives can be seen in Figs. 3.55-62. The  $A2^*$  flutter derivative in Fig. 3.56 appears to indicate a positive trend for each case at the higher reduced velocities. With  $A2^*$  reversing sign, it is possible that the aerodynamic damping becomes negative, which may result in aerodynamic instability. The  $-3^\circ$  attack angle did not visually produce any significant observed vortex shedding as seen during the testing at zero attack angle.

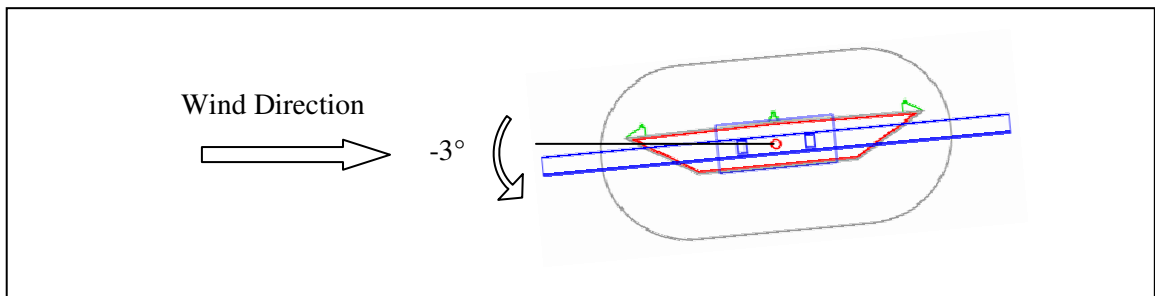


Figure 3.54: Bridge cross-section with 3° negative attack angle

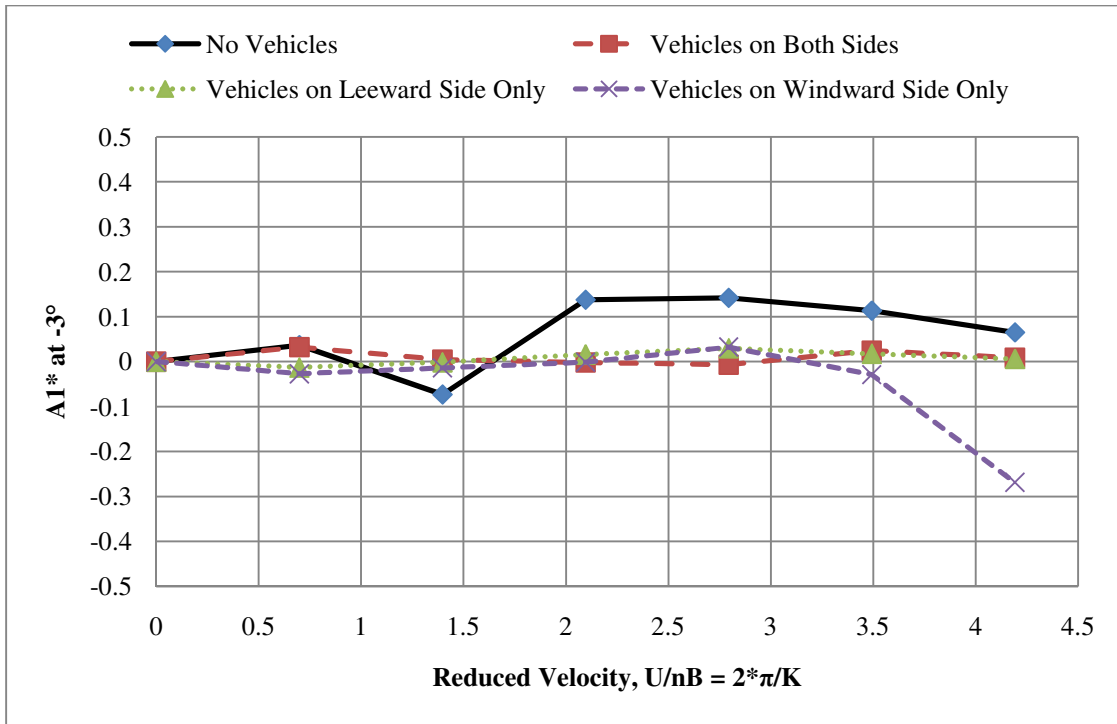


Figure 3.55: Flutter derivative  $A1^*$  for Extreme traffic scenarios with  $-3^\circ$  attack angle

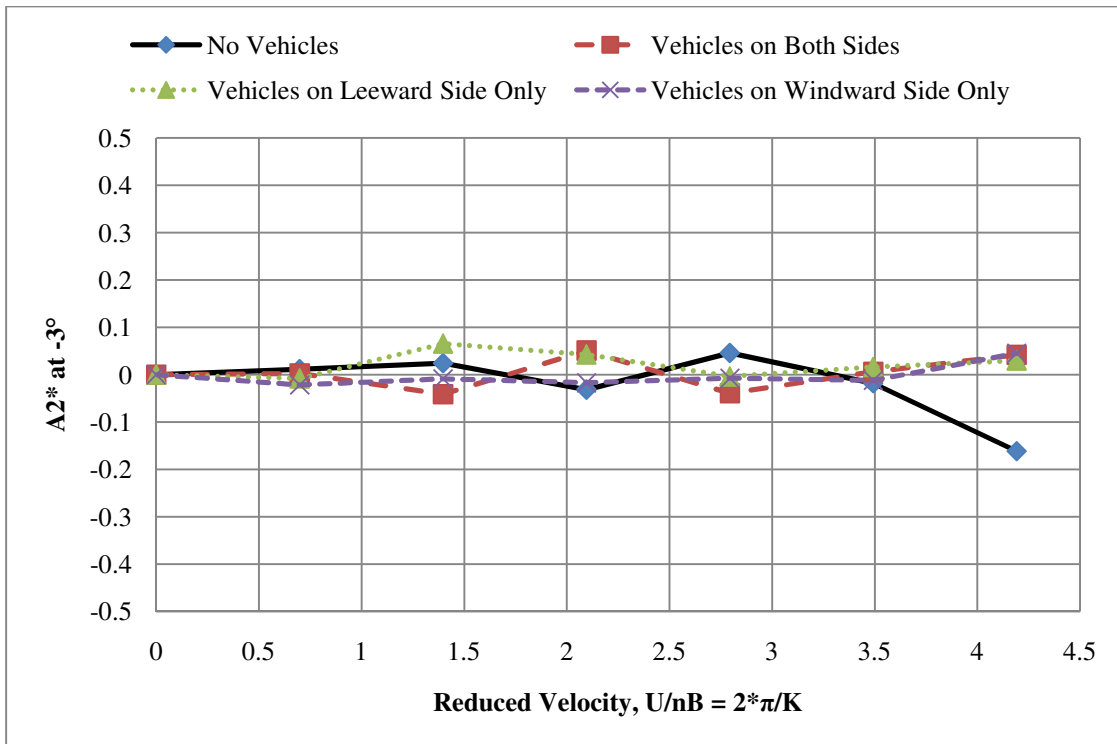


Figure 3.56: Flutter derivative  $A2^*$  for Extreme traffic scenarios with  $-3^\circ$  attack angle

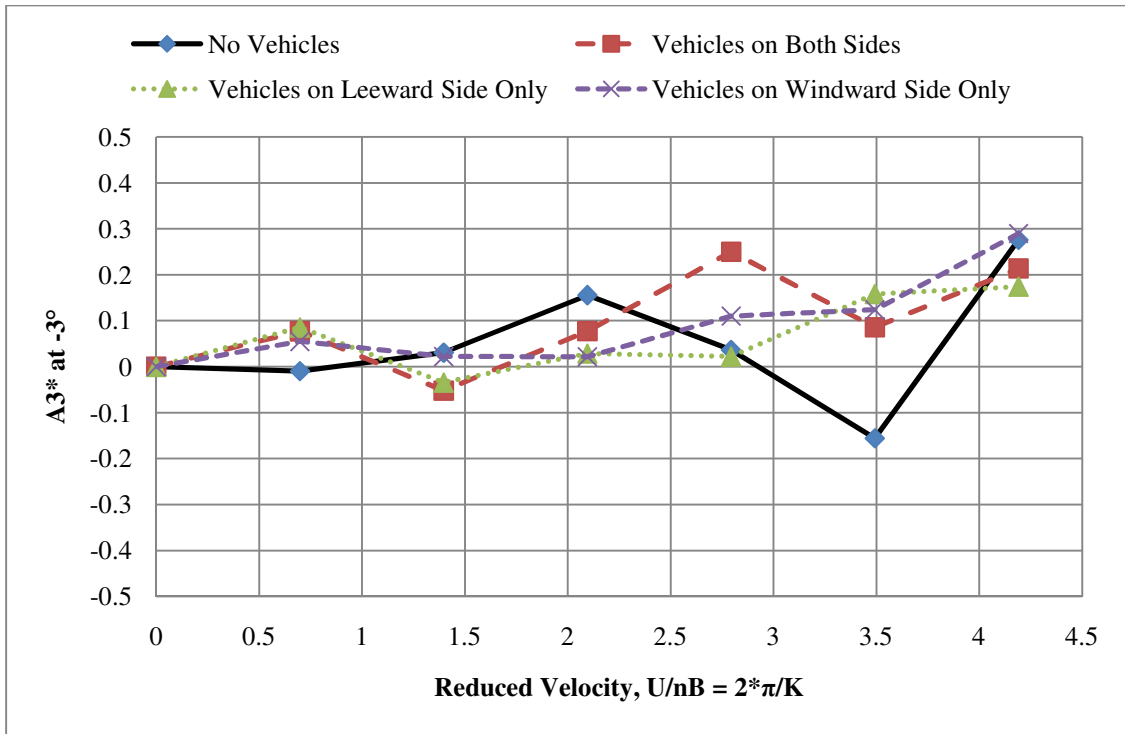


Figure 3.57: Flutter derivative  $A3^*$  for Extreme traffic scenarios with  $-3^\circ$  attack angle

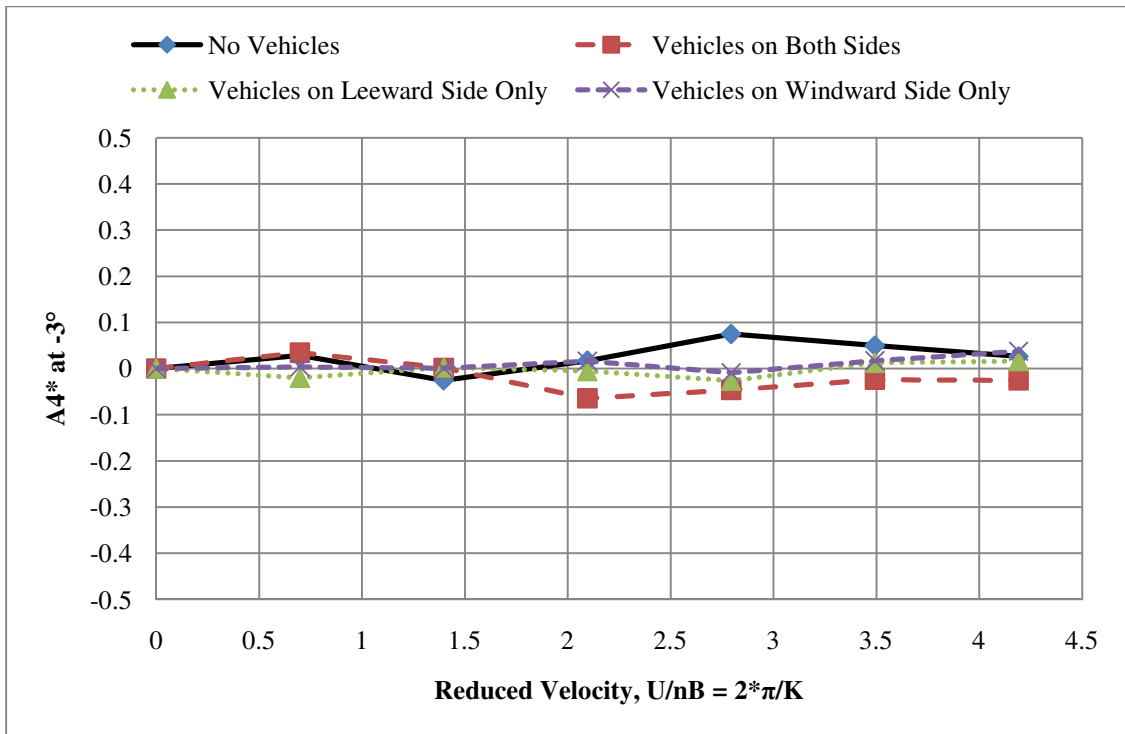


Figure 3.58: Flutter derivative  $A4^*$  for Extreme traffic scenarios with  $-3^\circ$  attack angle

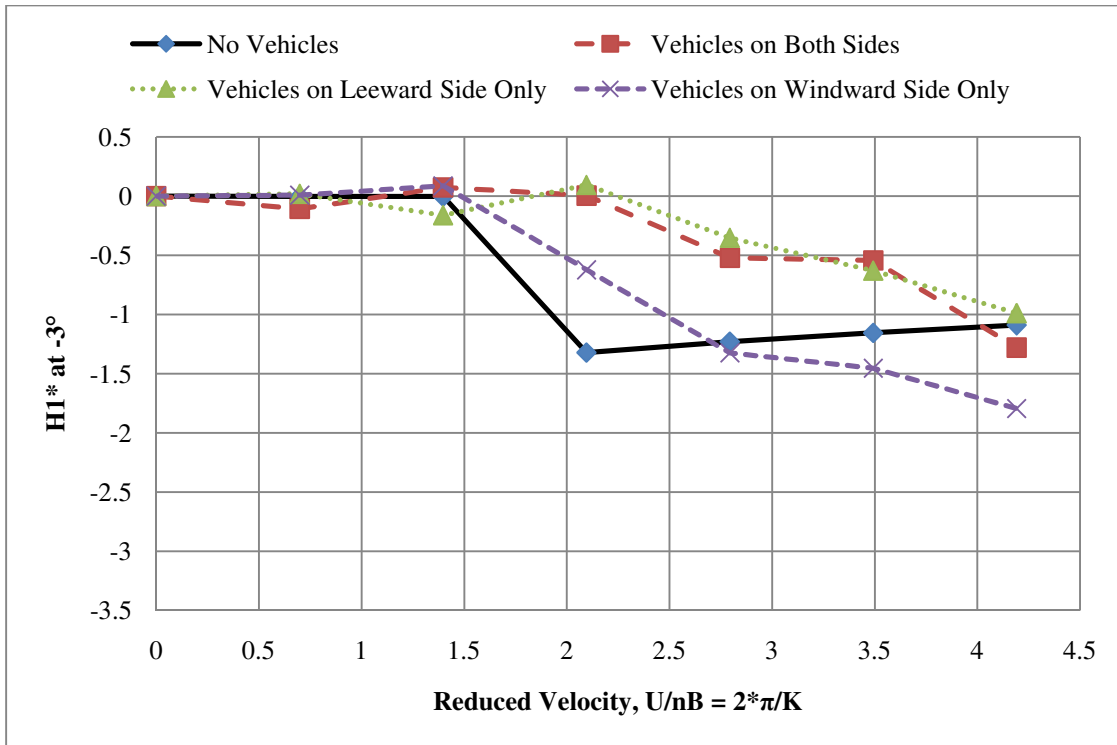


Figure 3.59: Flutter derivative  $H1^*$  for Extreme traffic scenarios with  $-3^\circ$  attack angle

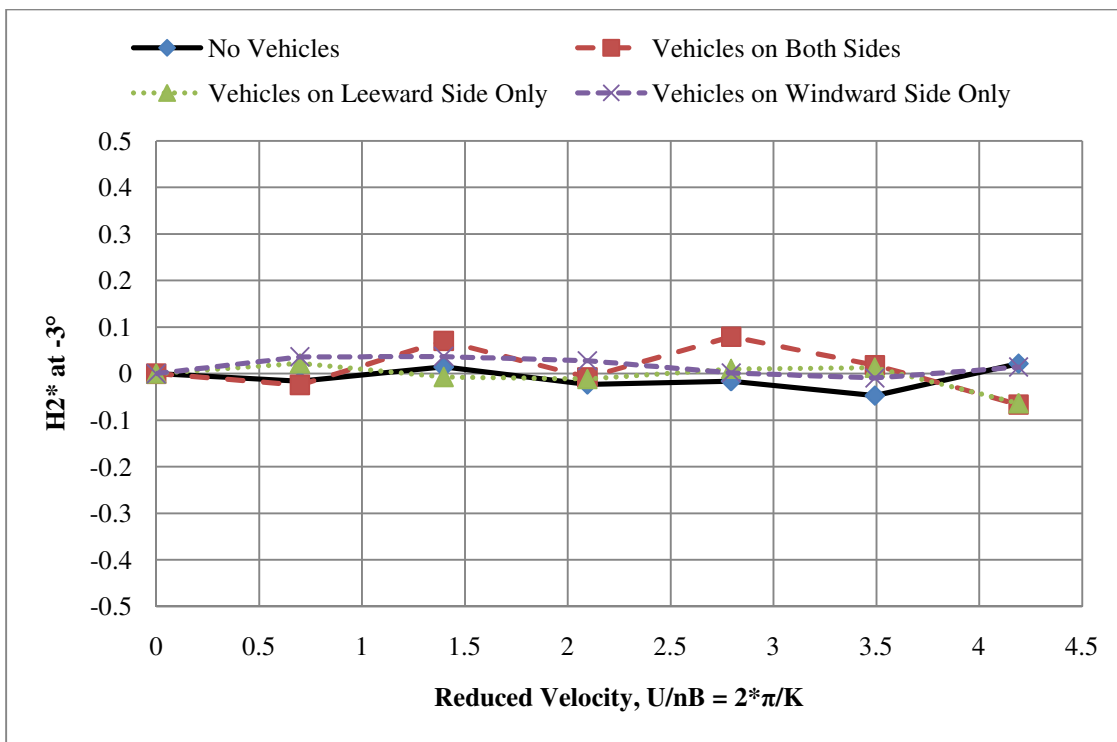


Figure 3.60: Flutter derivative  $H2^*$  for Extreme traffic scenarios with  $-3^\circ$  attack angle

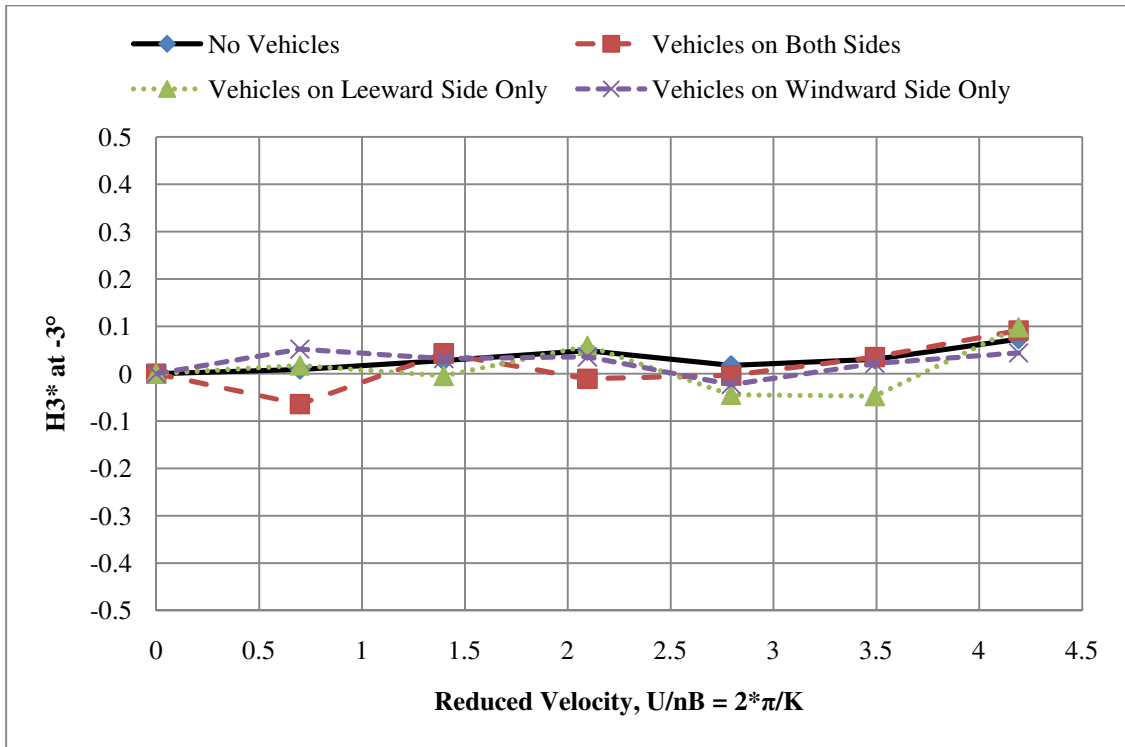


Figure 3.61: Flutter derivative  $H3^*$  for Extreme traffic scenarios with  $-3^\circ$  attack angle

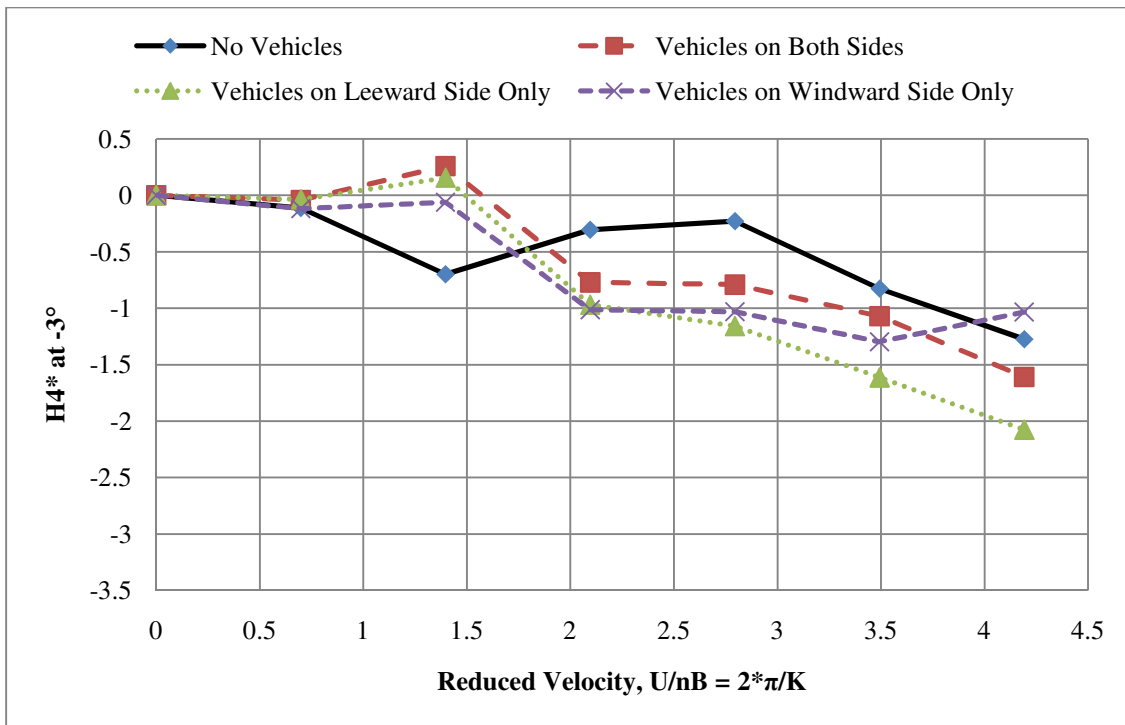


Figure 3.62: Flutter derivative  $H4^*$  for Extreme traffic scenarios with  $-3^\circ$  attack angle

### 3.4.3 Extreme Traffic Scenarios with Positive 3° Attack Angle

The change of the attack angle for the wind flow was achieved by rotating the bridge about its long axis as seen in Figure 3.63. Again the bridge section was then re-tested for the 3 extreme cases. The flutter derivatives can be seen in Figs. 3.64-71. The changes occurred at the  $A3^*$  and  $A4^*$  appear to improve the torsional motion and coupling coefficient respectively, while the  $H1^*$  and  $H4^*$  are still negative and the data shows a larger shift in the positive direction for the vertical motion. This would indicate that the critical velocity for the bridge section with traffic may be reduced, which could negatively impact the performance of the bridge. During the testing the bumper to bumper traffic on both sides and windward side only exhibited vortex shedding phenomenon at a reduced velocity 1.39, the vortex shedding is further discussed in Section 3.7.

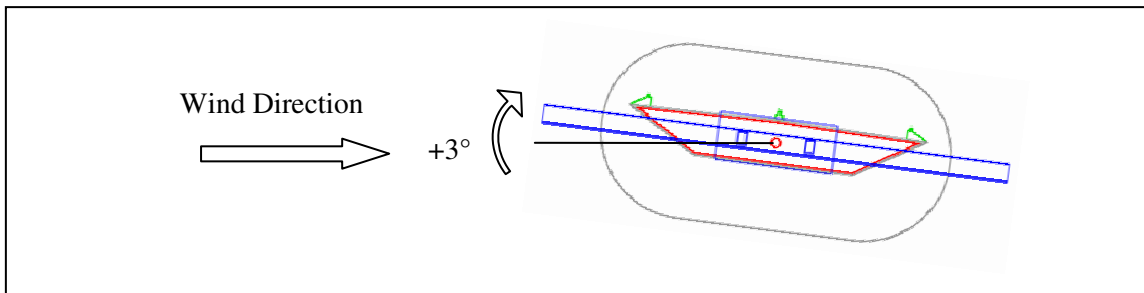


Figure 3.63: Bridge cross-section with positive 3° attack angle

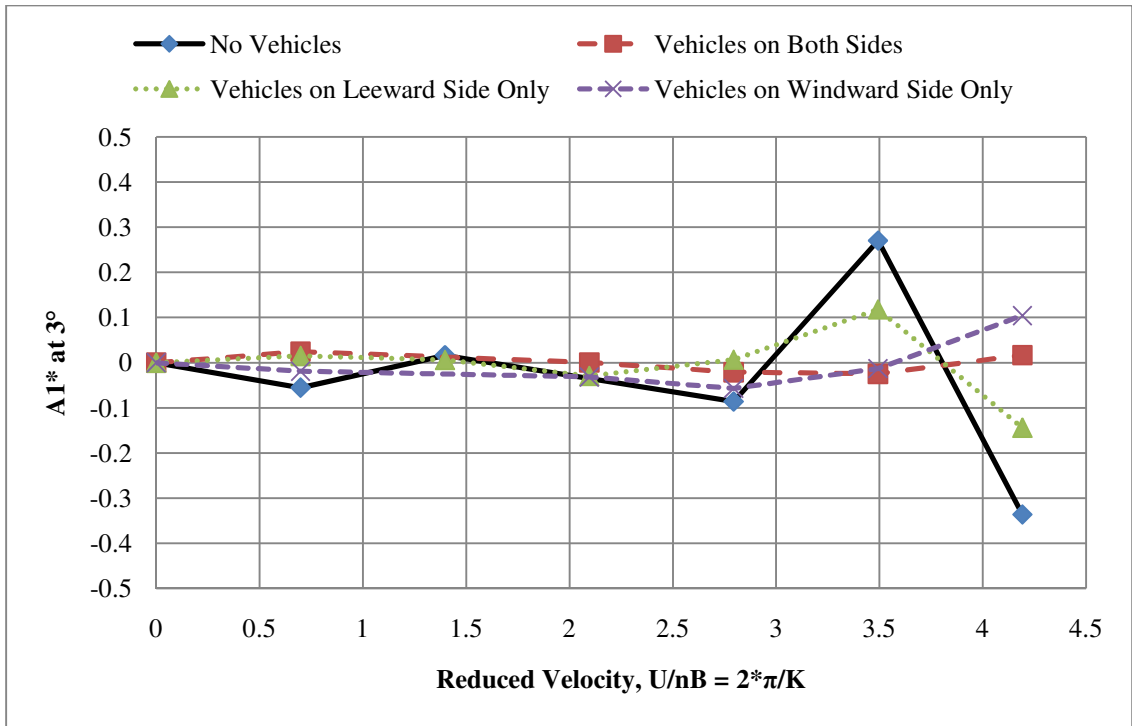


Figure 3.64: Flutter derivative  $A1^*$  for Extreme traffic scenarios with  $+3^\circ$  attack angle

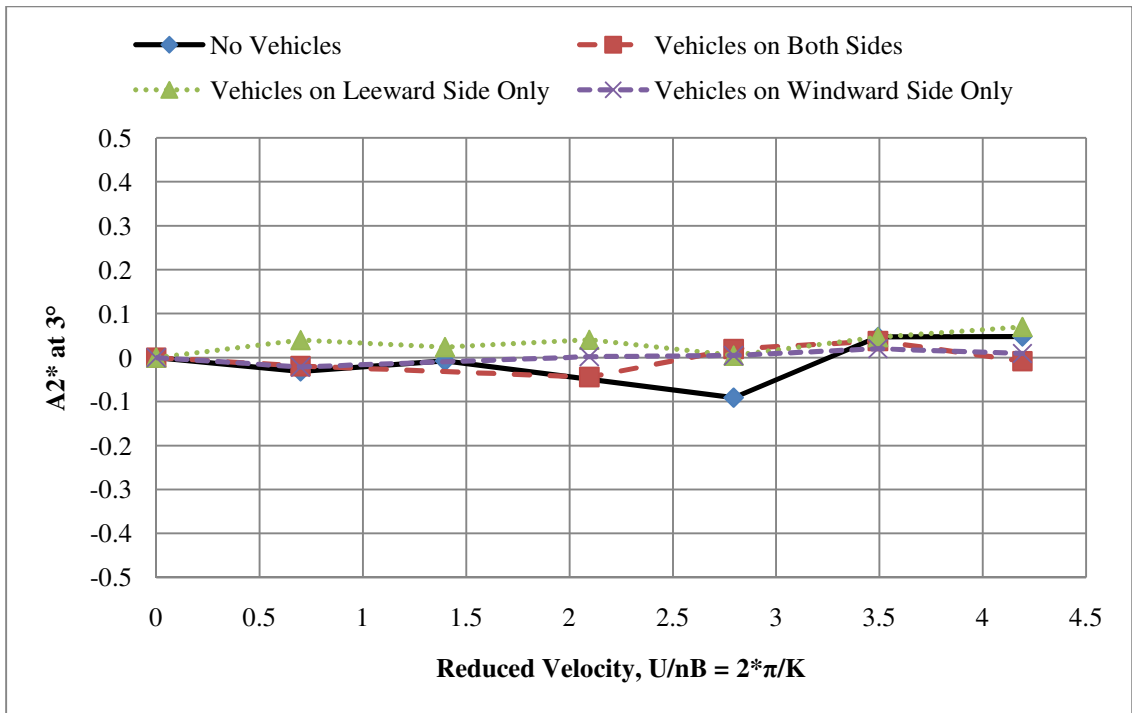


Figure 3.65: Flutter derivative  $A2^*$  for Extreme traffic scenarios with  $+3^\circ$  attack angle

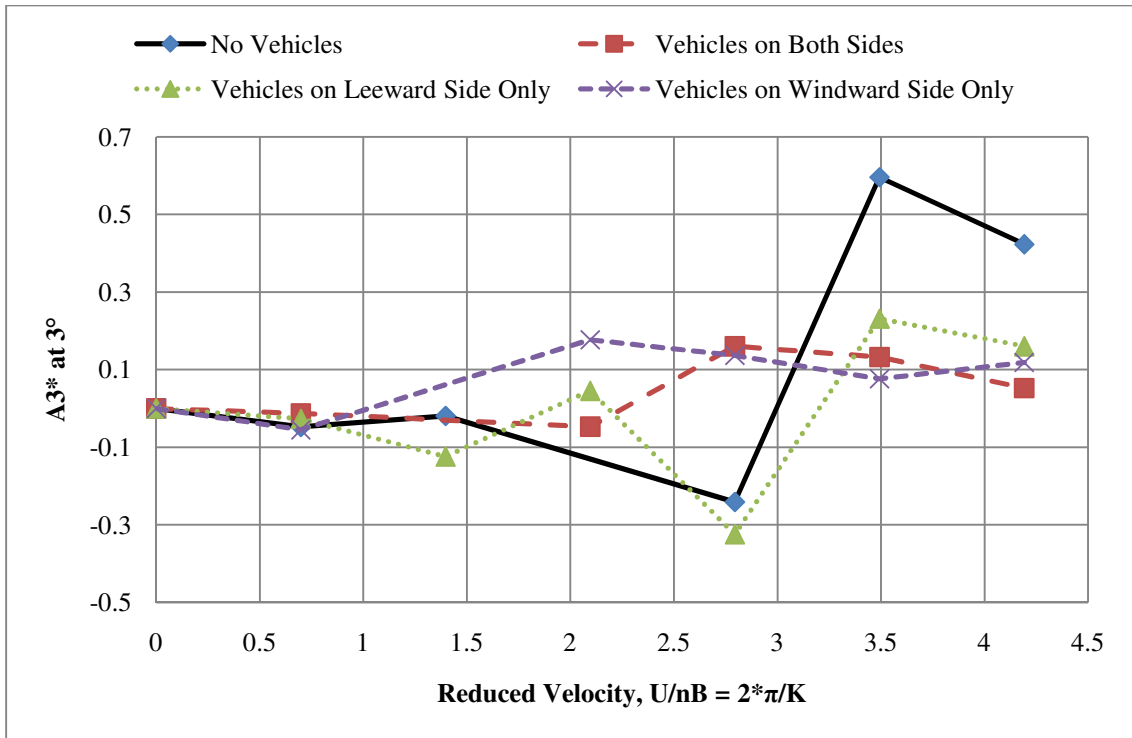


Figure 3.66: Flutter derivative  $A3^*$  for Extreme traffic scenarios with  $+3^\circ$  attack angle

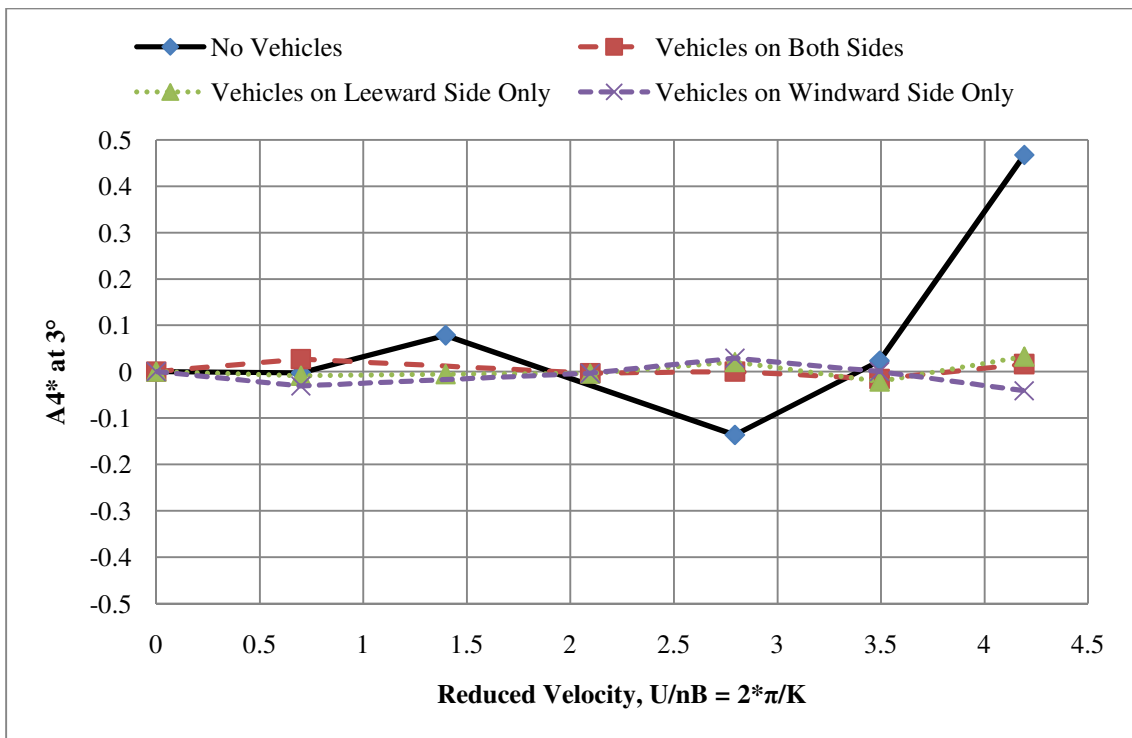


Figure 3.67: Flutter derivative  $A4^*$  for Extreme traffic scenarios with  $+3^\circ$  attack angle

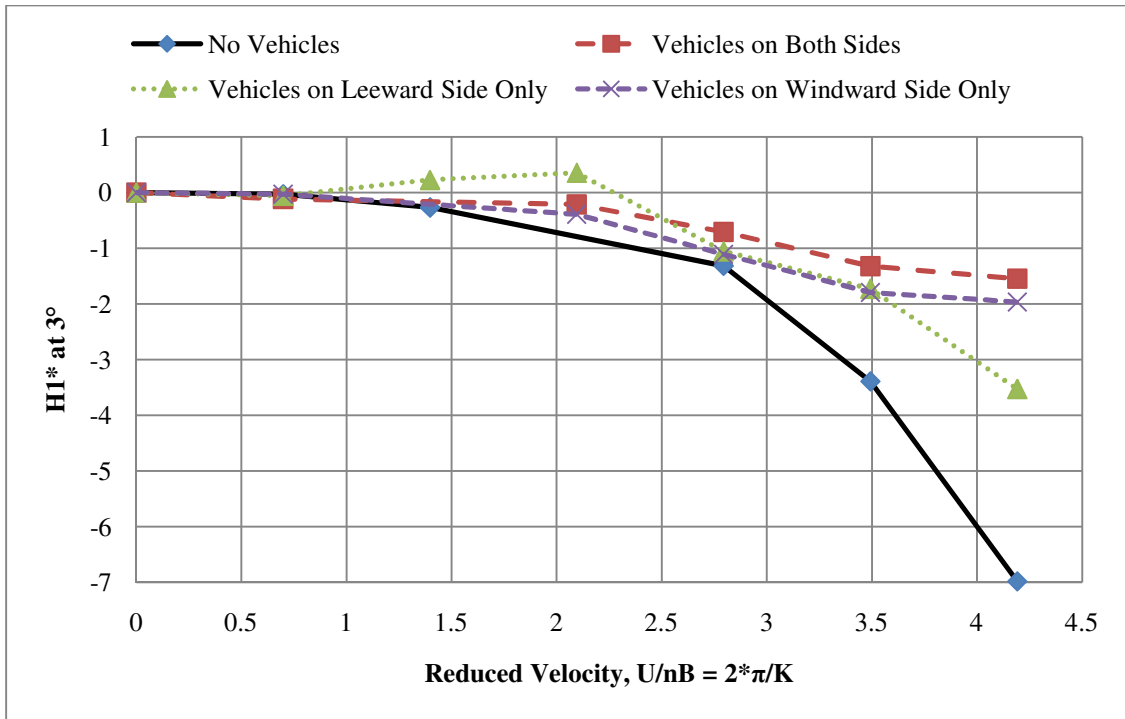


Figure 3.68: Flutter derivative  $H1^*$  for Extreme traffic scenarios with  $+3^\circ$  attack angle

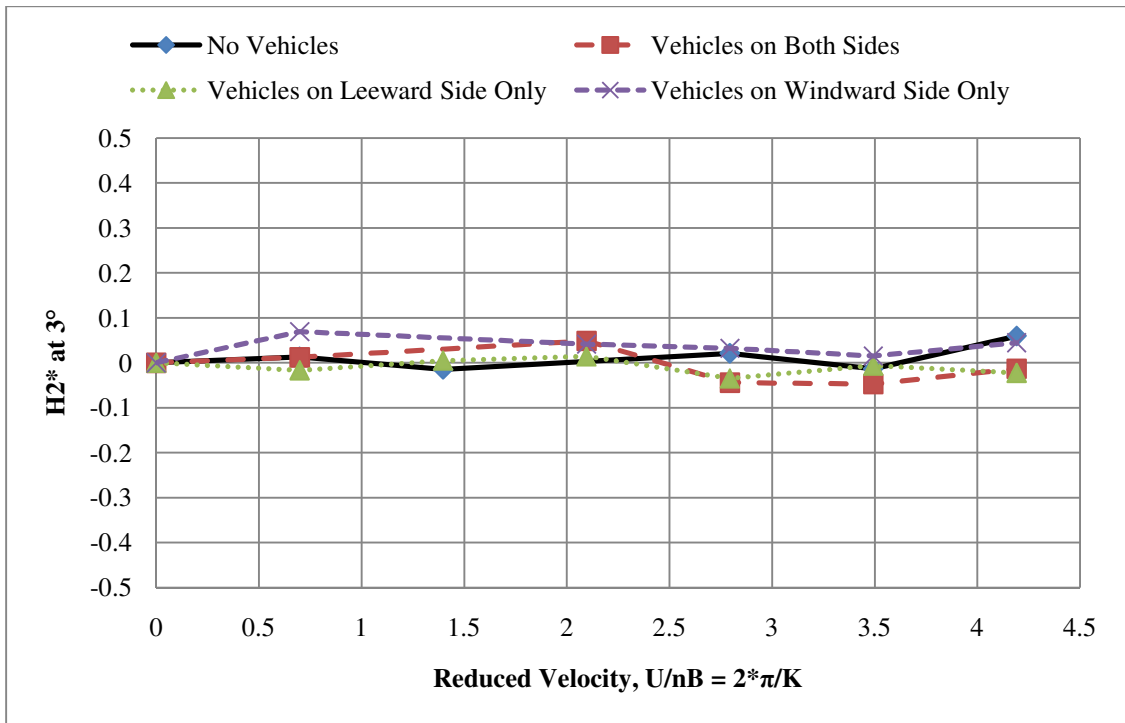


Figure 3.69: Flutter derivative  $H2^*$  for Extreme traffic scenarios with  $+3^\circ$  attack angle

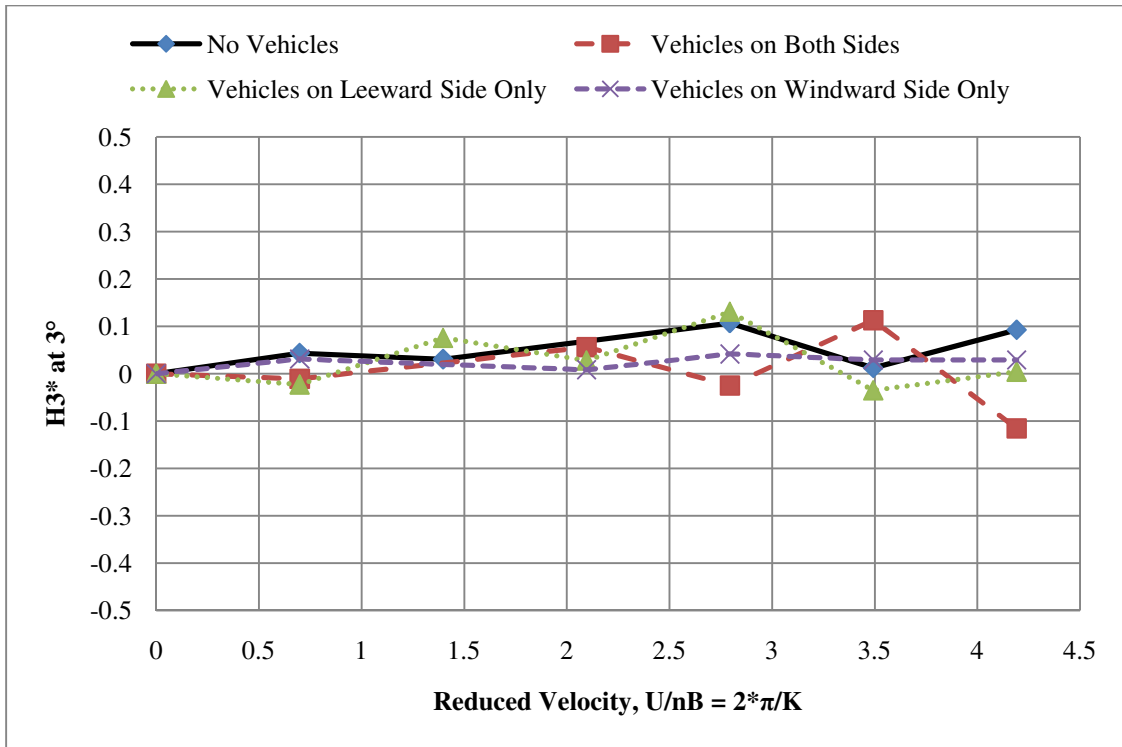


Figure 3.70: Flutter derivative  $H3^*$  for Extreme traffic scenarios with  $+3^\circ$  attack angle

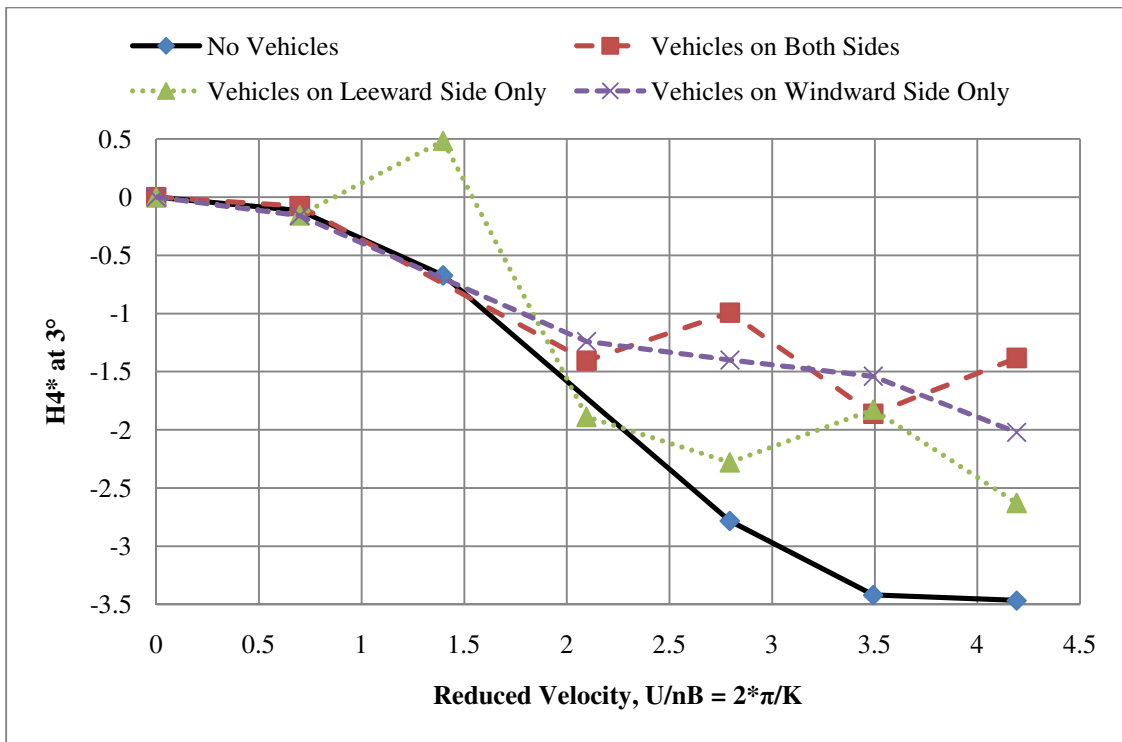


Figure 3.71: Flutter derivative  $H4^*$  for Extreme traffic scenarios with  $+3^\circ$  attack angle

### 3.5 Comparison of Attack Angles

In Figs. 3.72-79 the flutter derivatives for the empty bridge deck with variations of different attack angles are shown. The figures illustrate how the attack angle can have significant impact on the bridge performance. When examining the extreme traffic flow cases at different attack angles, one must consider the significance of the change due to the influence of traffic and attack angle. In some cases the change of attack angle has a larger impact on the flutter derivatives than the presence of traffic. It can be found that the flutter derivatives  $A1^*$ ,  $A4^*$ ,  $H1^*$  and  $H4^*$  show large variations of the flutter coefficients as compared to the results with zero attack angle.

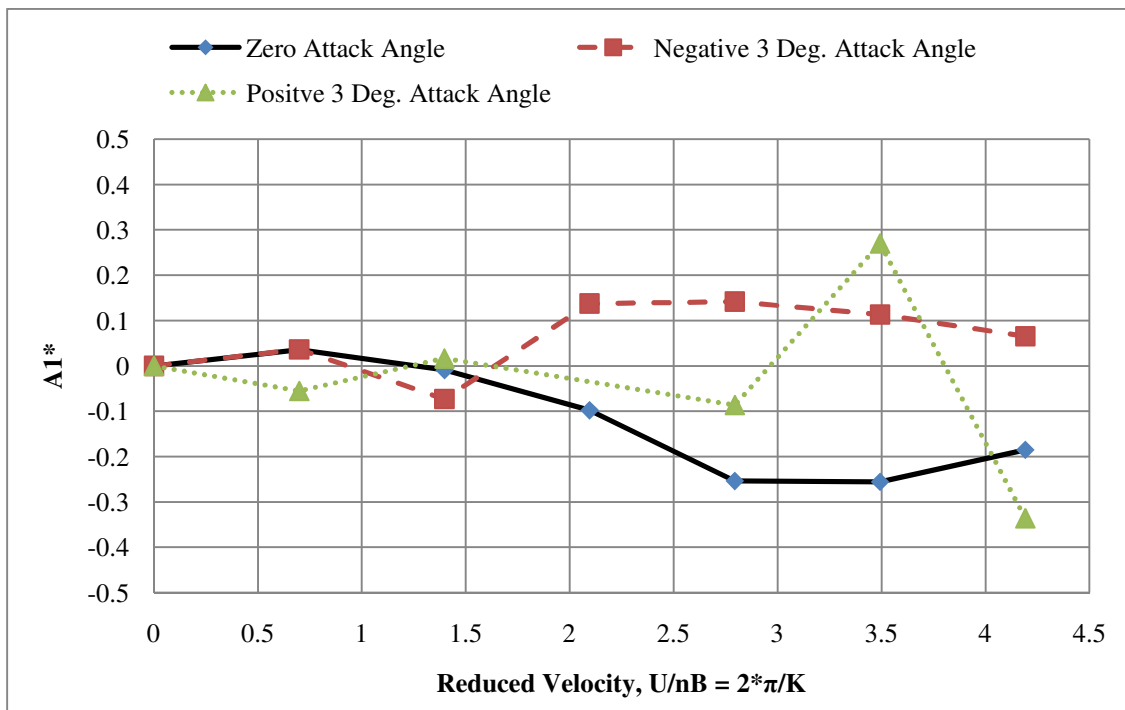


Figure 3.72: Changes in  $A1^*$  due to attack angle, no vehicles

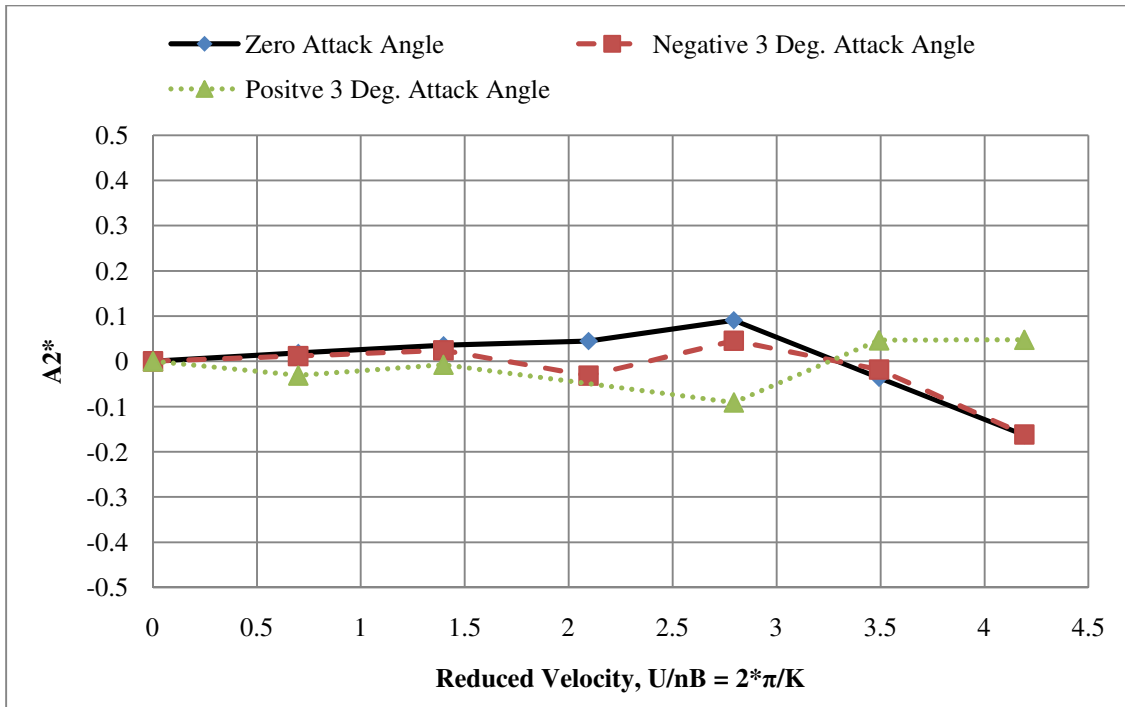


Figure 3.73: Changes in  $A2^*$  due to attack angle, no vehicles

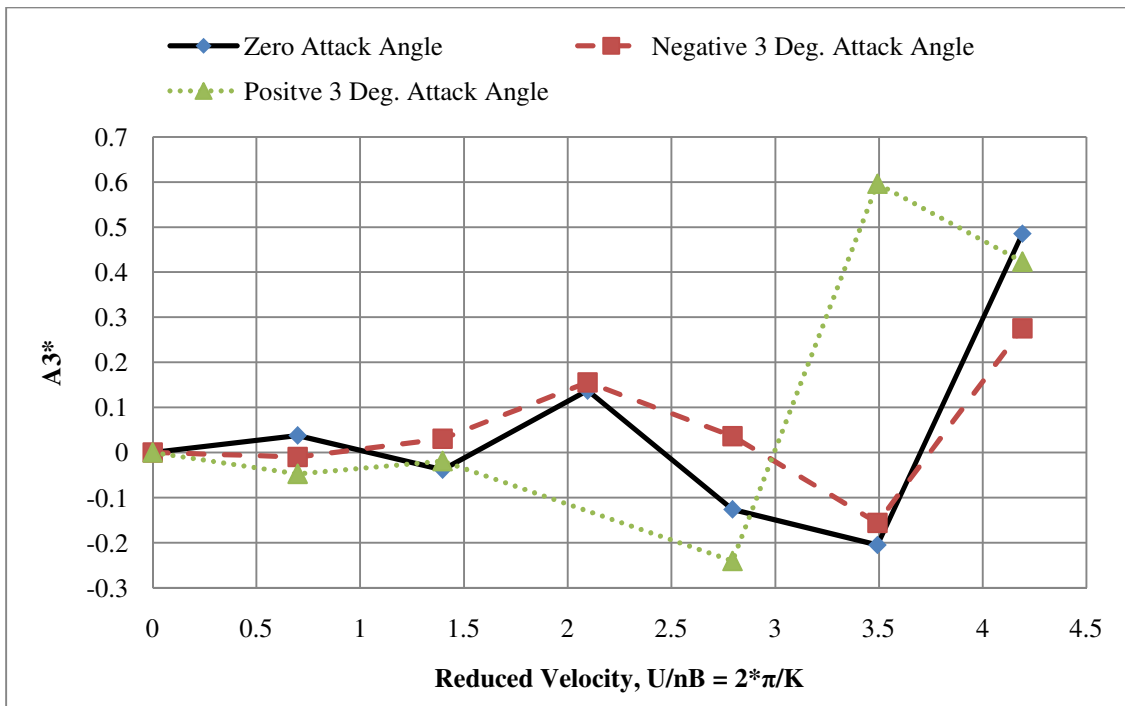


Figure 3.74: Changes in  $A3^*$  due to attack angle, no vehicles

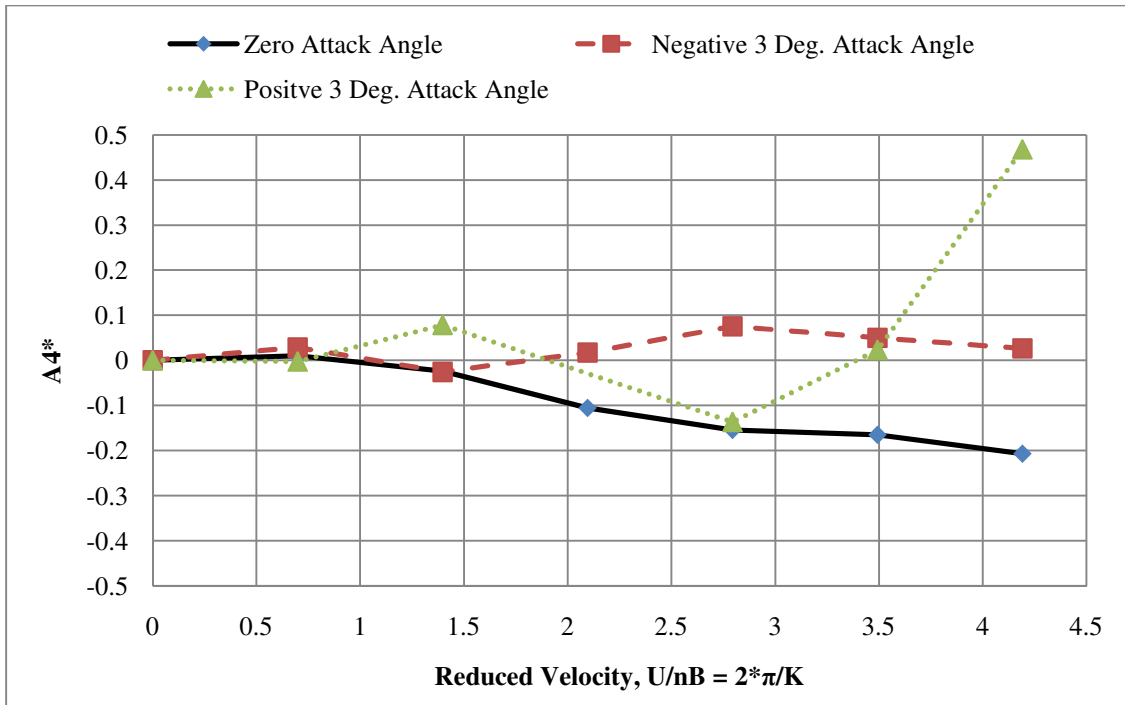


Figure 3.75: Changes in  $A4^*$  due to attack angle, no vehicles

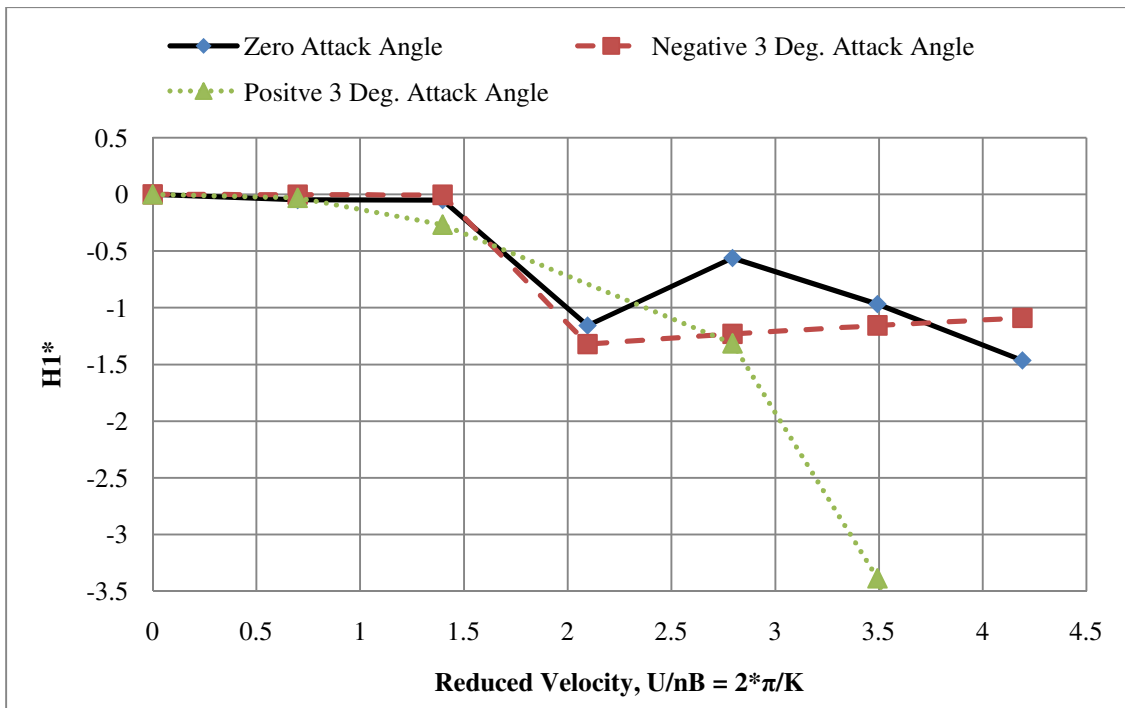


Figure 3.76: Changes in  $HI^*$  due to attack angle, no vehicles

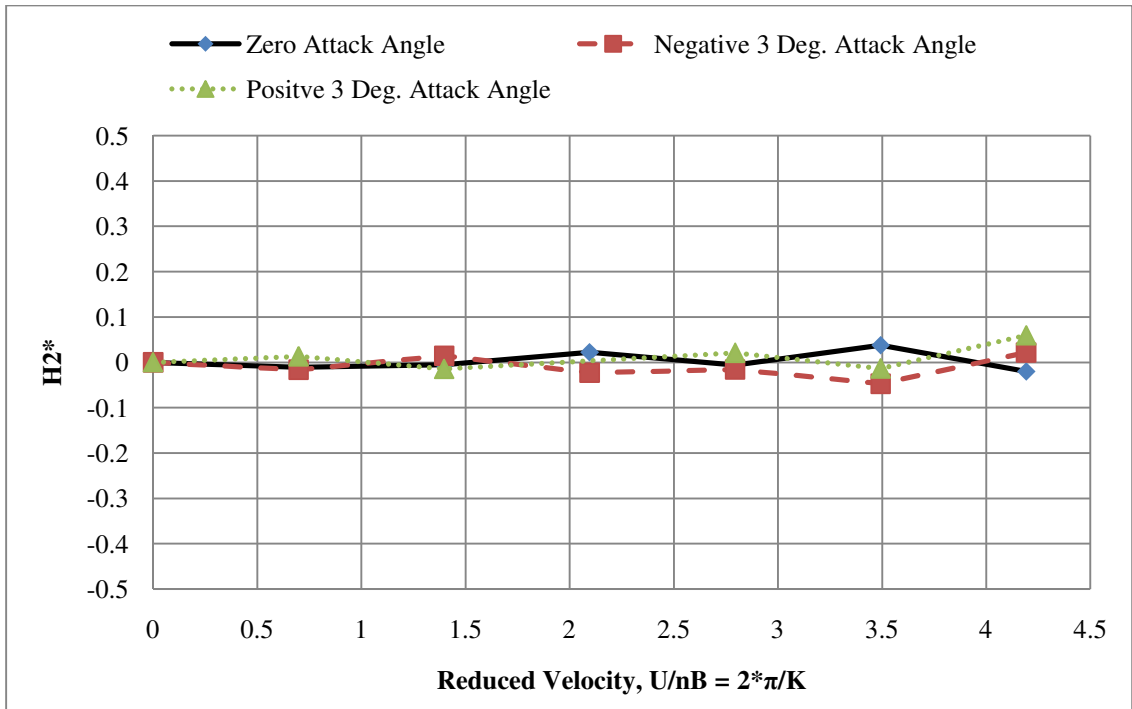


Figure 3.77: Changes in  $H2^*$  due to attack angle, no vehicles

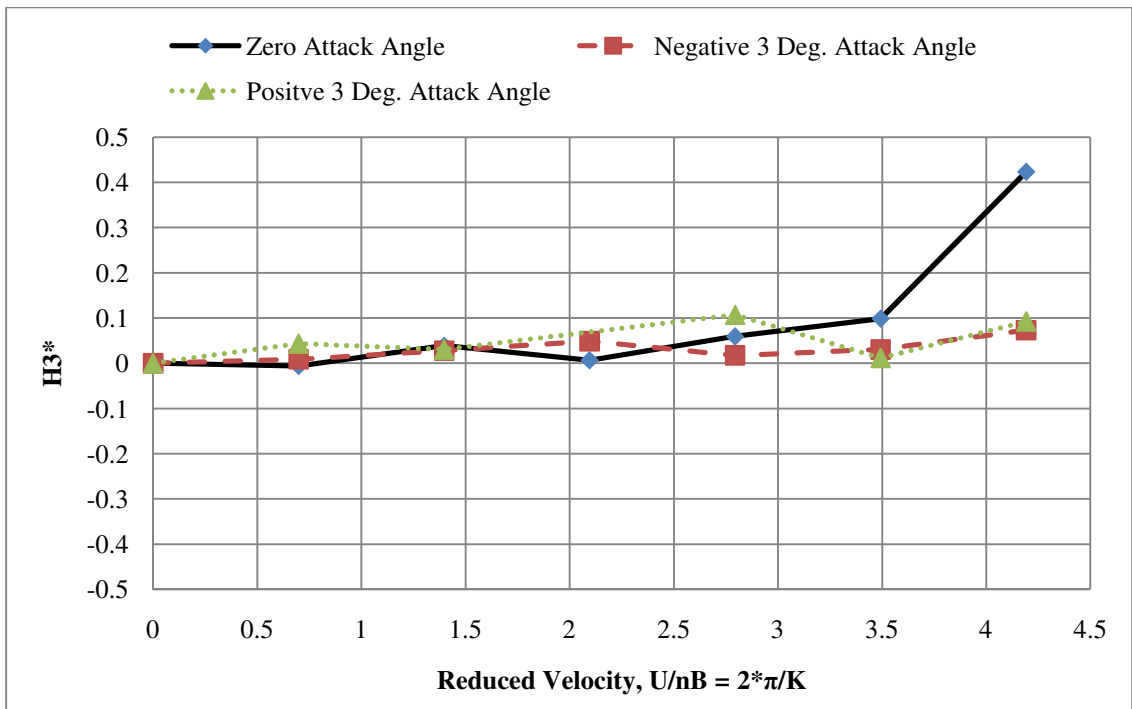


Figure 3.78: Changes in  $H3^*$  due to attack angle, no vehicles

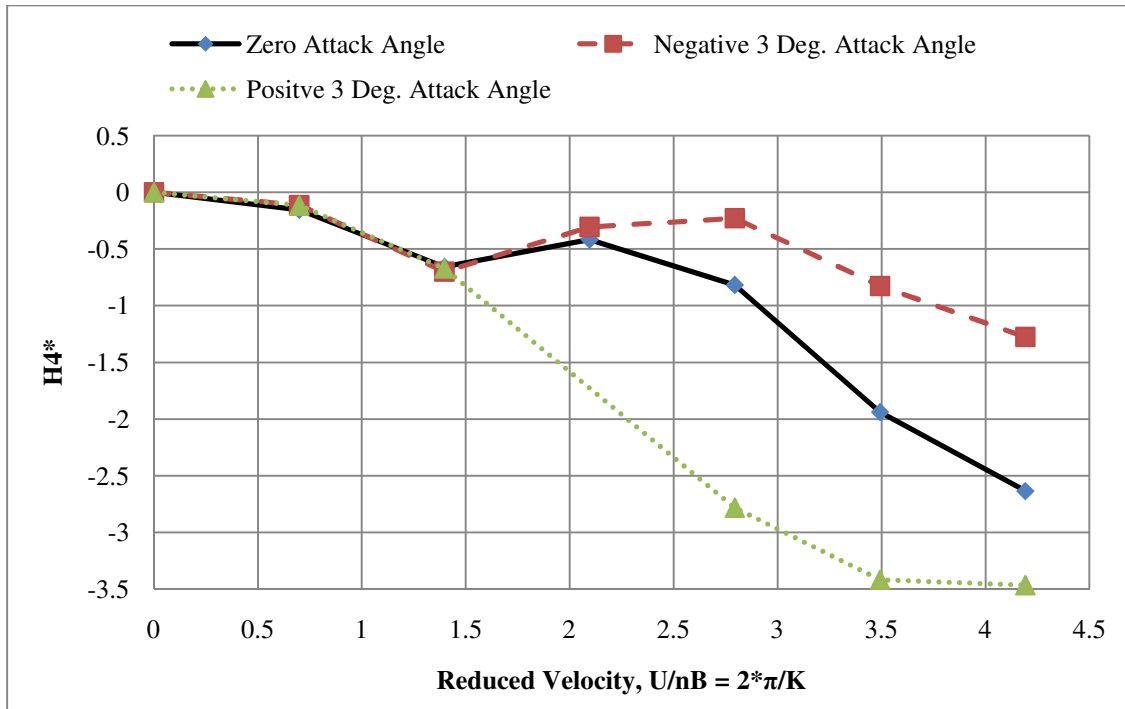


Figure 3.79: Changes in  $H4^*$  due to attack angle, no vehicles

### 3.6 Statistical Descriptions of Variation in Spatial Traffic Simulations

The spatial simulations were not affected by vortex shedding as significantly as the time dependent scenarios, so a more quantitative analysis was performed to outline the statistical parameters of the results. The mean and standard deviation were calculated for each flutter derivative in the spatial dependent traffic flow. This was performed for the 20 veh/km/ln and 32 veh/km/ln traffic flows and the results can be found in Figs. 3.80-87 and Figs 3.88-95 respectively. The mean and two standard deviations were plotted for each flutter derivative. The figures illustrate the statistical descriptions of the variations of flutter derivatives due to the spatial difference of stochastic traffic. This information can be used further to evaluate the bridge aerodynamic performance considering traffic.

### 3.6.1 Spatial Cases 2.1-3 Statistical Variation for 20 veh/km/ln Traffic Flow

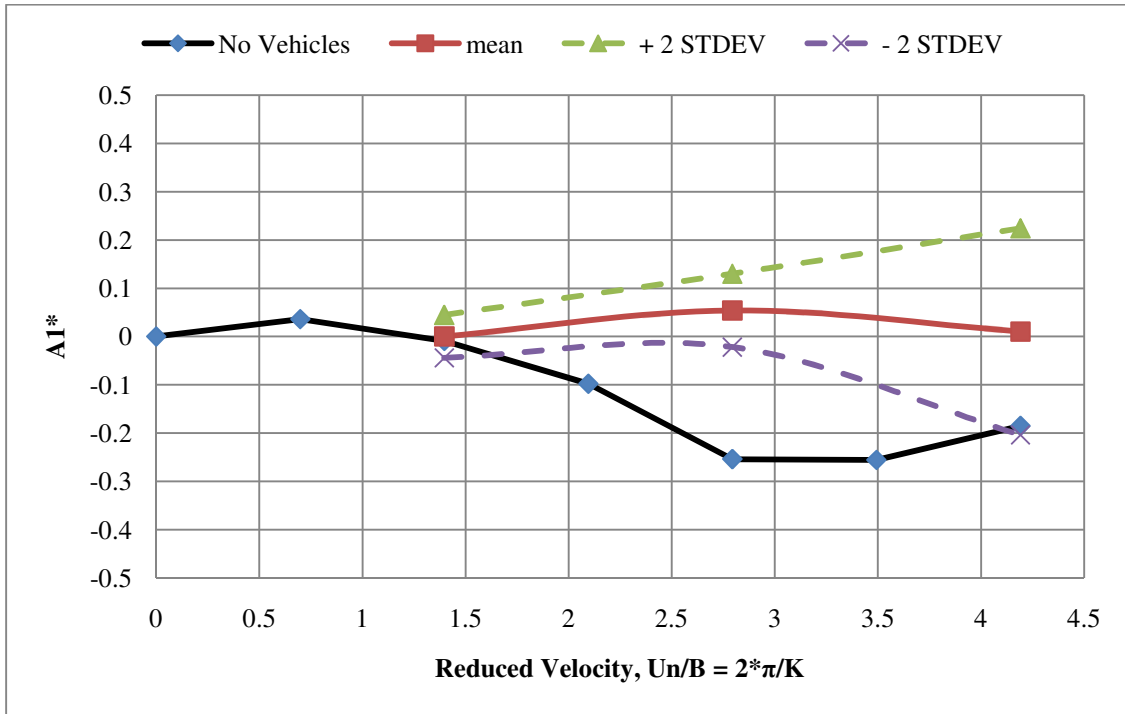


Figure 3.80: Variation of  $A1^*$  showing the mean, upper and lower 2 standard deviations

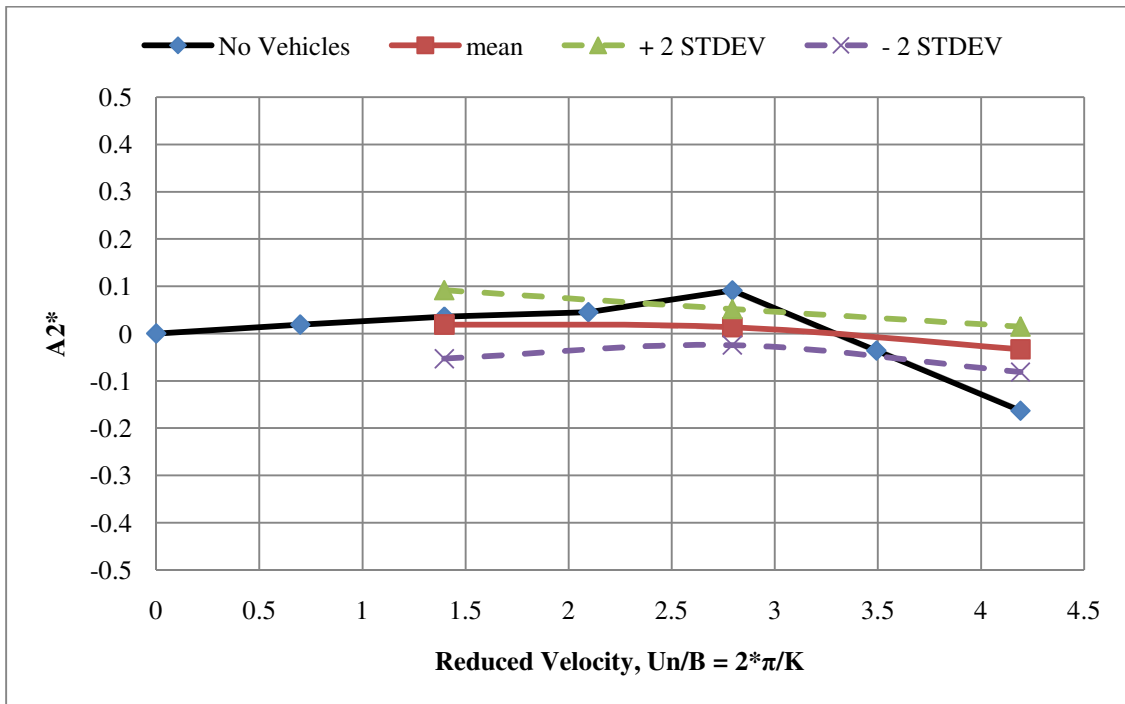


Figure 3.81: Variation of  $A2^*$  showing the mean, upper and lower 2 standard deviations

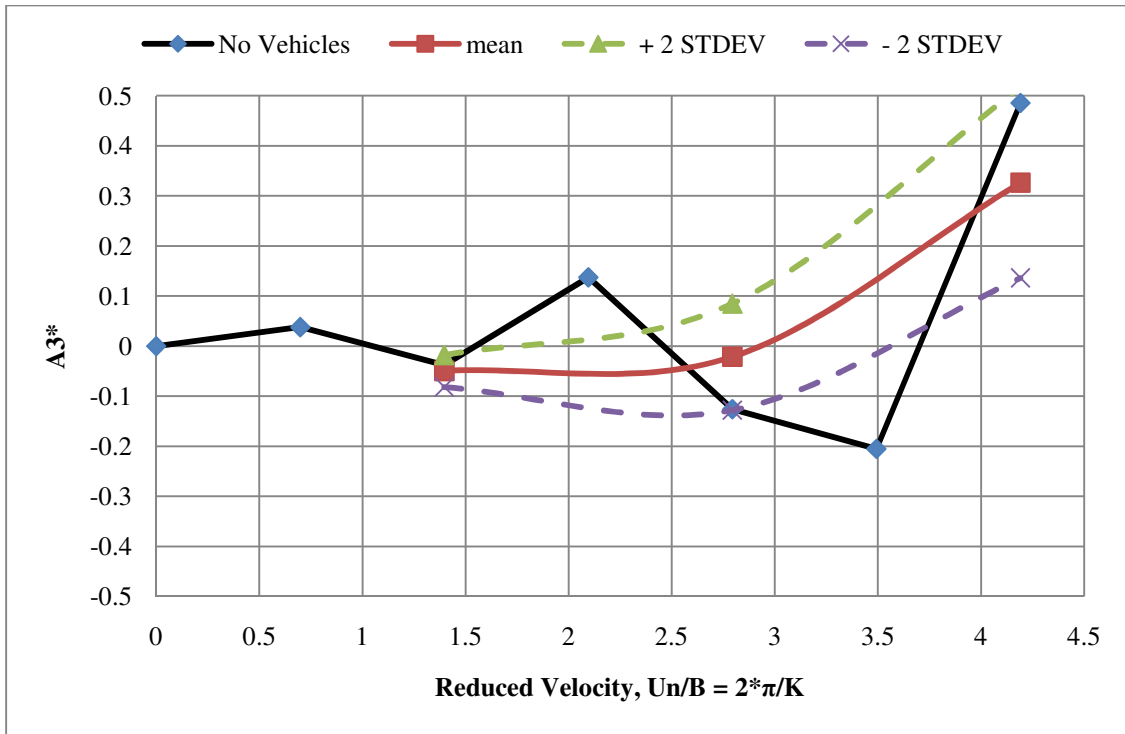


Figure 3.82: Variation of  $A3^*$  showing the mean, upper and lower 2 standard deviations

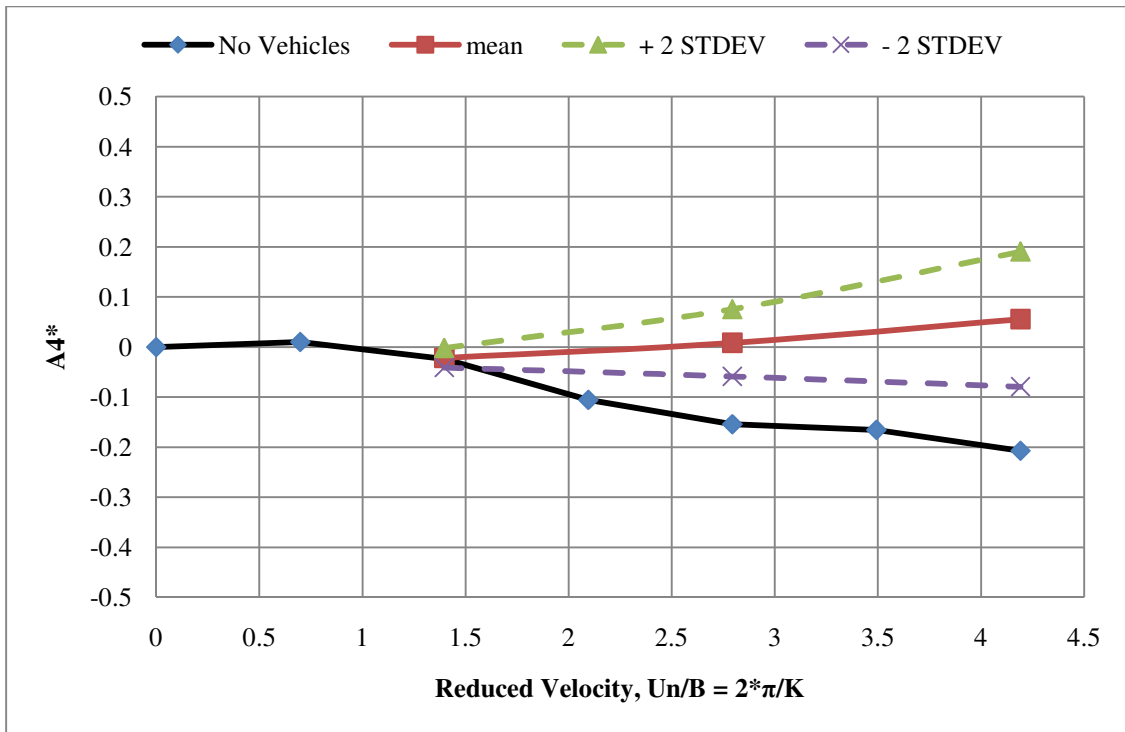


Figure 3.83: Variation of  $A4^*$  showing the mean, upper and lower 2 standard deviations

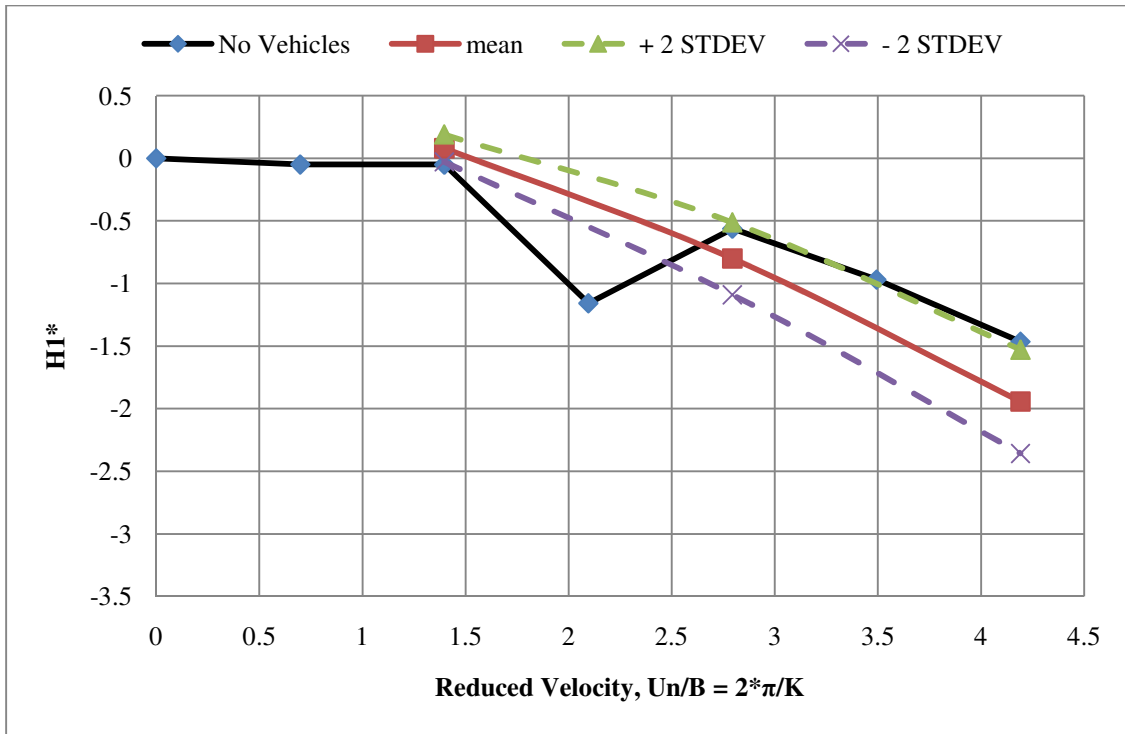


Figure 3.84: Variation of  $H1^*$  showing the mean, upper and lower 2 standard deviations

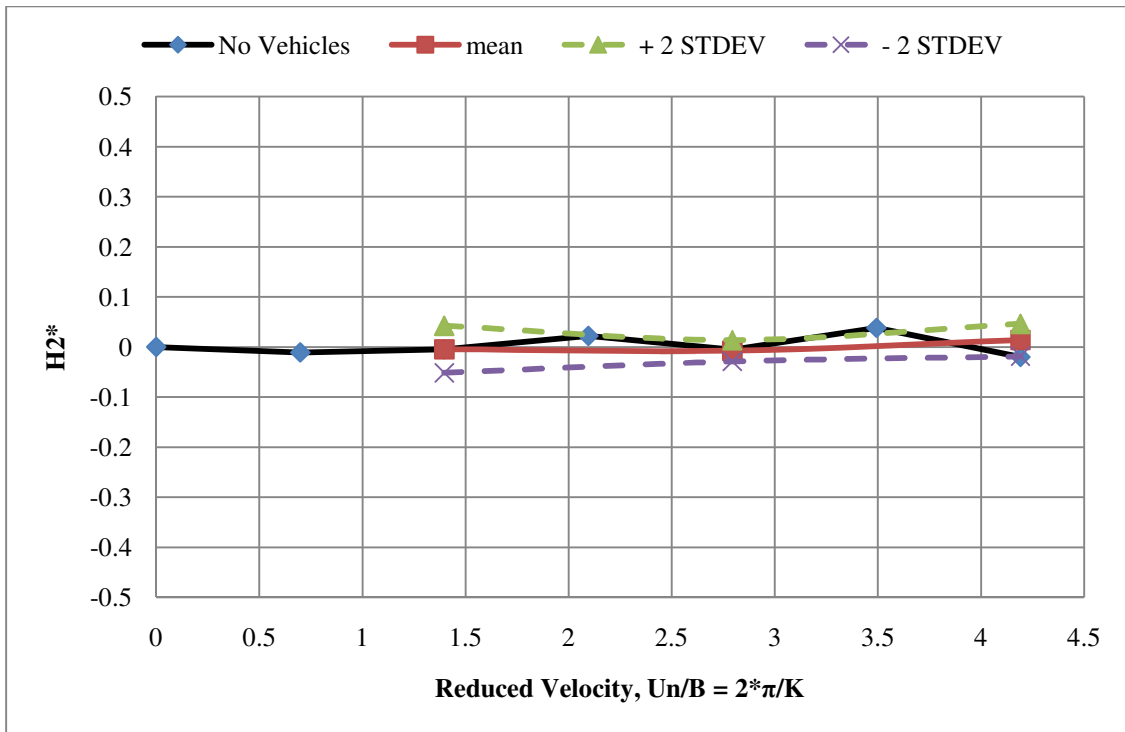


Figure 3.85: Variation of  $H2^*$  showing the mean, upper and lower 2 standard deviations

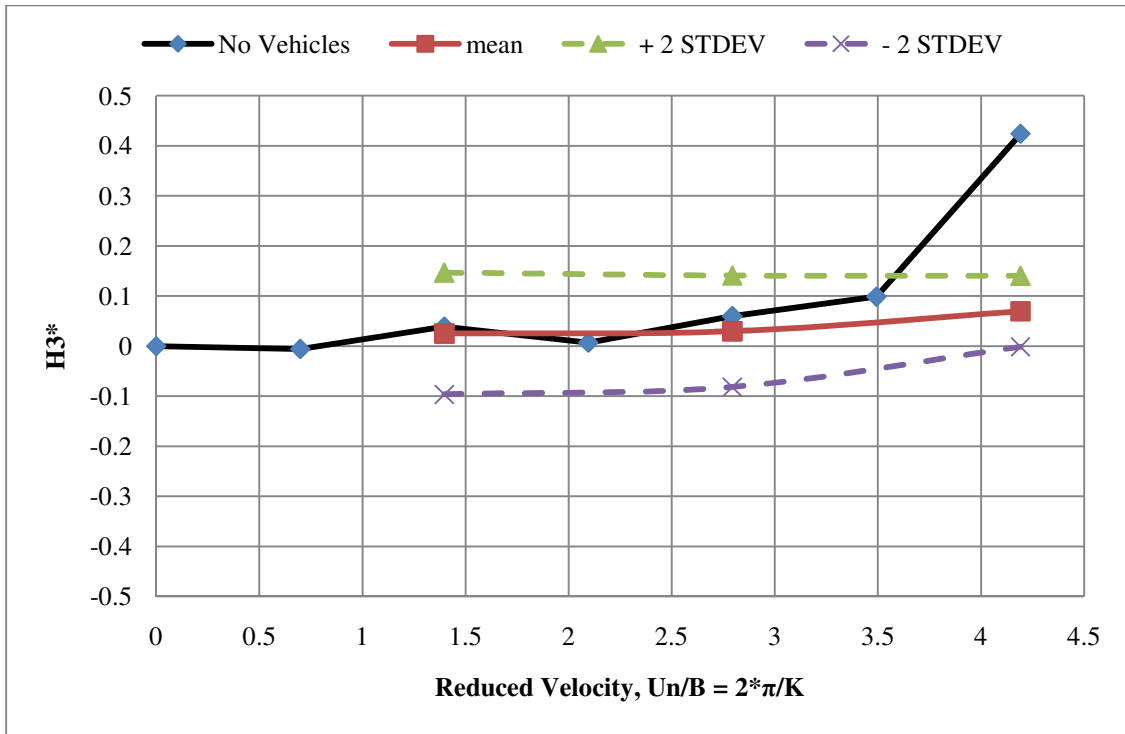


Figure 3.86: Variation of  $H3^*$  showing the mean, upper and lower 2 standard deviations

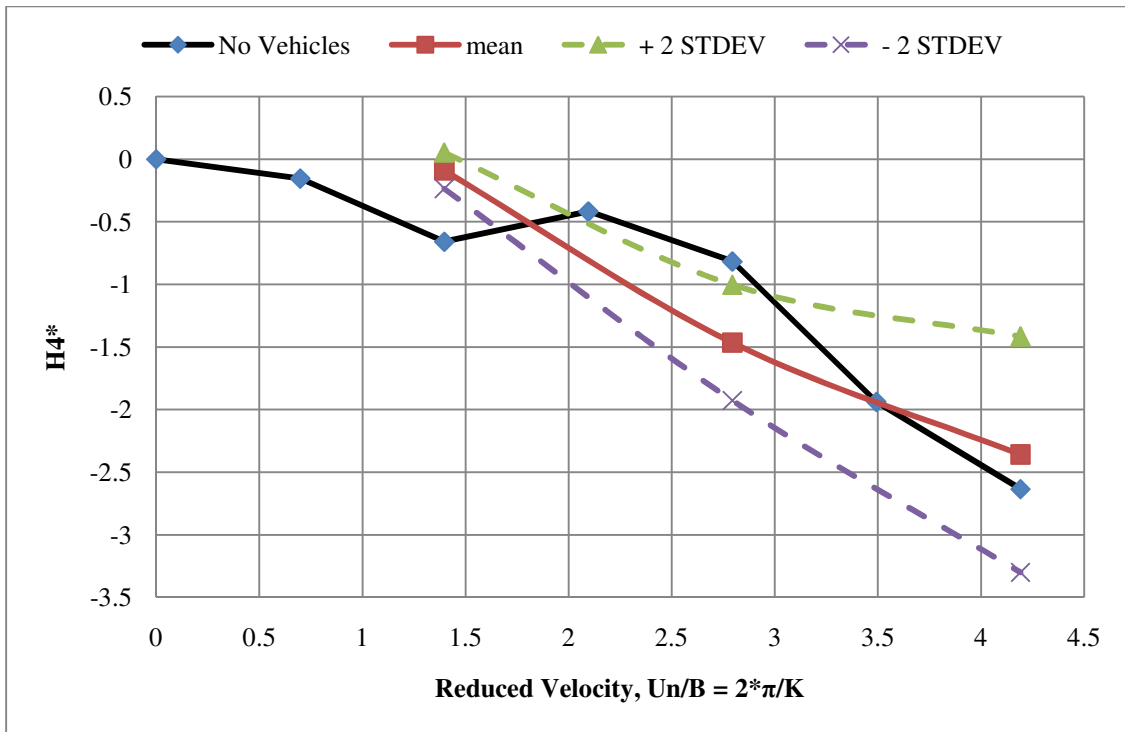


Figure 3.87: Variation of  $H4^*$  showing the mean, upper and lower 2 standard deviation

### 3.6.2 Spatial Cases 3.1-3 Statistical Variation for 32 veh/km/ln Traffic Flow

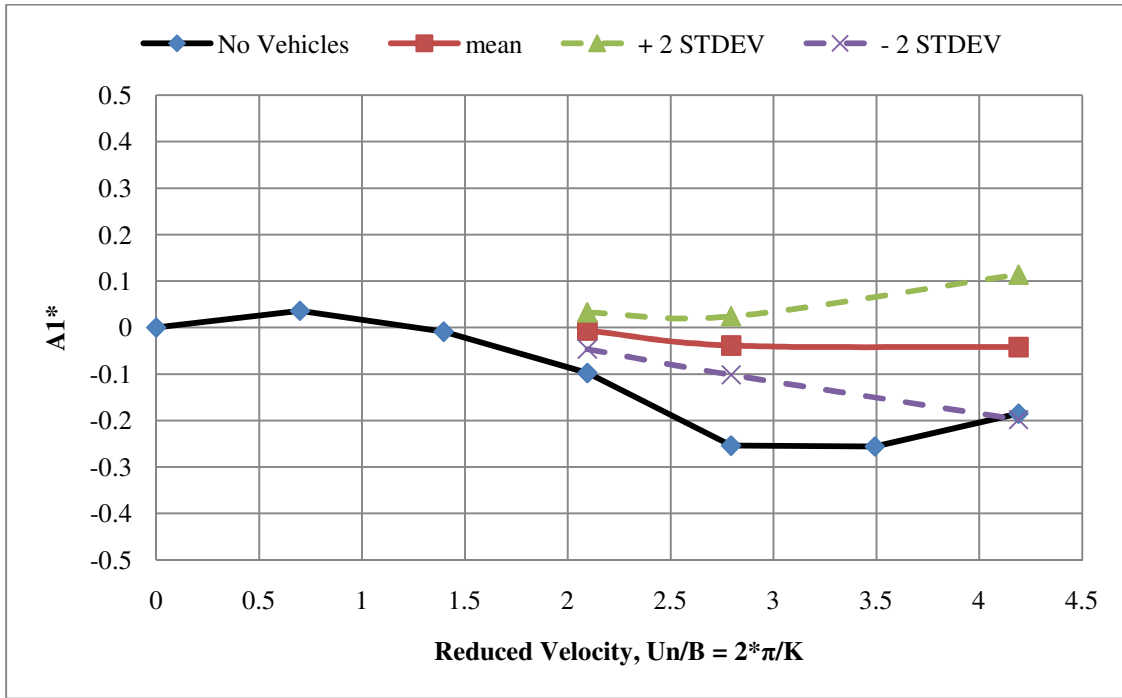


Figure 3.88: Variation of  $A1^*$  showing the mean, upper and lower 2 standard deviations

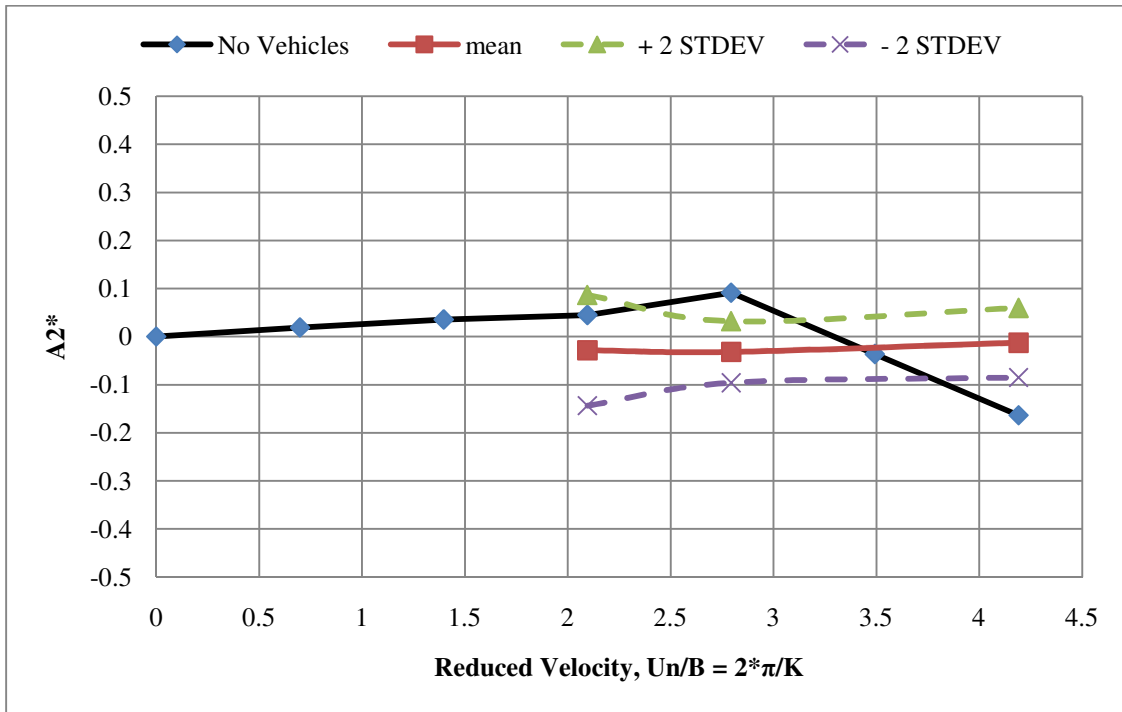


Figure 3.89: Variation of  $A2^*$  showing the mean, upper and lower 2 standard deviations

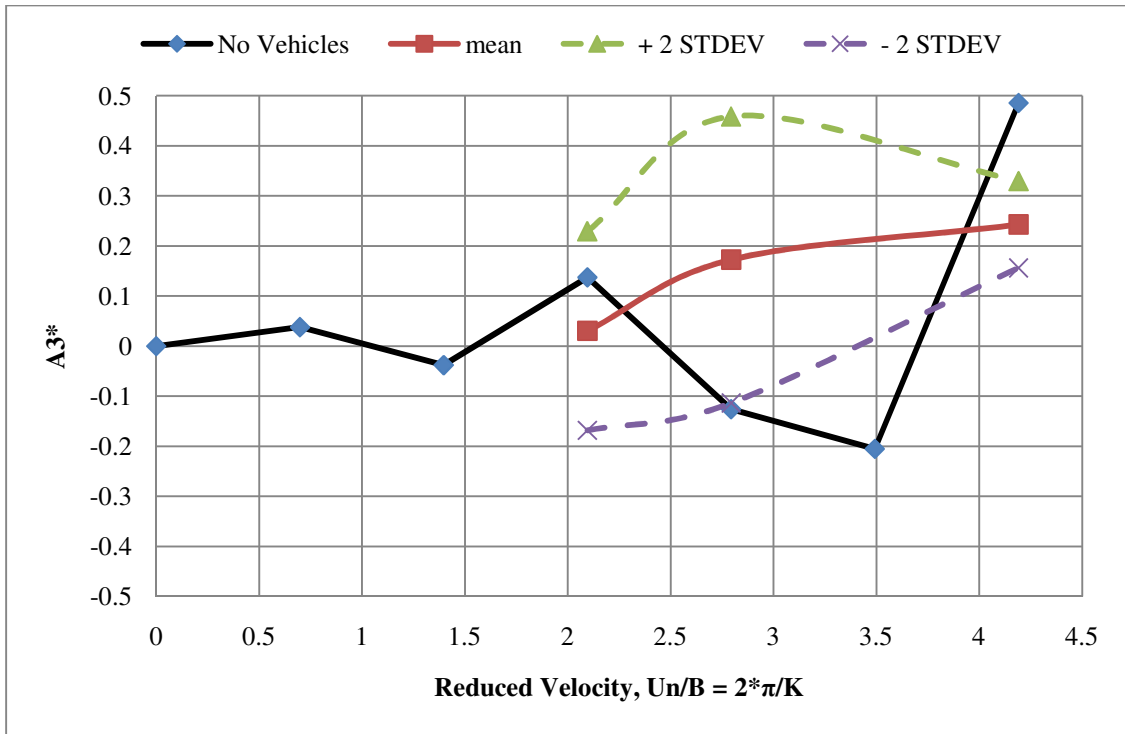


Figure 3.90: Variation of  $A3^*$  showing the mean, upper and lower 2 standard deviations

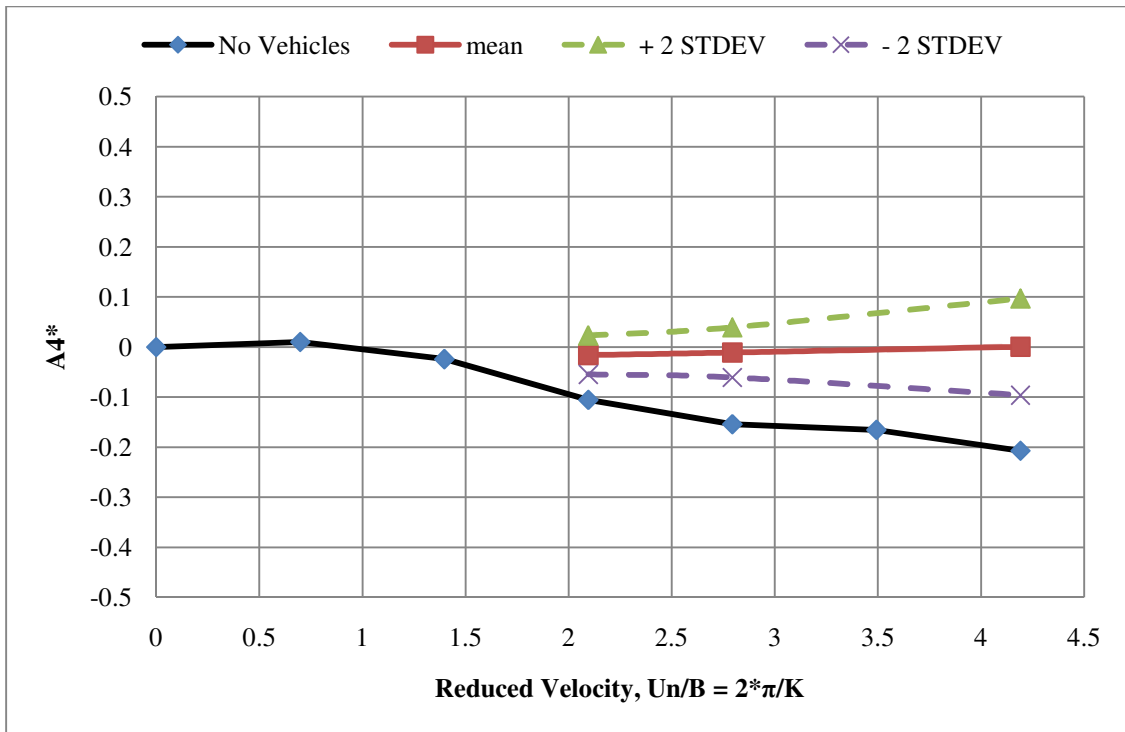


Figure 3.91: Variation of  $A4^*$  showing the mean, upper and lower 2 standard deviations

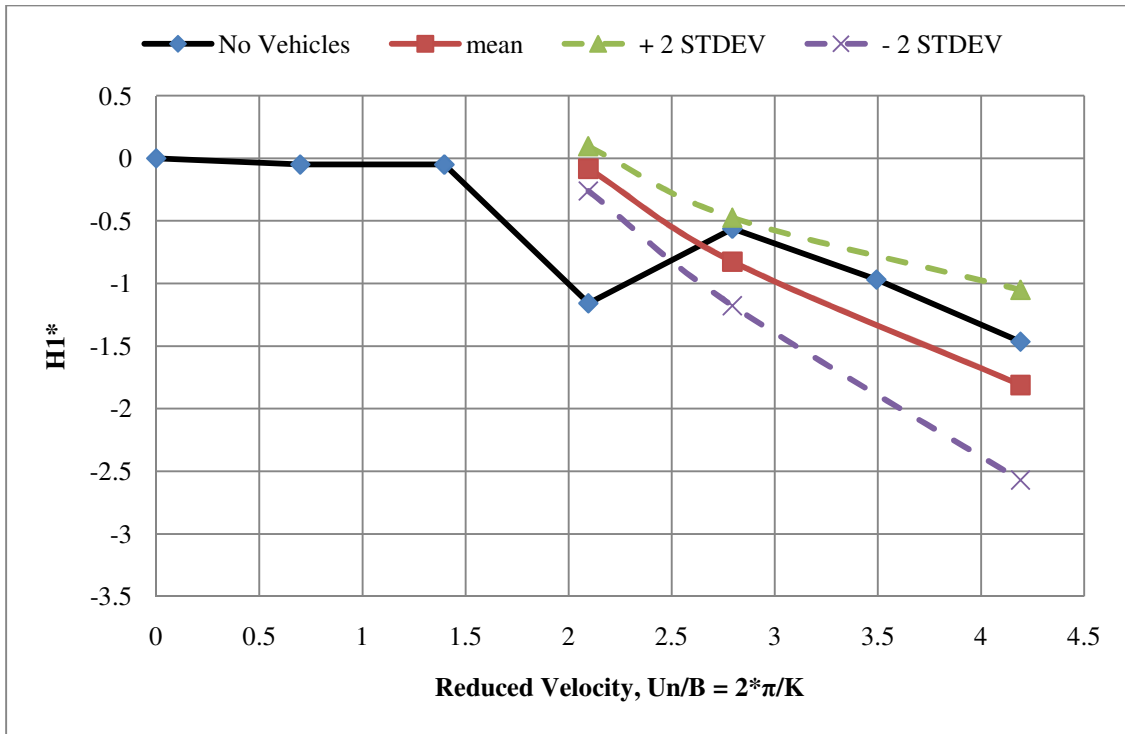


Figure 3.92: Variation of  $H1^*$  showing the mean, upper and lower 2 standard deviations

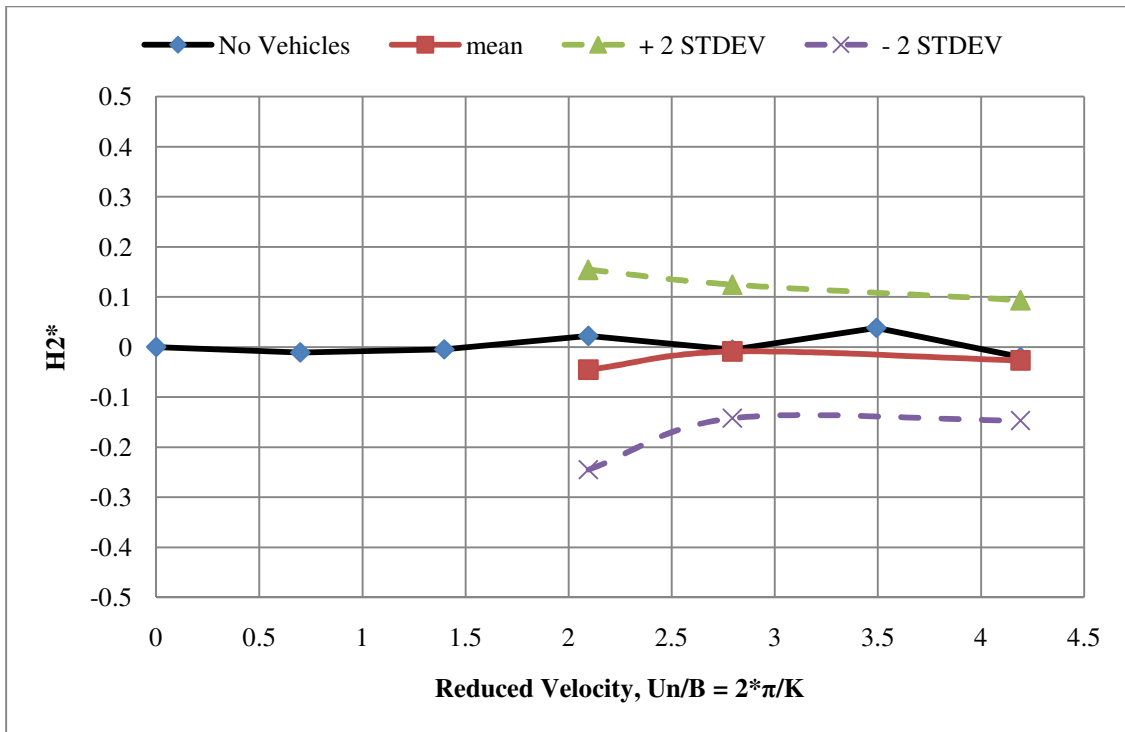


Figure 3.93: Variation of  $H2^*$  showing the mean, upper and lower 2 standard deviations

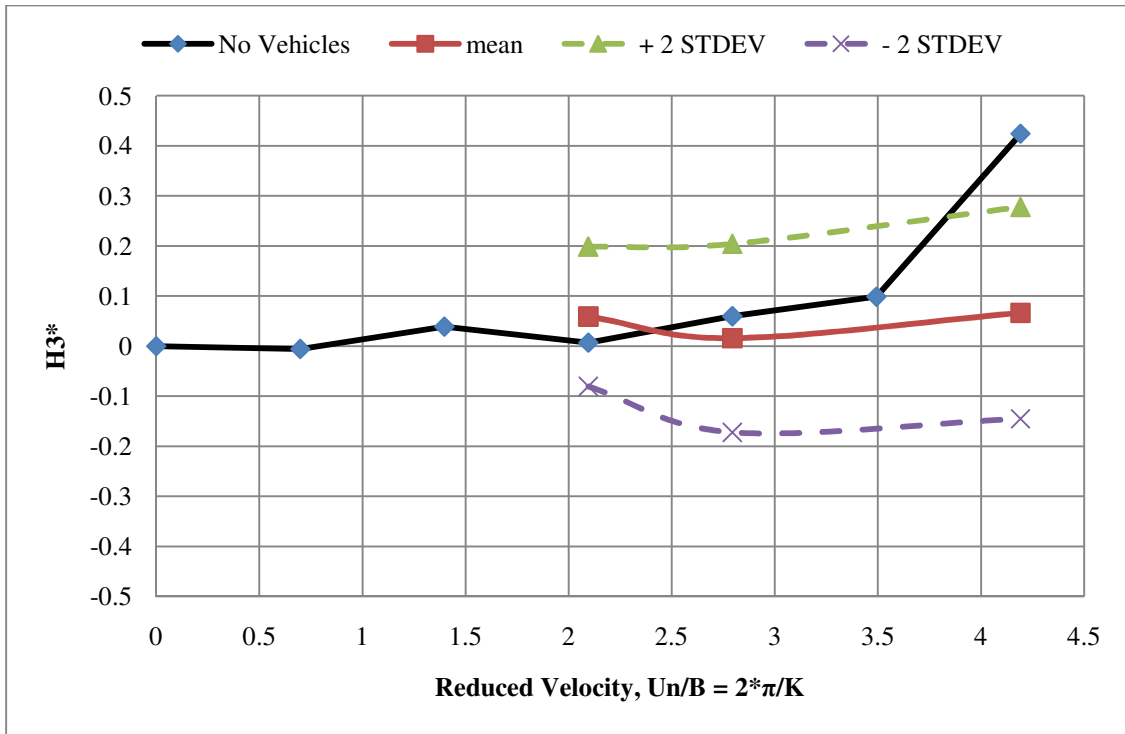


Figure 3.94: Variation of  $H3^*$  showing the mean, upper and lower 2 standard deviation

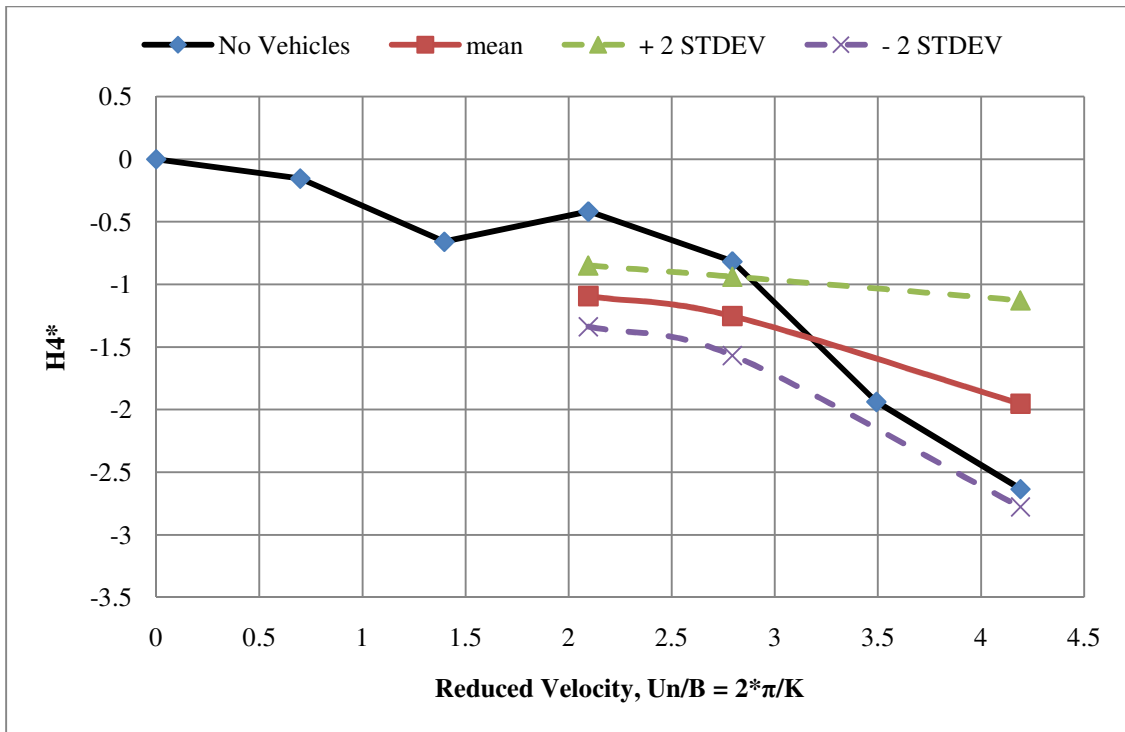


Figure 3.95: Variation of  $H4^*$  showing the mean, upper and lower 2 standard deviations

### **3.7 Vortex Shedding Phenomenon in Tests**

The spatial-dependent traffic flow first exhibited vortex shedding phenomenon with the traffic density of 32 veh/km/ln cases. The reduced velocity of 1.39 had to be eliminated from the flutter derivative testing due to the lock-in effect. Similarly in the time dependent and extreme traffic cases, the testing results at the reduced velocities of 1.39, 2.09 and 2.79 had to be removed from the final testing record due to the lock-in effect. The combination of the two changes on both the aerodynamic profile and mass of the bridge section with the presence of traffic caused the observed vortex shedding phenomenon. Throughout the wind tunnel testing the vortex shedding behavior was typically observed between the reduced velocities of 1-3. An in-depth study of the vortex behavior due to the changed geometry of the bridge section due to traffic flow should be conducted in the future.

## CHAPTER 4 SUMMARY & DISCUSSION

### 4.1 Summary and Discussions

This thesis summarized the initial experimental work to determine the aeroelastic and aerodynamic effects caused by stochastic and extreme traffic flow on slender long-span bridges. A bridge section model was constructed with a similar cross-section profile as the Luling Bridge in St. Charles Parish, Louisiana. A portable frame was developed to allow for testing in or outside of the wind tunnel. Incorporated into the portable frame design was the ability to test the bridge section in both SDOF and MDOF configurations. An electromagnetic release mechanism was developed to simultaneously release both sides of the section model and allow for different sets of initial excitations as required for testing. The release mechanism could then adapt to torsional, vertical, coupled and gallop scenarios. The bridge section model used accelerometers to obtain the time histories from the free decay tests under different wind speeds.

To simulate the stochastic traffic, various types of vehicle scaled models were manufactured. These vehicle models were put on the top of the bridge section model following the simulated traffic flow pattern. The experiments were conducted in the Wind Engineering and Fluids Laboratory at the Engineering Research Center of Colorado State University. The main issues with the Industrial Aerodynamics Wind Tunnel (IWT) were due to the current age of the drive system. The wind velocity was restricted to 50% of its maximum capacity and run times were limited to 30 minutes with 15-20 minute breaks to keep the drive motor cool. Overall the IWT provided consistent testing environment, which helped reduce systematic testing errors. The

flutter derivatives were determined from the time-histories from the accelerometers. The iterative least squares method was implemented to extract the  $A_i^*$  and  $H_i^*$  ( $i=1-4$ ) flutter derivatives. Several MATLAB codes were written to automate the ILS procedure of the flutter derivative extraction. The flutter derivatives were then compared with the SDOF and MDOF analysis to confirm the system calibration. The bridge section model was tested with the stochastic and extreme traffic flows and compared with the base lines tests of the bridge section with no vehicle.

## 4.2 Significance of Stochastic and Extreme Traffic Flow

After completing the 26 scenarios and 459 separate tests the following conclusions were made:

A1\*: The coupling coefficient generally became more positive with traffic when compared to the bridge section without traffic.

A2\*: The torsional aerodynamic damping coefficient exhibited a complex nature of variation with traffic flows that a general conclusion in terms of impact of traffic on flutter stability cannot be easily made.

A3\*: The torsional motion coefficient was very similar with and without vehicles. At the highest reduced velocity the coefficient was typically reduced with the presence of vehicles.

A4\*: The coupling coefficients typical increased with the addition of vehicles on the bridge deck for most testing scenarios. However, this was untrue during the extreme scenarios with changes in attack angle. A more comprehensive analysis is needed to quantify the coupling effects and the impacts on flutter stability and buffeting response.

H1\*: The vertical motion coefficient results did not provide a clear picture of whether the impact would be positive or negative to the bridge section model as the data points varied equally above and below the baseline test without vehicles.

H2\* & H3\*: The coupling coefficients appeared to exhibit little to no change when compared with the baseline test for the reduced velocities used. All test with or without traffic had coefficients close to zero.

H4\*: The vertical motion coefficient related with stiffness/frequency exhibited large changes in both negatively and positively on the value of the coefficient with and without traffic. In relation to the reduced values the typical trend was seen as initial positive with low velocities then becoming negative and once again becoming positive with highest velocity.

The vortex shedding lock-in phenomenon was encountered during several tests, typically between the reduced velocities of 1-3. The lock-in effect could have the potential of causing undesirable bridge vibrations that could lead to early fatigue, driver discomfort and other bridge performance issues. A more in-depth study of the vortex shedding phenomenon is needed to fully quantify the possible effects observed during wind tunnel testing of the section model with traffic.

The extreme traffic flow scenarios tested resembled the most realistic conditions as in most real cases of bumper to bumper traffic the speed is either slow to not moving. The stochastic time and spatial dependent traffic flows represent instantaneous snapshots that are statically tested. The reality is that the vehicles could be moving at a high rate of speed so the imposed traffic flow effects are constantly changing along with the addition of the dynamic vehicle forces. These scenarios also indicate another potential real life scenario in which construction or maintenance vehicles on a slender long-span bridge could unintentionally produce undesirable wind effects such as vortex shedding lock-in.

### 4.3 Recommendations and Future Experiments

In looking back at the testing process and the development of the experimental setup, there are a few areas that could be enhanced for future work.

1. In the construction of the bridge section model, thought should be given to improve the vehicle mounting and vehicle motion. This would require a much more elaborate bridge deck to simulate moving traffic flow.
2. The implementation of secondary measurement system to verify between systems. The testing apparatus only utilized accelerometers. The addition of laser displacement devices in unison with the accelerometers may provide a good check between the two data sets.
3. The development of a 3-DOF bridge suspension system that can easily restrain any degree of freedom for different testing scenarios. The system should have a mounting setup that is easily adapted to different bridge sections.
4. The release mechanism can be a critical part of obtaining good data. Care should be taken to integrate such a system that can consistently release the bridge section with a desired displacement, rotation and direction. It was difficult to design such a system for the 2-DOF system in place after the construction of the frame and model as there were fewer options available.

In the future, further studies can be built based upon the initial experimental results in the following areas:

1. A sensitivity analysis will be performed to further quantify the effects related to the changes in the flutter derivatives on long-span slender bridges.

2. The development of a fully coupled reliability-based bridge/traffic/wind analytical methodology for determining the performance of slender long-span bridges to these combined loads.

## REFERENCES

- AASHTO. (2007). *American Association of State Highway and Transportation Officials (AASHTO) LRFD Bridge Design Specifications*. Washington, D.C.
- Bartoli, G., Contri, S., Mannini, C., & Righi, M. (2009). Toward an Improvement in the Identification of Bridge Deck Flutter Derivatives. *Journal of Engineering Mechanics* , 771-785.
- Cai, C. S., Liu, X., & Peng, W. (2010). Wind Effects on Coastal Bridges and Vehicles and Mitigations., (pp. 1-27). Baton Rouge.
- Chen, S. R., & Cai, C. S. (2004). Framework of Vehicle-Bridge-Wind Dynamic Analysis. *Journal of Wind Engineering and Industrial Aerodynamics* , 579-607.
- Chen, X., & Kareem, A. (2002). Advances in Modeling of Aerodynamic Forces on Bridge Decks. *Journal of Engineering Mechanics* , 1193-1205.
- Chowdhury, A. G., & Sarkar, P. P. (2003). A New Technique for Identification of Eighteen Flutter Derivatives using a Three-Degree-of-Freedom Section Model. *Engineering Structures* , 1763-1772.
- Janesupasaeree, T., & Boonyapinyo, V. (2009). Identification of Flutter Derivatives of Bridge Decks in Wind Tunnel Test by Stochastic Subspace Identification. *American Journal of Engineering and Applied Sciences* , 304-316.
- Li, Y., Hu, P., Zhang, M., & Liao, H. (2009). Wind Tunnel Test With Moving Vehicle Model for Aerodynamic Forces of Vehicle-Bridge Systems Under Cross Wind. *The Seventh Asia-Pacific Conference on Wind Engineering (APCWE-VII)*. APCWE-VII.
- Partha P. Sarkar, N. P. (1994). Identification of Aeroelastic Parameters of Flexible Bridges. *Journal of Engineering Mechanics* , 1718-1742.

Sarkar, P. P., Chowdhury, A. G., & Gardner, T. B. (2003). A Novel Elastic Suspension System for Wind Tunnel Section Model Studies. *Journal of Wind Engineering & Industrial Aerodynamics* , 23-40.

Sarkar, P. P., Nicholas, P. J., & Scanlan, R. H. (1992). System Identification for Estimation of Flutter Derivatives. *Journal of Wind Engineering and Industrial Aerodynamics* , 1243-1254.

Scanlan, R. H. (1981). *State-of-the-Art Methods for Calculating Flutter, Vortex-Induced and Buffeting Response of Bridge Structures*. Washington, D.C.: FHWA/RD 80/050.

Scanlan, R. H. (1978). The Action of Flexible Bridges Under Wind, II: Buffeting Theory. *Journal of Sound and Vibration* , 201-211.

Scanlan, R. H., Jain, A., & Jones, N. P. (1996). Coupled Flutter and Buffeting Analysis of Long Span Bridges. *Journal of Structural Engineering* , 717-725.

Scanlan, R. (1978). The Action of Flexible Bridges Under Wind, I: Flutter Theory. *Journal of Sound and Vibration* , 187-199.

Simiu, P. D., & Scanlan, R. H. (1996). *Wind Effects on Structures 3rd Edition*. New York: John Wiley & Sons.

Thiesemann, L., Bergmann, D., & Starossek, U. (n.d.). Numerical and Experimental Evaluation of Flutter Derivatives by Means of the Forced Vibration Method. Hamburg, Germany: Technical University of Hamburg.

Thomson, W. T., & Dahleh, M. D. (1993). *Theory of Vibration with Applications*. Upper Saddle River: Prentice Hall.

Yau-Jun Ge, H.-F. X. (2008). Bluff Body Aerodynamics Application in Challenging Bridge Span Length. *Bluff Body Aerodynamics and Applications*. Milano, Italy: BBAA VI International Colloquium.

Zhou, L., & Yaojun, G. E. (2007). Sectional Model Test Study on Vortex-Excited Resonance of Vehicle-Bridge System of Shanghai Bridge over Yangtse River. *China Civil Engineering Journal*, 61-66.